

Instituto Nacional de Matemática Pura e Aplicada (IMPA)

Doctoral Thesis

**Hydrodynamic Pilot-waves:
Analytical modeling approaches to the interaction of
drops and surface waves.**

Carlos Antonio Galeano Rios

Advisor: Prof. André Nachbin

Co-Advisor: Prof. Paul Milewski

Rio de Janeiro

February, 2016



Programa de
Recursos Humanos
da ANP



anp
Agência Nacional
do Petróleo,
Gás Natural e Biocombustíveis



Instituto de
Matemática
Pura e Aplicada

Ministério da
**Ciência, Tecnologia
e Inovação**



This page was intentionally left blank.

*To my wife;
my partner in this curious journey
in seek for love and knowledge,
that we like to call life.*

This page was intentionally left blank.

*When you are studying any matter,
or considering any philosophy;
ask yourself only what are the facts
and what is the truth that the facts bear out.
Never let yourself be diverted
either by what you wish to believe
or by what you think would have
benefice in social effects if it were believed.*

Bertrand Russell

This page was intentionally left blank.

Acknowledgments

I wish to express my gratitude to many people and institutions that made it possible for me to pursue a life of studies; the baby steps of which are laid in this work.

I would like to thank my mentors; Prof. André Nachbin, Prof. Paul Milewski, and Prof. John Bush. All of whom have mastered the art of leading youth to the frontier of knowledge, without ever losing sight of the human dimension of science and mathematics.

My most profound gratitude goes to my family and their eternal protecting net, even at a distance they are always looking out for me. They have encouraged me to tackle the problems of life with reason; making my pursue of knowledge a mere consequence of that acquired taste.

My most sincere gratitudes are with my beloved wife, Fabi; who faced every unexpected challenge by my side and effectively conquered the opportunities hidden behind them.

My kindest thanks to the Professors, teaching assistants and every staff member of IMPA who so proudly work to make IMPA an oasis for the thirst of mathematics; and systematically remove spurious barriers in the way of those who seek to learn.

I specially thank the friends made along the way of these and prior studies; exchanging ideas and views about mathematics and about life with them is always constructive and fulfilling. Our shared experience of idealistic struggle is irreplaceable.

I also thank my skeptical friends from APRA, in Paraguay, the intellectual air that is shared in conversations with them has been very important to maintain a healthy outlook of life.

I could not leave out the people who introduced me to the world of meritocracy and opportunities of IMPA, among whom Prof. Christian Schaefer and Carlos Sauer particularly stand out. Prof. Roberto Markarian together with other brilliant mathematicians from the UMALCA, were also fundamental players in laying bridges to transforming opportunities in my life.

I would also like to express my gratitude to the members of the examining committee, who have kindly taken the time to review this work and improve it with their thoughtful suggestions.

This work was supported by the Agencia Nacional de Petróleo (ANP), the Conselho Nacional de Desenvolvimento Científico e Tecnológico (CNPq), the MIT International Science and Technology Initiative (MISTI) through the MIT-Brazil program and the University of Bath (UK) through the Global Partner Research Scholarship Scheme.

Abstract

A millimetric drop can be made to bounce indefinitely on the surface of a vertically oscillating bath of the same fluid. This inhibition of coalescence is achieved by the sustenance of an air layer during the drop's impact with the free surface. The bouncing drop can also become unstable to lateral perturbations and thus execute a horizontal trajectory. The *bouncer* or *walker* thus produced is a macroscopic particle-wave association that mimics phenomena previously thought to be exclusive to the quantum realm. We develop models of particle and fluid mechanics that capture several of the behaviors of bouncing droplets; including different modes of bouncing and walking, wave field features and walker-walker interactions. We have focused on a reduced modeling attempt that starts from first principles; and which, as will be shown, is capable of capturing the spontaneous emergence of these behaviors, in very good agreement with laboratory experiments.

Keywords: Faraday Waves, Capillary-Gravity Waves, Drops, Hydrodynamics.

This page was intentionally left blank.

Contents

Abstract	ix
Introduction	1
1 The Linear PDEs Fluid Model	5
1.1 Linearized Navier-Stokes and the Helmholtz decomposition	5
1.1.1 PDEs and Boundary Conditions	5
1.1.2 A Helmholtz Decomposition	7
1.1.3 Reducing the Problem	8
1.2 Wave-like Solutions	10
1.3 Infinite Depth	12
2 Slowly Decaying Waves	15
2.1 An Asymptotic Limit	15
2.2 The Dispersion Relation	16
2.2.1 A Consistency Check	17
2.3 Faraday Waves	18
2.4 The Faraday Threshold	19
2.4.1 Some Examples and a Correction Factor	22
3 Generation and Propagation of a Hydrodynamic Pilot-Wave	25
3.1 Droplet Dynamics	25
3.1.1 The Hypothetical Surface	26
3.1.2 The Equations of Droplet Motion	26
3.2 Forcing the Waves	27
3.3 Bouncers and Walkers	28
3.3.1 The Transient of a Walker	32

3.3.2	Accuracy of Predicted Vertical Motion	34
3.3.3	Wave Fields	36
3.4	Multiple Droplets	39
3.4.1	Scattering and Orbiting	40
3.4.2	The Promenade Mode	42
3.5	Possible Improvements	43
4	A Kinematic Matching Condition	45
4.1	The Modeling Assumptions	45
4.2	An Implicit Iterative Method in Physical Space	47
4.3	A Problem of Singular Integrals	48
4.4	Simulating a Bouncer	48
4.4.1	Results	52
4.4.2	Possible Improvements	60
5	An Improved Viscous Water Wave Model	61
5.1	Solving the System	61
5.2	Faraday Forcing	66
5.2.1	Some Examples	68
Appendices		73
A	Linearization	75
B	The Dirichlet to Neumann Operator	79
B.1	The Laplace Problem	79
C	Comments on the Solution to the Heat Equation	81
D	The N Transform for the Laplace Problem in the Half-space	83
D.1	How to compute the N map	83
D.1.1	The Neumann to Dirichlet map	83
D.1.2	Inverting the Neumann to Dirichlet map	85
D.1.3	Convergence of the singular integral of the N map in the principal value sense	89

Introduction

When a fluid bath is subject solely to the action of constant gravity, its undisturbed free surface will match a horizontal plane. If said bath is then subject to sinusoidal vertical motion, with angular frequency ω_0 and increasing amplitude A , its free surface initially remains planar; but as the amplitude $\gamma = A\omega_0^2$ of the oscillatory acceleration reaches a certain value, it becomes unstable to a field of standing waves. This critical acceleration amplitude is known as the Faraday threshold (γ_F), and the waves observed are known as Faraday waves. These waves have half the frequency of the imposed vibration, and a wavelength (λ_F) prescribed by the standard capillary-gravity wave dispersion relation. An inviscid theory that successfully describes the field of standing waves is presented in [1], and a linear stability theory is presented in [36].

In a certain parameter regime, coalescence of an impacting millimetric drop can be prevented when the bath oscillates vertically. The minimum value of γ that permanently inhibits coalescence is known as the bouncing threshold [40]. This is made possible by the sustenance of an air layer that prevents van der Waals forces to trigger coalescence. The oscillatory motion allows for the replenishing of this layer and thus causes the drop to bounce indefinitely [11, 51, 52]. In particular, the amplitude of oscillatory acceleration must be below the Faraday threshold but above a certain minimum value. A *bouncer*, a coherent association of a drop and the waves generated by its previous impacts, is thus created.

Just above the bouncing threshold, the drop bounces in synchrony with the forcing; however, as the forcing amplitude is increased, the bouncing undergoes a period doubling transition, thus matching the frequency of the subharmonic Faraday wave field. Resonance is thus achieved between the bouncing droplet and its accompanying wave field, energy is most readily transferred between the two, and one can view the bath as being a damped oscillator forced at resonance [38].

Several regimes of bouncing and the corresponding transitions have been experimentally observed and theoretically described [9, 23, 40, 49, 53]. Perhaps most importantly, a walking regime has been discovered [41, 48, 53]. It occurs when the axial symmetry of the droplet-wave pair is broken as the drop happens to land not exactly on the peak of the wave but rather on its slanted side. This impact on an inclined surface provides a net horizontal component of the forces

that appear during contact and thus propels the droplet in a horizontal direction [10, 12, 41, 48, 53]. The drop then becomes a moving source of surface waves.

Walkers can interact with boundaries and with each other. These interactions occur by means of their wave fields, which store information of the environment and the history of previous bounces. In turn, the form of the surface during impact influences the motion of the drops. Surprising behaviors appear when multiple droplets interact, such as repelling or attracting collisions [47, 48], orbiting pairs [12, 47, 48], crystal-like lattices [20, 52], parallel walking [4, 47], formation of ratchets and drifting rafts [24]. The interaction with boundaries is equally surprising. Reflection from walls [5], tunneling events [21], spirals around pillars [29], and scattering patterns observed as walkers go through single and double slits [7, 9, 10] all pose interesting modeling problems.

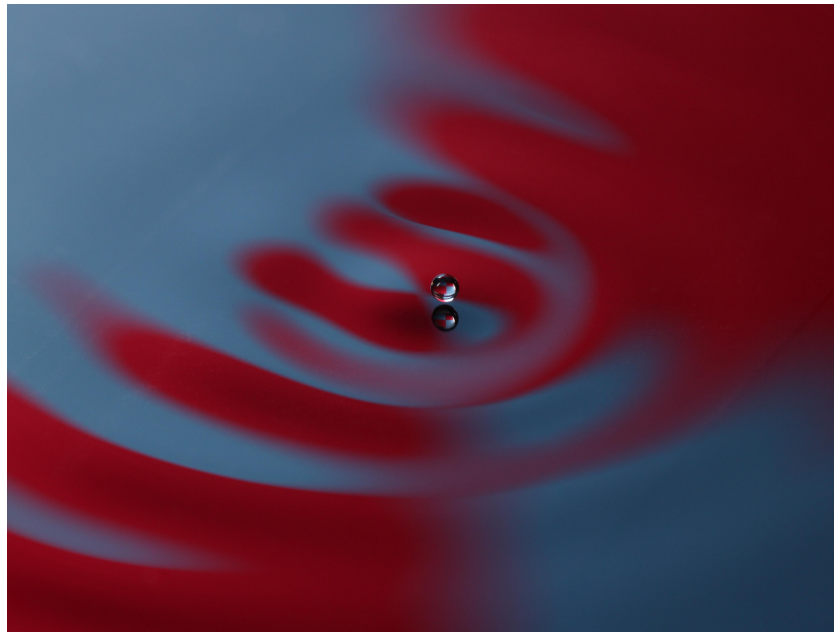


Figure 1: Walker. Photo Credit: Dan Harris.

There is one special reason to be interested in the bouncing droplets problem. A surprising amount of phenomena involving bouncers and walkers replicates behaviors of the quantum realm. These include the existence of discrete permitted orbital states [22, 27, 47, 48], unpredictable tunneling [21], dependence of mass on velocity [8]; as well as wave-like statistics for single and double slit diffraction and interference experiments [9, 10, 22], and for walkers in confined geometries [7, 9, 28, 30, 31, 34].

These similarities are particularly interesting, given that quantum mechanics is the territory of another well known association between particles and waves. Wave-droplet duos are in fact strongly reminiscent of Louis de Broglie's pilot-wave theory, a rational model of quantum mechanics [6, 7, 9, 15–18]. Moreover, studying a system whose dynamics can be observed directly might provide insight into what elements are required for quantum-like behavior. Thus, the study of hydrodynamic quantum analogs might ultimately have a say in the struggle to answer some of the most profound questions about the very fabric of our universe.

Previous theoretical works have been able to rationalize different phenomena exhibited by bouncing droplets; including different modes of bouncing and walking [23, 40, 41], trajectories in free space [43], and exotic orbits in the presence of confining force fields [42, 44–46]. Those models estimate the surface deflection using sums of Bessel functions, or of approximations to them. Another feature of any one of those models is that they include some strategy to account for the droplet surface interaction.

In the present work, we wish to evolve the surface elevation simply by imposing the classical differential relations of fluid mechanics, and thus obtain a truly spontaneous appearance of the typical features of bouncers and walkers. Part of the motivation for this task is that a surface estimate of that sort is more easily adaptable to deal with submerged topographies and boundaries which, as we mentioned above, is an important new direction in the study of bouncing droplets. A major part of the work presented here is the result of adapting Moláček and Bush' model [40, 41] of interaction between droplets and free surfaces, to our surface deflection model.

We attempted to arrive at a fully predictive model, starting only from general first principles of particle and fluid mechanics, resorting as little as possible to *a posteriori* calibrations. Comparisons to experimental results [13, 14, 53] are reported throughout this work; they were fundamental in validating the models developed here, and in establishing them as the most accurate yet available. The careful characterization of experimentally observed bouncing and walking modes is largely due to the development of a precise vibrating bath apparatus [32] and a droplet generator [33], which allow for systematic testing of mode dependence on drop size [53].

We developed this work in the mindset of the applied mathematician, who is always looking to obtain as accurate a result as possible with tools that are simple enough to be put into practice.

Outline of the Thesis. Chapter 1 presents the linear partial differential equations (PDEs) that will be used throughout this work to model the waves. Chapter 2 presents a strategy to solve a high Reynolds number (Re) limit of that system of PDEs, in the context of Faraday forcing. Chapter 3 presents a model for bouncers and walkers in which the interaction between droplet and free surface uses existing methods to estimate the forces between the drop and the bath. Chapter 4 presents an alternative model of the wave-droplet interaction, which is derived from first principles, and geometric compatibility conditions. Chapter 5 presents an improved model for surface waves which does not assume high Reynolds numbers, and matches experiments more precisely; but, in turn, is more complex to solve. A final chapter discusses the broad view of the present work, and points at possible future developments to follow it.

Most of the contents of Chapters 1, 2 and 3 were reported in the Journal of Fluid Mechanics [38], the contents of Chapters 4 and 5 are in preparation for publication.

This work also contains a few appendices which outline in greater details some of the more technical aspects of the modeling here presented.

This page was intentionally left blank.

CHAPTER 1

The Linear PDEs Fluid Model

We deduce the linear system of PDEs that will be repeatedly used along this work.

1.1 Linearized Navier-Stokes and the Helmholtz decomposition

1.1.1 PDEs and Boundary Conditions

We consider an incompressible flow with velocity $\vec{u} = [u^1, u^2, u^3]^T$ and uniform density ρ , with the fluid initially occupying the negative half-space

$$D = \{(x, y, z) ; z < 0\}. \quad (1.1)$$

This flow is described by

$$\vec{u}_t + \vec{u} \cdot \nabla \vec{u} = \vec{g} - \frac{\nabla p}{\rho} + \nu \Delta \vec{u}, \quad (1.2)$$

$$\nabla \cdot \vec{u} = 0; \quad (1.3)$$

where p is the pressure, ν the kinematic viscosity and \vec{g} the acceleration due to gravity.

The flow is subject to the kinematic boundary condition

$$\eta_t = u^3 - \vec{u}_H \cdot \nabla_H \eta, \quad (1.4)$$

where $\vec{u}_H = [u^1, u^2]^T$, $\nabla_H = [\partial_x, \partial_y]$, and $\eta = \eta(x, y)$ is the free surface elevation. This condition corresponds to the physical premise that any particle that is on the surface initially will remain

on it at all times. The interface is also subject to the dynamic boundary condition

$$\vec{\zeta} = \begin{bmatrix} \zeta^1 \\ \zeta^2 \\ \zeta^3 \end{bmatrix} = \tau \hat{n}; \quad (1.5)$$

where $\vec{\zeta}$ is the stress vector at the free surface and

$$\tau = -pI + \rho\nu \begin{bmatrix} 2u_x^1 & (u_y^1 + u_x^2) & (u_z^1 + u_x^3) \\ (u_x^2 + u_y^1) & 2u_y^2 & (u_z^2 + u_y^3) \\ (u_x^3 + u_z^1) & (u_y^3 + u_z^2) & 2u_z^3 \end{bmatrix}, \quad (1.6)$$

and

$$\hat{n} = \frac{1}{\sqrt{1 + (\eta_x)^2 + (\eta_y)^2}} \begin{bmatrix} -\eta_x \\ -\eta_y \\ 1 \end{bmatrix}; \quad (1.7)$$

for which we assume there is no tangential stress, and the normal stress just beneath the surface can be calculated from the pressure jump across it, due to surface tension; i.e. $\vec{\zeta}$ must also satisfy

$$\vec{\zeta} = (\sigma\kappa\eta - p_d) \hat{n}, \quad (1.8)$$

where σ is the surface tension coefficient, $\kappa\eta$ is twice the mean curvature operator applied on η , and p_d is the pressure above the surface.

Finally, this flow satisfies a decay condition at infinity, given by

$$\vec{u} \xrightarrow{z \rightarrow -\infty} 0. \quad (1.9)$$

Asymptotic considerations that suit the typical set up for bouncing droplet experiments lead to the following linearized system

$$\vec{u}_t = \vec{g} - \frac{\nabla p}{\rho} + \nu\Delta\vec{u}, \quad (1.10)$$

$$\nabla \cdot \vec{u} = 0; \quad (1.11)$$

in

$$D = \{(x, y, z); z < 0\}. \quad (1.12)$$

subject to the linearized kinematic boundary condition

$$\eta_t = u^3, \quad (1.13)$$

and the linearized dynamic boundary conditions

$$\begin{bmatrix} 0 \\ 0 \\ \sigma\kappa\eta - p_d \end{bmatrix} = \begin{bmatrix} \rho\nu(u_z^1 + u_x^3) \\ \rho\nu(u_z^2 + u_y^3) \\ -p + 2\rho\nu u_z^3 \end{bmatrix}, \quad (1.14)$$

on

$$\partial D = \{(x, y, z) \in \mathbb{R}^3; z = 0\}. \quad (1.15)$$

We are interested in solutions to this system that are sufficiently regular to allow for re-ordering of the derivatives, and that satisfy the differential relation even on the boundary.

Details of the asymptotic analysis leading to the linearization of the Navier-Stokes equations and the boundary conditions are given in Appendix A.

1.1.2 A Helmholtz Decomposition

We take a Helmholtz decomposition of the velocity vector field, given by

$$\vec{u} = \underbrace{\nabla\phi}_{\vec{v}} + \underbrace{\nabla \times \vec{\psi}}_{\vec{w}}, \quad (1.16)$$

i.e.

$$\begin{bmatrix} u^1 \\ u^2 \\ u^3 \end{bmatrix} = \begin{bmatrix} v^1 \\ v^2 \\ v^3 \end{bmatrix} + \begin{bmatrix} w^1 \\ w^2 \\ w^3 \end{bmatrix} = \begin{bmatrix} \phi_x \\ \phi_y \\ \phi_z \end{bmatrix} + \begin{bmatrix} \psi_y^3 - \psi_z^2 \\ \psi_z^1 - \psi_x^3 \\ \psi_x^2 - \psi_y^1 \end{bmatrix}. \quad (1.17)$$

The interested reader can find technical details regarding conditions for the existence and uniqueness of this vector field decomposition in [2, 3, 25]. For the purpose of this work, it is enough to assume that we are looking for a particular kind of solution that can be written as shown in (1.16).

We now substitute (1.16) into (1.11) to obtain

$$\nabla \cdot \vec{u} = \nabla \cdot (\nabla\phi + \nabla \times \vec{\psi}) = \underbrace{\nabla \cdot \nabla\phi}_{\Delta\phi} + \underbrace{\nabla \cdot \nabla \times \vec{\psi}}_0 = \Delta\phi = 0, \quad (1.18)$$

and (1.16) into (1.10) to obtain

$$(\nabla\phi)_t + (\nabla \times \vec{\psi})_t = \vec{g} - \frac{\nabla p}{\rho} + \nu\Delta(\nabla\phi + \nabla \times \vec{\psi}), \quad (1.19)$$

i.e.

$$\nabla(\phi_t) + \vec{w}_t = \nabla(gz) - \nabla\left(\frac{p}{\rho}\right) + \nu\nabla\underbrace{\Delta\phi}_0 + \nu\Delta\vec{w}, \quad (1.20)$$

whenever

$$\vec{g} = g(t)\hat{z}. \quad (1.21)$$

We thus obtain

$$\nabla(\phi_t) + \vec{w}_t = \nabla\left(gz - \frac{p}{\rho}\right) + \nu\Delta\vec{w}. \quad (1.22)$$

Notice that if we solve

$$\phi_t = gz - \frac{p}{\rho}, \quad (1.23)$$

and

$$w_t^i = \nu\Delta w^i, \quad i = 1, 2, 3; \quad (1.24)$$

we solve (1.22).

1.1.3 Reducing the Problem

We recall now the linearized kinematic boundary condition as given by (1.13)

$$\eta_t = u^3 = v^3 + w^3 = \phi_z + (\psi_y^3 - \psi_z^2), \quad (1.25)$$

where η is the free surface elevation.

We recall also the linearized dynamic boundary condition given by vector equation (1.14) from each component of which, combined with the corresponding component of 1.16, we obtain respectively

$$0 = (\phi_x + w^1)_z + (\phi_z + w^3)_x, \quad (1.26)$$

$$0 = (\phi_y + w^2)_z + (\phi_z + w^3)_y, \quad (1.27)$$

$$-\frac{p}{\rho} = \frac{\sigma}{\rho}\kappa\eta - 2\nu(\phi_z + w^3)_z - \frac{p_d}{\rho}; \quad (1.28)$$

equivalently,

$$0 = \phi_{zx} + (\psi_y^3 - \psi_z^2)_z + \phi_{zx} + w_x^3, \quad (1.29)$$

$$0 = \phi_{zy} + (\psi_z^1 - \psi_x^3)_z + \phi_{zy} + w_y^3, \quad (1.30)$$

$$-\frac{p}{\rho} = \frac{\sigma}{\rho}\kappa\eta - 2\nu\phi_{zz} - 2\nu w_z^3 - \frac{p_d}{\rho}. \quad (1.31)$$

We now take the derivative with respect to x and y of equations (1.29) and (1.30), respectively, and add the results to obtain

$$0 = 2\Delta_H(\phi_z) - \underbrace{(\psi_x^2 - \psi_y^1)_{zz}}_{w_{zz}^3} + \Delta_H w^3, \quad (1.32)$$

where $\Delta_H = \partial_{xx} + \partial_{yy}$. Combining (1.32) with (1.24) for $i = 3$, we obtain

$$w_t^3 = 2\nu\Delta_H (\phi_z + w^3). \quad (1.33)$$

Finally, if we combine (1.23) at $z = \eta$ with (1.31) we obtain

$$\phi_t = g\eta + \frac{\sigma}{\rho}\kappa\eta + 2\nu\Delta_H\phi - 2\nu w_z^3 - \frac{p_d}{\rho}, \quad (1.34)$$

where we used (1.18); and N is the Dirichlet to Neumann operator for Laplace's equation. A Dirichlet to Neumann map, when well defined, is simply the map that assigns to every Dirichlet boundary condition the normal derivative of the solution associated to it. Details on the definition of this operator are given in Appendix B.

We have thus obtained in equations (1.25), (1.34) and (1.33) and (1.24) for $i = 3$; the following system of linear partial differential equations that control the evolution of the surface

$$\eta_t = N\phi + w^3, \quad \text{on } z = 0; \quad (1.35a)$$

$$\phi_t = g\eta + \frac{\sigma}{\rho}\kappa\eta + 2\nu\Delta_H\phi - 2\nu w_z^3 - \frac{p_d}{\rho}, \quad \text{on } z = 0; \quad (1.35b)$$

$$w_t^3 = 2\nu\Delta_H (N\phi + w^3), \quad \text{on } z = 0; \quad (1.35c)$$

$$\Delta\phi = 0, \quad \text{for } z < 0. \quad (1.35d)$$

$$w_t^3 = \nu\Delta w^3, \quad \text{for } z < 0. \quad (1.35e)$$

Notice that the right hand side (RHS) of equation (1.35c) is just a multiple of the horizontal Laplacian of the RHS of equation (1.35a). We will address strategies to solve this system, in the context of a wave problem, in the following section.

A final remark is due before concluding this section. Notice that if the evolution of the problem approaches a steady state, equations (1.35a) yield

$$w^3 = -N\phi, \quad (1.36)$$

and so does equation (1.35c) under reasonable assumptions. Also, as a steady state is approached, equation (1.24) converges to Laplace's equation, yielding

$$p_d = \rho g\eta + \sigma\kappa\eta + 2\nu\rho (\Delta_H\phi - Nw^3), \quad (1.37)$$

and hence

$$p_d = \rho g\eta + \sigma\kappa\eta + 2\nu\rho \underbrace{(\Delta_H\phi + \phi_{zz})}_{\Delta\phi=0}; \quad (1.38)$$

thus, the system captures the correct steady state given by

$$p_d = \rho g\eta + \sigma\kappa\eta, \quad (1.39)$$

whenever it converges to a static solution.

1.2 Wave-like Solutions

We wish to find doubly periodic, traveling wave solutions to the system (1.35). More precisely, given a wave vector $\vec{k} = [k_x, k_y]$ we look for solutions of the form

$$\eta^{\vec{k}} = A(\vec{k})e^{i(\vec{k}\cdot\vec{r}-\omega t)}, \quad (1.40a)$$

$$\phi^{\vec{k}} = B(\vec{k}, z)e^{i(\vec{k}\cdot\vec{r}-\omega t)}, \quad (1.40b)$$

$$w^{3,\vec{k}} = C(\vec{k}, z)e^{i(\vec{k}\cdot\vec{r}-\omega t)}, \quad (1.40c)$$

where $\vec{r} = [x, y]$, and ω is some function of \vec{k} to be determined. Once this case is solved, we can use the linearity of system (1.35) to combine solutions of this type associated with different values of \vec{k} . Notice that the linearity will also allow us to obtain real solutions to system (1.35) to any solution of the form (1.40) the corresponding solution for $-\vec{k}$ so long as we can impose

$$A^{-\vec{k}} = \overline{A(\vec{k})}, \quad (1.41a)$$

$$B^{-\vec{k}}(z) = \overline{B(\vec{k}, z)}, \quad (1.41b)$$

$$C(-\vec{k}, z) = \overline{C(\vec{k}, z)}. \quad (1.41c)$$

We recall that ϕ satisfies Laplace's equation and hence we have

$$\Delta\phi^{\vec{k}} = \left(-k^2 + B_{zz}(\vec{k}, z)\right) e^{i(\vec{k}\cdot\vec{r}-\omega t)} = 0, \quad \forall (x, y, z) \in D, \quad (1.42)$$

where $k := |\sqrt{k_x^2 + k_y^2}|$. We thus have

$$0 = \partial_z^2 B(\vec{k}, z) - k^2 = \left(B_z(\vec{k}, z) - k\right) \left(B_z(\vec{k}, z) + k\right), \quad (1.43)$$

therefore

$$B(\vec{k}, z) = B^+(\vec{k})e^{kz} + B^-(\vec{k})e^{-kz}. \quad (1.44)$$

Similarly, we recall that each w^i satisfies heat equation (1.24), and hence we must have

$$w_t^{3,\vec{k}} - \nu \Delta w^{3,\vec{k}} = \left(-i\omega C(\vec{k}, z) - \nu C_{zz}(\vec{k}, z) + \nu k^2 C(\vec{k}, z)\right) e^{i(\vec{k}\cdot\vec{r}-\omega t)} = 0, \quad \forall (x, y, z) \in D. \quad (1.45)$$

We thus have

$$\partial_z^2 C(\vec{k}, z) - \left(k^2 + \frac{-i\omega}{\nu}\right) C(\vec{k}, z) = (\partial_z - \xi)(\partial_z + \xi) C(\vec{k}, z) = 0, \quad (1.46)$$

where

$$\xi = \sqrt{k^2 + \frac{-i\omega}{\nu}} \quad (1.47)$$

with $\Re e(\xi) \geq 0$, and therefore

$$C(\vec{k}, z) = C^+(\vec{k})e^{\xi z} + C^-(\vec{k})e^{-\xi z}. \quad (1.48)$$

We now substitute ansatz (1.40) into equation (1.35c) and obtain

$$w_t^{3,\vec{k}} - 2\nu\Delta_H N\phi^{\vec{k}} - 2\nu\Delta_H w^{3,\vec{k}} = -i\omega w^{3,\vec{k}} + 2\nu k^2 N\phi^{\vec{k}} + 2\nu k^2 w^{3,\vec{k}} = 0. \quad (1.49)$$

We then have

$$(i\omega - \alpha) w^{3,\vec{k}} = \alpha N\phi^{\vec{k}}, \quad (1.50)$$

where

$$\alpha = 2\nu k^2, \quad (1.51)$$

and, assuming

$$\alpha(k) \neq i\omega(\vec{k}), \quad (1.52)$$

we have

$$w^{3,\vec{k}} = \frac{\alpha}{i\omega - \alpha} N\phi^{\vec{k}}. \quad (1.53)$$

We now substitute (1.53) and ansatz (1.40) into (1.35a) and (1.35b) and obtain

$$-i\omega\eta^{\vec{k}} = \frac{i\omega}{i\omega - \alpha} N\phi^{\vec{k}}, \quad (1.54a)$$

$$-i\omega\phi^{\vec{k}} = \left(g + \frac{\sigma}{\rho}\kappa\right)\eta^{\vec{k}} - \alpha\phi^{\vec{k}} - 2\nu\partial_z \frac{\alpha}{i\omega - \alpha} N\phi^{\vec{k}} - \frac{p_d^{\vec{k}}}{\rho}; \quad (1.54b)$$

i.e.

$$-i\omega\eta^{\vec{k}} = -\alpha\eta^{\vec{k}} + N\phi^{\vec{k}}, \quad (1.55a)$$

$$-i\omega\phi^{\vec{k}} = \left(g + \frac{\sigma}{\rho}\kappa\right)\eta^{\vec{k}} - \left(\alpha + 2\nu\partial_z \frac{\alpha}{i\omega - \alpha} N\right)\phi^{\vec{k}} - \frac{p_d^{\vec{k}}}{\rho}; \quad (1.55b)$$

where we have assumed that the forcing $p_d = p_d^{\vec{k}} = H(\vec{k})e^{i(\vec{k}\cdot\vec{r}-\omega t)}$. The more general periodic case can be treated approximately truncating its Fourier series, each wave vector can be solved independently and the solutions can be recombined using the linearity of the equations.

Notice that the problem of the existence of a solution of the form (1.40) to the unforced system (1.35) is reduced to the existence of a solution of the following equation in $\omega(\vec{k})$

$$-i\omega \begin{bmatrix} \eta^{\vec{k}} \\ \phi^{\vec{k}} \end{bmatrix} = \begin{bmatrix} -\alpha & N \\ \left(g + \frac{\sigma}{\rho}\kappa\right) & -\left(\alpha + 2\nu\partial_z \frac{\alpha}{i\omega - \alpha} N\right) \end{bmatrix} \begin{bmatrix} \eta^{\vec{k}} \\ \phi^{\vec{k}} \end{bmatrix}. \quad (1.56)$$

Thus we need to find non-trivial solutions of

$$[M(i\omega) - (i\omega)I] \begin{bmatrix} \eta^{\vec{k}} & \phi^{\vec{k}} \end{bmatrix}^T = 0, \quad (1.57)$$

where M is given in (1.56). This is an eigenvalue-type problem, where the eigenvalue appears nonlinearly.

1.3 Infinite Depth

Notice that all the analysis that we have done so far suits the search for solutions of the form (1.40) to the system (1.35). We are interested in solutions that are bounded in all D as given by (1.12). Thus we impose

$$B^-(\vec{k}) = 0, \quad \forall \vec{k} \neq 0, \quad (1.58)$$

and

$$C^-(\vec{k}) = 0, \quad \forall \vec{k} \neq 0, \quad (1.59)$$

on (1.44) and (1.48) respectively.

Notice that, for solutions of the form (1.40) to system (1.35), we only need to calculate ϕ and η , since equation (1.53) fully determines w^3 as a function of ϕ . Moreover, in the case of ϕ we need not calculate the case $\vec{k} = 0$, since only $\nabla\phi$ is of physical relevance. As for η , the component of the zero wave vector should stay constant so as to conserve mass. This is actually the case, since equation (1.55) imposes

$$\eta_t^0 = -\alpha\eta^0 + N\phi^0 = 0; \quad (1.60)$$

which follows from the definition of α in (1.51) and the N operator applied to the constant solution to the Laplacian. In view of this, we can disregard $\vec{k} = 0$.

Now, for all $\vec{k} \neq 0$, from

$$\phi^{\vec{k}} = B^+(\vec{k})e^{kz}e^{i(\vec{k}\cdot\vec{r}-\omega t)}, \quad (1.61)$$

and

$$w^{3,\vec{k}} = C^+(\vec{k})e^{\xi z}e^{i(\vec{k}\cdot\vec{r}-\omega t)}, \quad (1.62)$$

it follows that

$$\phi_z^{\vec{k}} = kB^+(\vec{k})e^{kz}e^{i(\vec{k}\cdot\vec{r}-\omega t)} = k\phi^{\vec{k}}, \quad (1.63)$$

$$w_z^{3,\vec{k}} = \xi B^+(\vec{k})e^{kz}e^{i(\vec{k}\cdot\vec{r}-\omega t)} = \xi w_z^{3,\vec{k}}, \quad (1.64)$$

respectively. Thus, evaluating (1.63) at $z = 0$ we have

$$N\phi^{\vec{k}} = k\phi^{\vec{k}}, \quad (1.65)$$

and

$$N^H w^{3,\vec{k}} = \xi w^{3,\vec{k}}. \quad (1.66)$$

From this it follows that we can write system (1.55) as

$$-i\omega\eta^{\vec{k}} = -\alpha\eta^{\vec{k}} + k\phi^{\vec{k}}, \quad (1.67a)$$

$$-i\omega\phi^{\vec{k}} = \left(g + \frac{\sigma}{\rho}\kappa\right)\eta^{\vec{k}} - \alpha\left(1 + \frac{2\nu k\xi}{i\omega - \alpha}\right)\phi^{\vec{k}} - \frac{p_d^{\vec{k}}}{\rho}. \quad (1.67b)$$

An asymptotic limit of system (1.67) will be presented in Chapter 2. Chapter 3 uses this asymptotic approximation as part of a first and simpler approach to modeling bouncing droplets. Details on the solution of (1.67) are presented in Chapter 5. Some comments on the solution of the heat equation with the separation of variables shown in (1.40c) are presented in Appendix C.

This page was intentionally left blank.

CHAPTER 2

Slowly Decaying Waves

We develop an asymptotic theory for the case in which viscous forces are relatively small as compared to inertial forces associated with the wave motion on the surface. The model thus found is used to develop a theory for Faraday waves in media where viscous dissipation is not negligible.

2.1 An Asymptotic Limit

In section 1.3 we considered the problem of wave-like solutions of the form (1.40) to system (1.35) in the negative half space, which led us to system (1.67). Let us take that study one step further by substituting the definition of ξ as given by (1.47) into (1.67b), yielding

$$-i\omega\phi^{\vec{k}} = \left(g + \frac{\sigma}{\rho}\kappa\right)\eta^{\vec{k}} - \alpha \left(1 + \frac{2\nu k^2 \sqrt{1 + \frac{-i\omega}{\nu k^2}}}{i\omega - \alpha}\right) \phi^{\vec{k}} - \frac{p_d^{\vec{k}}}{\rho}, \quad (2.1)$$

and since $\alpha = 2\nu k^2$

$$-i\omega\phi^{\vec{k}} = \left(g + \frac{\sigma}{\rho}\kappa\right)\eta^{\vec{k}} - \alpha \left(1 - \underbrace{\frac{\sqrt{1 + 2\frac{-i\omega}{\alpha}}}{1 + \frac{-i\omega}{\alpha}}}_{\epsilon_0}\right) \phi^{\vec{k}} - \frac{p_d^{\vec{k}}}{\rho}. \quad (2.2)$$

We define

$$Re = \frac{\omega}{\alpha}, \quad (2.3)$$

and notice that

$$\epsilon_0 = \sqrt{\frac{1 - 2iRe}{1 - 2iRe - Re^2}} = \frac{1}{Re} \sqrt{\frac{\frac{1}{Re^2} - \frac{2i}{Re}}{\frac{1}{Re^2} - \frac{2i}{Re} - 1}} \xrightarrow{|Re| \rightarrow \infty} 0; \quad (2.4)$$

thus, system (1.67) approaches

$$-i\omega\eta^{\vec{k}} = -\alpha\eta^{\vec{k}} + k\phi^{\vec{k}}, \quad (2.5a)$$

$$-i\omega\phi^{\vec{k}} = \left(g + \frac{\sigma}{\rho}\kappa\right)\eta^{\vec{k}} - \alpha\phi^{\vec{k}} - \frac{p_d^{\vec{k}}}{\rho}, \quad (2.5b)$$

for high values of Re . Equivalently we have

$$\begin{bmatrix} \eta^{\vec{k}} \\ \phi^{\vec{k}} \end{bmatrix}_t = -i\omega \begin{bmatrix} \eta^{\vec{k}} \\ \phi^{\vec{k}} \end{bmatrix} = \begin{bmatrix} -\alpha & k \\ \left(g + \frac{\sigma}{\rho}\kappa\right) & -\alpha \end{bmatrix} \begin{bmatrix} \eta^{\vec{k}} \\ \phi^{\vec{k}} \end{bmatrix} - \begin{bmatrix} 0 \\ \frac{p_d^{\vec{k}}}{\rho} \end{bmatrix}. \quad (2.6)$$

Notice that Re is essentially a Reynolds number for wave phenomena, since

$$Re = \frac{\omega}{2\nu k^2} = \frac{1}{2} \frac{\omega/k}{\nu} \frac{\lambda}{2\pi} = \frac{1}{4\pi} \frac{C_p \lambda}{\nu}, \quad (2.7)$$

where C_p is phase velocity of the waves, and λ is the wave length. Thus, Re is simply a constant times the Reynolds number (characteristic speed times characteristic length over kinematic viscosity).

Taking one more linear approximation, this time for κ , we will claim that for small waves $\kappa\eta \approx \Delta_H\eta$, which combined with ansatz (1.40) yields

$$-i\omega\eta^{\vec{k}} = -\alpha\eta^{\vec{k}} + k\phi^{\vec{k}}, \quad (2.8a)$$

$$-i\omega\phi^{\vec{k}} = \left(g - \frac{\sigma}{\rho}k^2\right)\eta^{\vec{k}} - \alpha\phi^{\vec{k}} - \frac{p_d^{\vec{k}}}{\rho}. \quad (2.8b)$$

A system identical to (2.8), except for the forcing term, is presented in [37] and [19]; but, in both cases, it is derived differently.

2.2 The Dispersion Relation

The unforced ($p_d^{\vec{k}} = 0$, $g = g_0$) system (2.8) is simpler than system (1.67) in the sense that the solution of (2.6) involves a typical eigenvalue problem, and not a generalization of it. In fact,

equation (2.6) yields an explicit expression for ω as a function of \vec{k} through the solution of

$$\det \begin{pmatrix} i\omega - \alpha & k \\ -\left(-g_0 + \frac{\sigma}{\rho}k^2\right) & i\omega - \alpha \end{pmatrix} = 0, \quad (2.9)$$

i.e.

$$(i\omega - \alpha)^2 = -k \left(-g_0 + \frac{\sigma}{\rho}k^2 \right), \quad (2.10)$$

thus we have

$$-i\omega = -\alpha \pm i\sqrt{k \left(-g_0 + \frac{\sigma}{\rho}k^2 \right)}. \quad (2.11)$$

Recall that, by (2.15), $\vec{g} = g(t)\hat{z}$, thus normal gravity implies $\vec{g} = g_0\hat{z}$, with $g_0 < 0$, rendering

$$-g_0 + \frac{\sigma}{\rho}k^2 > 0. \quad (2.12)$$

Relation (2.12) together with equation (2.11) imply that, in this simplified model, the temporal decay of waves depends only on ν and k ; and that wave velocity doesn't depend on ν . This is clear, since we now know that our wave-like solutions of $\eta^{\vec{k}}$ are of the form

$$\eta^{\vec{k}} = A(\vec{k})e^{-\alpha t}e^{i(\vec{k}\cdot\vec{r} \mp \sqrt{k(-g_0 + \frac{\sigma}{\rho}k^2)})}, \quad (2.13)$$

and that they are similar for $\phi^{\vec{k}}$ and $w^{3,\vec{k}}$.

2.2.1 A Consistency Check

The value of the Reynolds number Re should in principle be calculated using the solution of the system before the simplifications for high Reynolds numbers were made (see Chapter 5). Still, the least we can be expected to do is to see what $|Re|$ is as predicted by the waves that this model produces. Thus, we combine equations (2.3), (2.11) and (1.51) to obtain

$$|Re| = \frac{|\omega|}{\alpha} = \frac{\sqrt{\alpha^2 + k \left(-g_0 + \frac{\sigma}{\rho}k^2 \right)}}{\alpha} = \sqrt{1 + \frac{\omega_I}{\alpha^2}}, \quad (2.14)$$

where ω_I corresponds to the dispersion relation for an inviscid system. We thus expect that this asymptotic approximation works better in scenarios where ω_I is comparatively larger than α . Notice that $|Re| > 1$ in all cases, at least as predicted by this asymptotic model.

2.3 Faraday Waves

We can model surface waves on a vertically oscillating bath by adding a time-dependent gravity in the frame of reference of the bath. More precisely, we need to modify the usual gravity by subtracting from it the acceleration of the shaken container. For the case of simple harmonic motion of the bath we have

$$g(t) = g_0(1 - \Gamma \cos(\omega_0 t)), \quad (2.15)$$

where $g_0 \approx -980 \text{ cm/s}^2$, $\gamma = g_0\Gamma$ is the amplitude of the oscillatory acceleration imparted to the container, and ω_0 is the angular frequency of the shaking. This particular choice of initial phase is done so as to have the container at its maximum height at $t = 0$.

Under these conditions we can rewrite system (2.8) as

$$V_t = MV + L(t)V + P(t), \quad (2.16)$$

where

$$V = \begin{bmatrix} \eta^k \\ \phi^k \end{bmatrix}, \quad (2.17)$$

$$M = \begin{bmatrix} -\alpha & k \\ -\left(-g_0 + \frac{\sigma}{\rho}k^2\right) & -\alpha \end{bmatrix}, \quad (2.18)$$

$$L = \begin{bmatrix} 0 & 0 \\ -g_0\Gamma \cos(\omega_0 t) & 0 \end{bmatrix}, \quad (2.19)$$

and

$$P = \begin{bmatrix} 0 \\ -\frac{p_d^k}{\rho} \end{bmatrix}. \quad (2.20)$$

To integrate equation (2.16) it is convenient to consider first the use of the integrating factor e^{-tM} , so as to obtain

$$e^{-tM}V_t - e^{-tM}MV = e^{-tM}(L(t) + P(t)), \quad (2.21)$$

i.e.

$$(e^{-tM}V)_t = e^{-tM}(L(t) + P(t)). \quad (2.22)$$

An alternative variable change makes use of complex variables by defining

$$s^{\vec{k}} = \eta^{\vec{k}} + i \frac{k}{\beta} \phi^{\vec{k}}, \quad (2.23)$$

where

$$\beta = \sqrt{k \left(-g_0 + \frac{\sigma}{\rho} k^2 \right)}. \quad (2.24)$$

Notice that we then have

$$\dot{s}_t^{\vec{k}} = \eta_t^{\vec{k}} + i \frac{k}{\beta} \phi_t^{\vec{k}} = -\alpha \eta^{\vec{k}} + k \phi^{\vec{k}} - i \frac{k}{\beta} \frac{\beta^2}{k} \eta^{\vec{k}} - i \frac{k}{\beta} \alpha \phi^{\vec{k}} - i \frac{k}{\beta} g_0 \Gamma \cos(\omega_0 t) \eta^{\vec{k}} - i \frac{k}{\beta} \frac{p_d^{\vec{k}}}{\rho}, \quad (2.25)$$

i.e.

$$\dot{s}_t^{\vec{k}} = -\alpha \left(\eta^{\vec{k}} + i \frac{k}{\beta} \phi^{\vec{k}} \right) - i \beta \left(\eta^{\vec{k}} + i \frac{k}{\beta} \phi^{\vec{k}} \right) - i \frac{k}{\beta} g_0 \Gamma \cos(\omega_0 t) \eta^{\vec{k}} - i \frac{k}{\beta} \frac{p_d^{\vec{k}}}{\rho}, \quad (2.26)$$

hence

$$e^{(\alpha+i\beta)t} s_t^{\vec{k}} + e^{(\alpha+i\beta)t} (\alpha + i\beta) s^{\vec{k}} = -i \frac{k}{\beta} e^{(\alpha+i\beta)t} \left(g_0 \Gamma \cos(\omega_0 t) \eta^{\vec{k}} - \frac{p_d^{\vec{k}}}{\rho} \right), \quad (2.27)$$

we thus have

$$\left(e^{(\alpha+i\beta)t} s_t^{\vec{k}} \right)_t = -i \frac{k}{\beta} e^{(\alpha+i\beta)t} \left(g_0 \Gamma \cos(\omega_0 t) \eta^{\vec{k}} - \frac{p_d^{\vec{k}}}{\rho} \right). \quad (2.28)$$

2.4 The Faraday Threshold

We now try to find an approximate wave-like subharmonic solution to system (2.16). This is inspired in the simulations results we have observed for this physical system, where we see that the subharmonic component dominates the solution.

We wish to find approximate solutions of the form

$$\eta^{\vec{k}} = E^+ e^{(v+i\frac{\omega_0}{2})t} e^{\vec{k} \cdot \vec{r}} + E^- e^{(v-i\frac{\omega_0}{2})t} e^{\vec{k} \cdot \vec{r}}, \quad (2.29a)$$

$$\phi^{\vec{k}} = F^+ e^{(v+i\frac{\omega_0}{2})t} e^{\vec{k} \cdot \vec{r}} e^{kz} + F^- e^{(v-i\frac{\omega_0}{2})t} e^{\vec{k} \cdot \vec{r}} e^{kz}; \quad (2.29b)$$

for the system

$$\eta_t^{\vec{k}} = -2\nu \Delta \eta^{\vec{k}} + k \phi^{\vec{k}}, \quad (2.30a)$$

$$\phi_t^{\vec{k}} = \left(g_0 - g_0 \Gamma \cos(\omega_0 t) + \frac{\sigma}{\rho} k^2 \right) \eta^{\vec{k}} - 2\nu \Delta \phi^{\vec{k}}. \quad (2.30b)$$

The Faraday threshold should correspond to the minimum value of Γ for which we can find non-trivial, neutrally stable solutions; i.e. with $v = 0$ in system (2.30).

We thus substitute ansatz (2.29), at $z = 0$, into (2.30a). Separating frequencies by their sign,

we obtain

$$\left(v + i\frac{\omega_0}{2}\right) E^+ e^{i\frac{\omega_0}{2}t} = -2\nu k^2 E^+ e^{i\frac{\omega_0}{2}t} + k F^+ e^{i\frac{\omega_0}{2}t}, \quad (2.31a)$$

$$\left(v - i\frac{\omega_0}{2}\right) E^- e^{-i\frac{\omega_0}{2}t} = -2\nu k^2 E^- e^{-i\frac{\omega_0}{2}t} + k F^- e^{-i\frac{\omega_0}{2}t}; \quad (2.31b)$$

i.e.

$$\left(v + i\frac{\omega_0}{2}\right) E^+ = -2\nu k^2 E^+ + k F^+, \quad (2.32a)$$

$$\left(v - i\frac{\omega_0}{2}\right) E^- = -2\nu k^2 E^- + k F^-. \quad (2.32b)$$

Proceeding analogously with (2.30b)

$$\left(v + i\frac{\omega_0}{2}\right) F^+ e^{i\frac{\omega_0}{2}t} = -\left(-g_0 + \frac{\sigma}{\rho} k^2\right) E^+ e^{i\frac{\omega_0}{2}t} - 2\nu k^2 F^+ e^{i\frac{\omega_0}{2}t} - \frac{g_0 \Gamma}{2} E^- e^{i\frac{\omega_0}{2}t}, \quad (2.33a)$$

$$\left(v + i\frac{\omega_0}{2}\right) F^- e^{-i\frac{\omega_0}{2}t} = -\left(-g_0 + \frac{\sigma}{\rho} k^2\right) E^- e^{-i\frac{\omega_0}{2}t} - 2\nu k^2 F^- e^{-i\frac{\omega_0}{2}t} - \frac{g_0 \Gamma}{2} E^+ e^{-i\frac{\omega_0}{2}t}. \quad (2.33b)$$

Where we used

$$\cos(\omega_0 t) = \frac{e^{i\omega_0 t} + e^{-i\omega_0 t}}{2} \quad (2.34)$$

and we neglected the terms $-\frac{g_0 \Gamma}{2} E^+ e^{i3\frac{\omega_0}{2}t}$ and $-\frac{g_0 \Gamma}{2} E^- e^{-i3\frac{\omega_0}{2}t}$ in equations (2.33a) and (2.33b) respectively. These terms in fact show that an exact solution of the form (2.29) is impossible. This is because a forcing of the form $g_0 \Gamma e^{\pm\omega_0 t}$, which is multiplied by η , will always introduce one frequency that is larger by ω_0 than all those present in any ansatz that combines merely a finite number of frequencies. In other words, we disregarded frequencies that are higher than the subharmonic. That truncation criterium is based on what can be observed in our simulations for values near the numerical instability threshold, in which we see that the subharmonic component is known to largely dominate the surface wave dynamics.

Equations (2.30b) yields

$$\left(v + i\frac{\omega_0}{2}\right) F^+ = -\left(-g_0 + \frac{\sigma}{\rho} k^2\right) E^+ - 2\nu k^2 F^+ - \frac{g_0 \Gamma}{2} E^-, \quad (2.35a)$$

$$\left(v - i\frac{\omega_0}{2}\right) F^- = -\left(-g_0 + \frac{\sigma}{\rho} k^2\right) E^- - 2\nu k^2 F^- - \frac{g_0 \Gamma}{2} E^+. \quad (2.35b)$$

Equations (2.32) and (2.35) reduce the problem to finding a non-trivial solution to system

$$QR = 0; \quad (2.36)$$

where

$$R = \begin{bmatrix} E^+ \\ F^+ \\ E^- \\ F^- \end{bmatrix}, \quad (2.37)$$

and

$$Q = \begin{bmatrix} -2\nu k^2 - (v + i\frac{\omega_0}{2}) & k & 0 & 0 \\ -\left(-g_0 + \frac{\sigma}{\rho}k^2\right) & -2\nu k^2 - (v + i\frac{\omega_0}{2}) & -\frac{g_0\Gamma}{2} & 0 \\ 0 & 0 & -2\nu k^2 - (v - i\frac{\omega_0}{2}) & k \\ -\frac{g_0\Gamma}{2} & 0 & -\left(-g_0 + \frac{\sigma}{\rho}k^2\right) & -2\nu k^2 - (v - i\frac{\omega_0}{2}) \end{bmatrix}. \quad (2.38)$$

Solving $\det(Q) = 0$, after some basic algebraic manipulations we obtain

$$\left[\left(v + 2\nu k^2 + i\frac{\omega_0}{2} \right)^2 + k \left(-g_0 + \frac{\sigma}{\rho}k^2 \right) \right] \left[\left(v + 2\nu k^2 - i\frac{\omega_0}{2} \right)^2 k \left(-g_0 + \frac{\sigma}{\rho}k^2 \right) \right] = \frac{g_0^2 \Gamma^2}{4} k^2. \quad (2.39)$$

Given the set of physical parameters g_0 , ν , σ , ρ , and ω_0 , relation (2.39) serves two main proposes. First, if we make $v = 0$ we can obtain

$$\Gamma^2 = \frac{4}{g_0^2 k^2} \left[\left(2\nu k^2 + i\frac{\omega_0}{2} \right)^2 + k \left(-g_0 + \frac{\sigma}{\rho}k^2 \right) \right] \left[\left(2\nu k^2 - i\frac{\omega_0}{2} \right)^2 + k \left(-g_0 + \frac{\sigma}{\rho}k^2 \right) \right], \quad (2.40)$$

which is a prediction for an approximate value of Γ with which we need to shake the bath so as to observe neutrally stable surface waves. This, in turn, can be solved for all values of k , thus defining an upper bound curve in the $k - \Gamma$ plane, which bounds the stability region. A minimum value of Γ on the curve described as k takes all positive values will be our prediction for the Faraday threshold. The value of k that minimizes Γ will determine the prediction for the Faraday wavelength.

The second use of expression (2.39) of interest to the present work is made evident when we impose a value of Γ at which the experiment will be carried out and then consider a perturbation of wave number k . The real part of v will be a prediction of the growth rate of the waves, and its imaginary part will predict the expected deviation from the subharmonic frequency.

A concluding remark for this section is due. It is possible to characterize the stability of system (2.30) in a more rigorous way using the Poincaré map derived from Floquet theory, since (2.30) is a system of linear ODEs with periodic coefficients. This alternative requires the use of numerical integration through one forcing period. We have in fact done so and obtained results with less than 1% in error every case we tested. The arguments made in the present section can be found

in Appendix A of [38].

2.4.1 Some Examples and a Correction Factor

In [53] we find experimental determinations of the Faraday threshold value for three different parameter regimes. We will see how well the predictions of our asymptotic model compares to the laboratory measurements. Naturally, all experiments in [53] are carried out with $g_0 \approx -980 \text{ cm/s}^2$.

One parameter set, studied in [53], is given by $\nu = .5 \text{ St}$, $\rho = 0.965 \text{ g/cm}^3$, $\sigma = 20.8 \text{ Dyne/cm}$ and $\omega_0 = 2\pi \cdot 50 \text{ rad/s}$. For this set up, they determined $\Gamma_F = 4.23 \pm 0.05$, and the wave number as predicted by the standard capillary-gravity dispersion relation for subharmonic waves,

$$\left(\frac{\omega_0}{2}\right)^2 = |g_0|k_F + \frac{\sigma}{\rho}k_F^3, \quad (2.41)$$

which in this case corresponds to $\lambda_F = 0.70 \text{ cm}$. For the same conditions, the theoretical predictions of our model estimate $\Gamma_F^p = 4.99$ with $\lambda_F^p = .85 \text{ cm}$; i.e. they over predict Γ by 18% and k_F by 21%.

The other two regimes are given by $\nu = 0.2 \text{ St}$, $\rho = 0.949 \text{ g/cm}^3$, $\sigma = 20.6 \text{ Dyne/cm}$ and $\omega_0 = 2\pi \cdot 70 \text{ rad/s}$, and $\omega_0 = 2\pi \cdot 80 \text{ rad/s}$ respectively. The corresponding thresholds are found with $\Gamma_F = 3.33 \pm 0.05$ ($\lambda_F = 0.53 \text{ cm}$), and $\Gamma_F = 4.22 \pm 0.05$ ($\lambda_F = 0.48 \text{ cm}$). For the 70 Hz set up, our prediction is $\Gamma_F^p = 4.10$ and $\lambda_F^p = 0.56 \text{ cm}$; thus yielding errors of 23% and 5.6%, respectively. For the 80 Hz one it was $\Gamma_F^p = 5.18$ and $\lambda_F^p = 0.51 \text{ cm}$, i.e. errors of 23% and 6.2%, respectively. It is not clear why predictions worsen as ω increases, since in theory the approximation should improve, it does appear to be linked to the high Re approximation itself and not to the prediction of the Faraday threshold obtained disregarding the third harmonic term, since the same happens when predicting with Floquet theory.

We can easily introduce a viscosity correction, that will reduce the value of the Faraday threshold to the experimentally observed value. This correction does not appreciably change the value of λ_F^p . We will focus particularly in the 0.2 St and 80 Hz system, since this is the one for which there exists the most experimental data. Figure (2.1) illustrates the predictions with and without the correction, for that regime. With a corrected viscosity of

$$\nu^* = 0.8025 \nu \quad (2.42)$$

we can match the experimentally reported value of Γ_F with a 4.59% over prediction in wavelength.

Moreover, we ran a simulation of 20 seconds of physical time for the same set up and at different values of Γ , calculating with the same mesh for k and an initially flat Fourier spectrum. We confirmed that the predictions based on equation (2.40) correspond to the minimal value of Γ found to produce growth at some k (i.e. Γ_F), with precision of 0.01, and this growth occurs at the same mesh value of k_F . This indicates that equation (2.40) is in fact a good predictor of the Faraday threshold in this model.

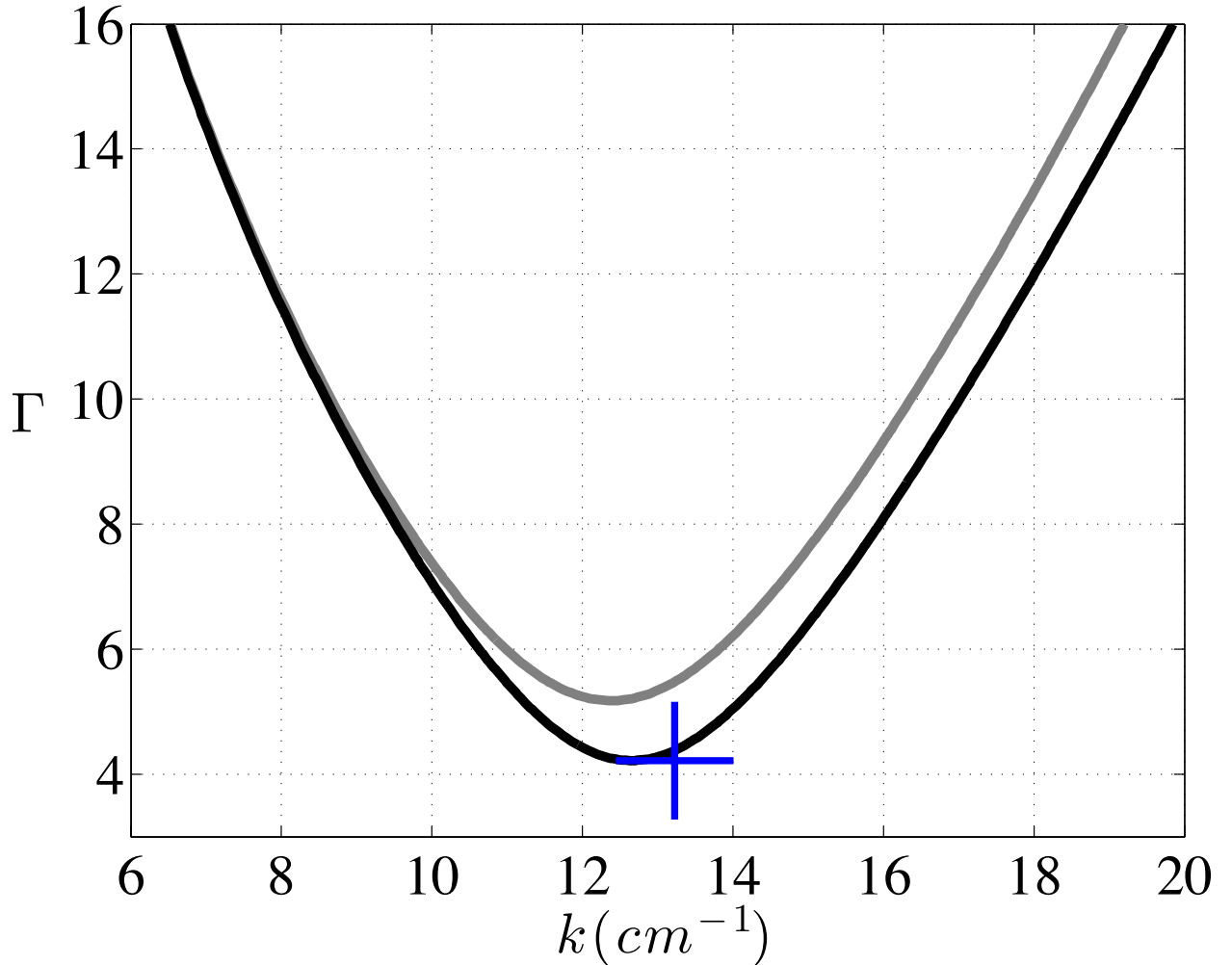


Figure 2.1: Correction of the viscosity to match the experimental Faraday threshold. The gray curve shows the value of Γ for neutral stability, as predicted by equation (2.40) in the parameter regime given by $\nu = 0.2 \text{ } St$, $\rho = 0.949 \text{ } g/cm^3$, $\sigma = 20.6 \text{ } dyne/cm$ and $\omega_0 = 2\pi \cdot 80 \text{ } rad/s$. The black curve corresponds to the same equation but with $\nu^* = 0.8025 \nu$, for viscosity. The blue + marker shows the experimental value as reported in [53].

An improved prediction of the Faraday threshold is obtained by the methods developed in Chapter 5.

This page was intentionally left blank.

CHAPTER 3

Generation and Propagation of a Hydrodynamic Pilot-Wave

We present a model of the hydrodynamic pilot-wave system. Waves are generated by repeated pressure forcing of the fluid surface. We combine the fluid model developed in Chapter 2 with existing methods to predict droplet motion and produce the most versatile walker model yet.

3.1 Droplet Dynamics

We follow [40] and [41], where a model of droplet surface interaction is presented. This model was designed to be used with the surface shape estimate introduced in the same works. Specifically, the shape of the interface was approximated by adding standing waves in the form of Bessel functions. The effect of a droplet impact on the bath was modeled by the addition of a new Bessel function at the end of the impact; meaning that the bath was not locally deformed during the impact, but rather only globally modified after it. Hence they obtain a trajectory for the droplet that actually intersects the bath at every impact. Their analysis of droplet penetration yields the reaction force of the bath on the droplet.

We, in turn, decided to model the effect of the droplet on the bath by means of a pressure field on the free surface. This pressure field is supported on a given area under the drop, and its spatial integral corresponds at each instant to the total force that the bath applied on the drop. To calculate this force, we adapt the spring model developed in [40]. We apply the pressure field to the surface of the fluid and thus actually deform it locally. We then let the fluid equations evolve without presuming any global features. Instead we expect them to arise spontaneously.

In the model here developed, droplet deformation is neglected for the purpose of calculating the trajectory of points of the droplet, hence we assume that the lowest point of the drop is one radius below its center of mass.

3.1.1 The Hypothetical Surface

Any spring model requires a deflection value to predict the applied force. In [40] and [41] the spring's deformation is simply taken to be the penetration depth of the drop's lowest point beneath the free surface that is computed accounting for all previous impacts.

To adapt this model of droplet motion to our surface waves, which are locally deformed by the falling droplet, we needed to find a way to compute the surface as if the ongoing hit was not occurring. This surface would then be compared to the position of the lowest point of the drop. We hence resort to an auxiliary surface, which will be different from the actual interface of the bath only during contact. We call this the hypothetical surface, and it is simply obtained by computing the surface evolution without applying the pressure of the ongoing impact.

To be consistent with the spring model, the force deduced from its use should be normal to the hypothetical surface. Thus, this auxiliary surface will in fact have two uses. The first is to calculate droplet penetration and the second is to obtain the gradient at the point of contact, yielding the horizontal component of the wave force.

3.1.2 The Equations of Droplet Motion

Following [40] and [41] we assume the droplet's motion is governed by

$$z_{tt} = g(t), \quad (3.1)$$

and

$$m\vec{r}_{tt} = -c_{St}\vec{r}_t, \quad (3.2)$$

when in flight; and by

$$\left(1 + \frac{c_3}{\ln^2 \left| \frac{c_1 R_0}{z - \bar{\eta}} \right|}\right) m z_{tt} + \frac{4\pi\nu\rho R_0 c_2}{3 \ln \left| \frac{c_1 R_0}{z - \bar{\eta}} \right|} (z - \bar{\eta})_t + \frac{2\pi\sigma}{\ln \left| \frac{c_1 R_0}{z - \bar{\eta}} \right|} (z - \bar{\eta}) = mg(t), \quad (3.3)$$

and

$$m\vec{r}_{tt} + \left(c_4 \sqrt{\frac{\rho R_0}{\sigma}} F(t) + c_{St}\right) \vec{r}_t = -F(t) \nabla \bar{\eta}(\vec{r}), \quad (3.4)$$

during contact.

Above, (x, y, z) is the position of the lowest point of the drop, $\vec{r} = (x, y)$, $c_{St} = 6\pi R_0 \mu_{air}$ is the coefficient for Stoke's drag, and $\bar{\eta}$ is the elevation of the hypothetical surface. Coefficients c_1 , c_2 , c_3 and c_4 are given in [40] and [41]. There they find the appropriate values of these coefficients for their Bessel function model. As a comment, we note that those values, could in principle be somewhat different in our model.

Equations (3.1), (3.2), (3.3) and (3.4) describe the motion of the drop in the frame of reference of the level of the vibrating bath.

In writing the equations that model motion during contact, we assume that the normal is

almost vertical, and thus apply the whole force vertically and $-F\nabla\bar{\eta}$ in the horizontal direction.

3.2 Forcing the Waves

Combining the use of the hypothetical surface with equation (3.3) we obtain a prediction for the value of the total force applied to the fluid during contact. We then use a constant pressure distribution applied in a circular area; which is determined as a linear approximation to the area of the basis of an spherical cap of height $\bar{\eta} - z$. More specifically, the area of the base of an spherical cap on the drop is given by

$$A_S = \pi (R_0^2 - (R_0 - (\bar{\eta} - z))^2) = \pi (2R_0(\bar{\eta} - z) - (\bar{\eta})^2), \quad (3.5)$$

and we take

$$A_C = 2\pi R_0 (\bar{\eta} - z). \quad (3.6)$$

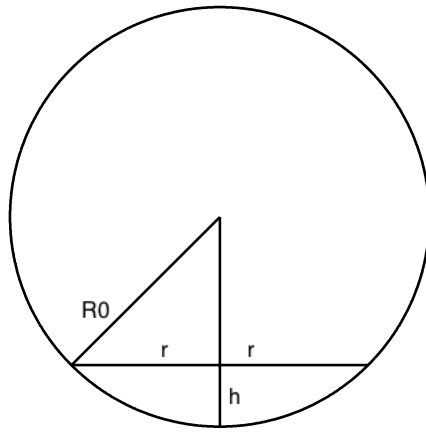


Figure 3.1: Basis for the estimate of the contact area under the drop for each value of penetration $h = \bar{\eta} - z$. The actual estimate is the linearization around zero of the area that is shown to have radius r in this diagram.

Figure 3.1 shows a central cross section of the drop which is used for our estimate of the pressed area.

We also impose the constraint that the radius of the pressed area can be at most equal to $R_0/3$. If (3.6) predicts a bigger area we use $\pi (R_0/3)^2$. When implementing the method we also impose the radius of the pressed area be at least bigger than the resolution of the spatial mesh; i.e. in a regular square mesh, the smallest possible number of pressed points is 5.

We decompose

3.3 Bouncers and Walkers

To implement this method we use an explicit finite differences scheme in time, and a spectral method in space. Thus we are solving the case of the doubly periodical spatial domain.

We use a square domain of periodicity, of 10 *cm* of side, where we fit 1024 mesh intervals. On this mesh we take the fast Fourier transform (FFT) of the pressure, as estimated by the methods described above, and thus reduce the problem to a family of problems of the form given in (2.16). More specifically, for each wave vector we need to solve

$$\eta_t^{\vec{k}} = -\alpha \eta^{\vec{k}} + k \phi^{\vec{k}}, \quad (3.7a)$$

$$\phi_t^{\vec{k}} = \left(g_0 - \frac{\sigma}{\rho} k^2 \right) \eta^{\vec{k}} - \alpha \phi^{\vec{k}} - g_0 \Gamma \cos(\omega_0 t) \eta^{\vec{k}} - \frac{p_d^{\vec{k}}}{\rho}. \quad (3.7b)$$

We complexify the equations as shown in (2.28), and solve in time using a mid point rule. The time step we use varies; in most experiments we initialize the simulations with 20 time steps per forcing period, and later switch up to 160. This is done to speed up the calculations on the initial transient leading to periodicity in most bouncers.

We initialize our simulations by letting the drop fall from a height of 0.5 *cm*, with a horizontal velocity of 0.5 *cm/s*. We try systematically different radii and different shaking amplitudes; and then compare the modes of bouncing we obtained to the experimental data reported in [53]. The model is able to capture many of the experimentally reported bouncing modes.

We run all simulations for the same set of fluid parameters, which match the 20 *cSt*, 80 *Hz* regime tested in [53]; namely $\nu = 0.2$ *cSt*, $\nu^* = 0.8025 * 0.2$ *cSt*, $\rho = 0.949$ *gr/cm*³, $\sigma = 20.6$ *dyne/cm*. We also use a fixed forcing frequency $\omega_0 = 2\pi 80$ *rad/s*, and a fixed value of gravitational acceleration $g_0 = -980$ *cm/s*². Thus we only vary drop size and shaking amplitude.

To use equations (3.1) and (3.2) we explored values of coefficients c_1 , c_2 and c_3 in the vicinity of those predicted in [40], and settled on a combination that produced relatively high waves and allowed for walking to take place; namely $c_1 = 0.7$, $c_2 = 8$, $c_3 = 0.7$. These values are kept constant for all experiments. The value of c_4 was chosen to match the walking threshold for a walker of $\Omega = 0.8$, i.e. $c_4 = 0.13$.

Following the criteria used in [40, 41, 53], we classify drops in terms of their vibration number

$$\Omega = \omega_0 \sqrt{\rho R_0^3 / \sigma}, \quad (3.8)$$

and measure the amplitude of the oscillatory acceleration as a fraction of the amplitude at the Faraday threshold. Thus we present the the bouncing modes obtained in our simulations in the $\Gamma/\Gamma_F - \Omega$ plane.

We classify modes following [40], with an ordered pair (m, n) ; where, m stands for the period of vertical motion of the drop measured in forcing periods, and n counts how many drop-surface contacts take place during this period. For instance, a (2,1) mode is a subharmonic bouncing mode (i.e. resonant with the waves) in which the drop interacts with the surface only once per

period of motion.

Figure 3.2 shows in more detail some of the bouncing modes obtained. Modes are identified by looking at the periodicity of the vertical motion of the lowest point of the drop. Notice that this model does not enforce a match between the vertical motion of the drop and the fluid beneath it; rather, it imposes a force balance, based on the spring model of [41], and allows for the drop and surface to evolve accordingly. Thus the agreement between the motion of the surface and the drop can be considered a measure of the accuracy of the spring model.

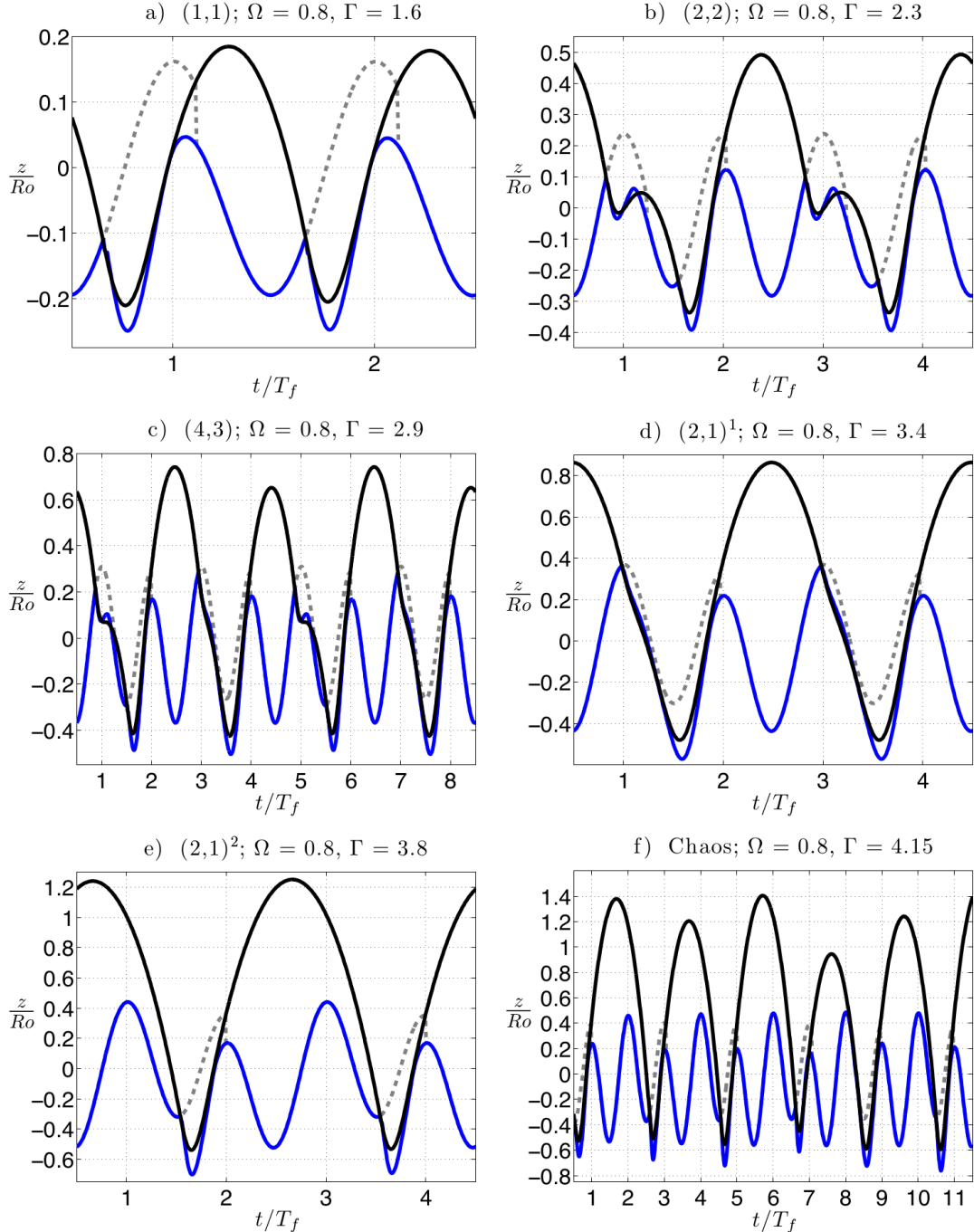


Figure 3.2: Bouncing and walking modes observed for $\Omega = 0.8$. The black curve shows the lowest point of the drop, the blue curve shows the surface beneath it, and the gray dashed curve shows the hypothetical surface.

We also impose a no suction constraint, following [40, 41]; i.e., we only apply positive pressure on the fluid, and upward force on the drop. In other words, the force that is effectively applied is the maximum of 0 and F , as estimated from finding the acceleration from equation (3.3) and subtracting the effect of gravity from it.

It is important to highlight that the drop is considered to be in contact so long as its lowest point is under the hypothetical surface (shown in the gray dashed line in Figure 3.2). Thus, even though the no-suction restriction might cause the drop to be in free fall for a certain part of the contact, the hypothetical surface is not re-initialized so long as the drop does not go completely over it; i.e. the contact is not considered to be interrupted by this free fall interval.

Figure 3.3 shows a $\Gamma/\Gamma_F - \Omega$ phase diagram of the bouncers and walkers predicted by this model, as well as a comparison to the experimental data reported on [53].

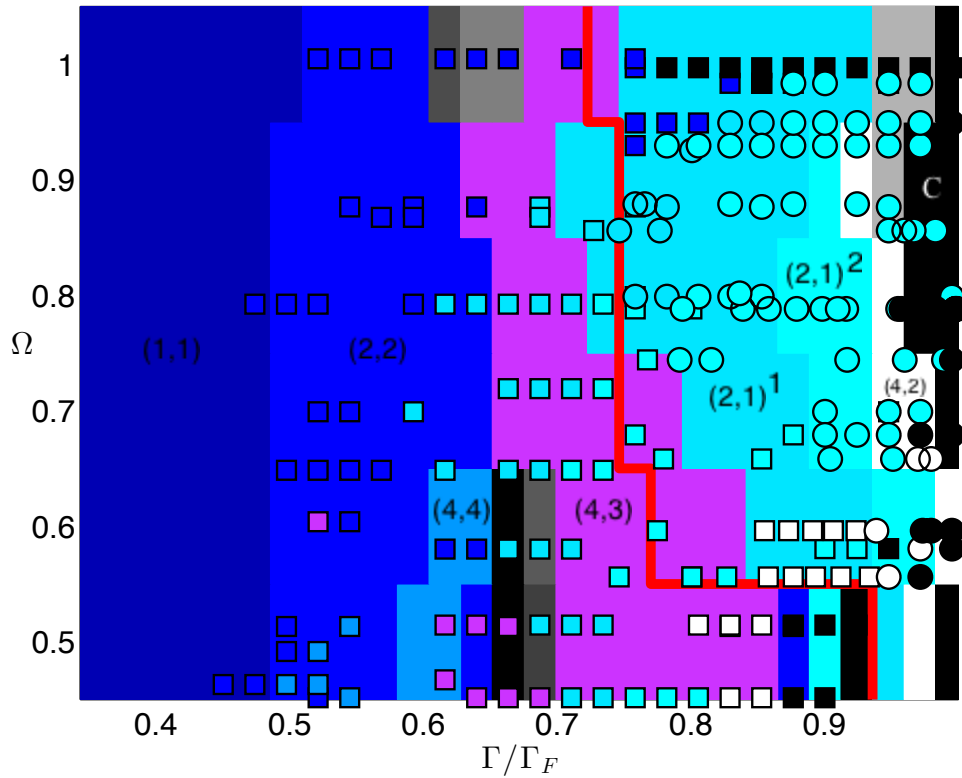


Figure 3.3: Regime diagram of bouncers. The background tiling is color coded according to the mode of bouncing. C stand for *chaos*, and shades of gray were used for bouncers with a period longer than 5 times that of the bouncing. The bullets show experimentally observed bouncers, reported in [53]; the color coding of the bullets is the same as that of the background. The red vertical line corresponds to the walking threshold; i.e. for values of Γ to the right of the red curve, the initial velocity of the walkers does not drop to zero, as it does for values of Γ to the left of that curve.

Some multiplicity of bouncing and walking states for the same parameter regime is expected from the experimental results, as is hinted at by the overlap between some of the experimental bullets in Figure 3.3. We have seen that we can obtain both phenomena with this model but a more extensive exploration of them remains to be done, and so is the case with experiments.

Figure 3.4 shows the transition in velocity, as well as in phase of the shaking at the moment of impact (i.e. when contact starts) for $\Omega = 0.8$, for different values of Γ . Notice that, in this figure, the black curve has multiple values whenever the droplet contacts the surface more than once at each period of its vertical motion. The chaotic region shows no regularity in bouncing phase of impact, and thus the black curve can not be defined in that region.

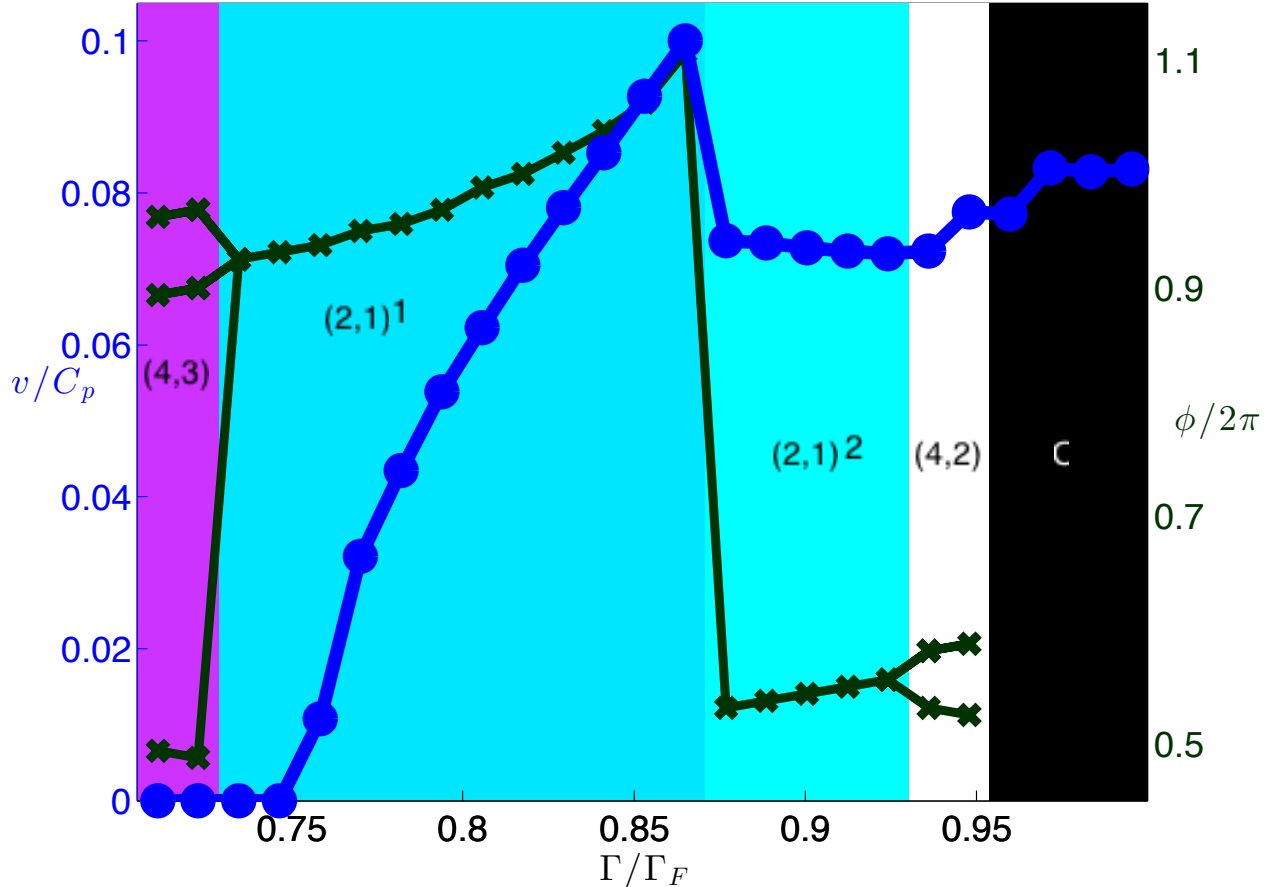


Figure 3.4: Walking bifurcation for $\Omega = 0.8$. The background is color coded according to the mode of bouncing, using the coding of Figure 3.3. The black curve corresponds to phase of impact ϕ ; and the blue curve to walker speed, normalized by the phase velocity of the Faraday waves C_p .

Also notice that there is a clear jump in walking speed separating the $(2, 1)^1$ mode from the $(2, 1)^2$ mode of walking. Figure 3.4 makes a clear case for the existence of a forbidden region of phases between the two modes. This distinction can also be noticed in Figure 3.2, where it is easy to see that in the $(2, 1)^1$ mode the drop impacts the surface as it is coming down, whereas in the $(2, 1)^2$ it hits it as it is going up. The $(2, 1)^2$ mode is also characterized by its much shorter contact.

The black curve on Figure 3.4 requires one further comment to completely explain its branches. In the region corresponding to the $(4, 3)$ mode, the tallest branch corresponds to the beginning of the longer contact (shown on the center left panel of Figure 3.2). This contact continues for roughly one forcing period and is followed by a flight of approximately the same

duration. Thus, approximately two full forcing period pass before we attain a second contact, which corresponds to the second to tallest branch of the (4, 3) mode region of Figure 3.4. At that moment, a short contact of about a quarter of a forcing period takes place which is followed by a similarly long flight and then, finally, the impact that corresponds to the lowest branch starts. A similar situation, but a much simpler one takes place in the (4, 2) mode region of the same figure.

3.3.1 The Transient of a Walker

As mentioned above, all bouncing droplets simulations were initialized with the same initial horizontal velocity and dropped from the same height, and at the same phase of the shaking. We observe a transient regime that gives way to the corresponding steady modes of bouncing. Figure 3.5 shows a typical example of the evolution of velocity for a walker. Velocity decreases with the first contacts, and then proceeds to adjust itself to the steady value. In the case of a bouncer, velocity simply continues to drop to zero. The inset in Figure 3.5 shows how velocity changes during contact.

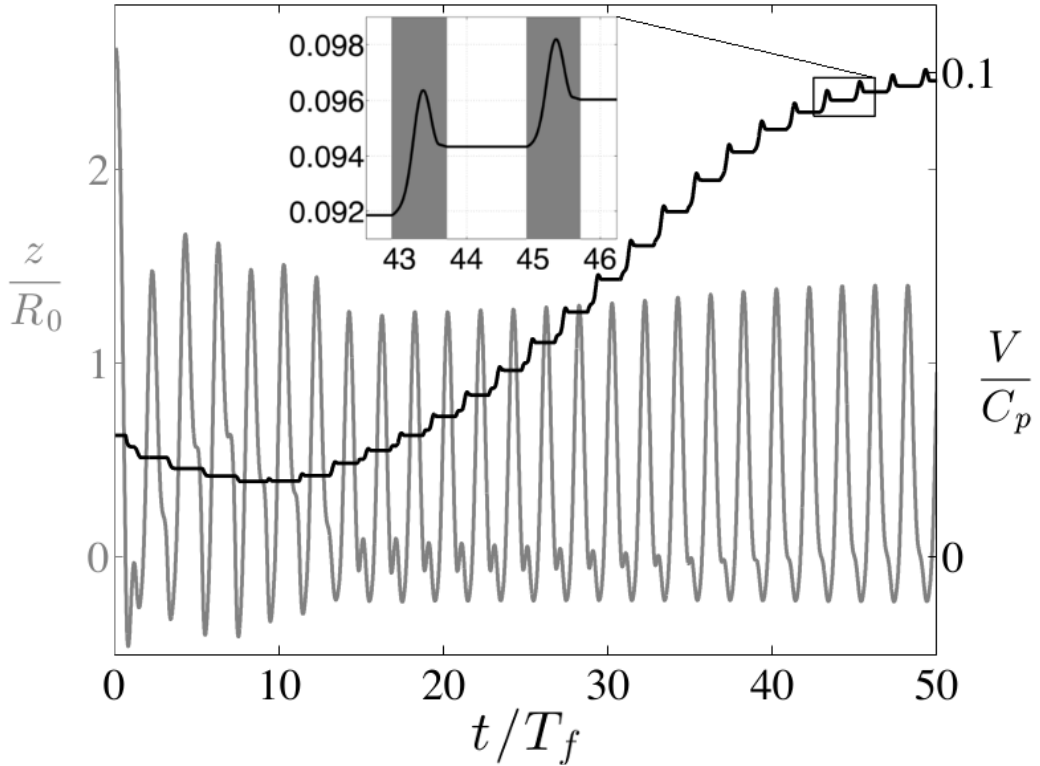


Figure 3.5: Transient of a walker ($\Omega = 0.8$, $\Gamma = 3.7$). Vertical trajectory of a walker (gray), in the laboratory frame of reference; together with its instantaneous horizontal velocity (black). The spikes shows the changes in velocity during contact (shaded regions). C_p is the phase velocity of the Faraday waves.

We initialized a walker with different velocities to check the robustness of the correspondence of the reported steady bouncing modes in Figure 3.3. The tests we performed indicate that different initial velocities do not affect the final steady regime. Figure 3.6 shows horizontal velocity as a function of time for the exact same configurations, except for their initial horizontal velocities. Notice that not only the final velocity is robust, but also the phase of impact coincides for all four cases. This walker is in a $(2, 1)^2$ mode, so it was in principle possible for any one of the resulting walkers to be one cycle out of phase, even if it were bouncing with otherwise identical motion.

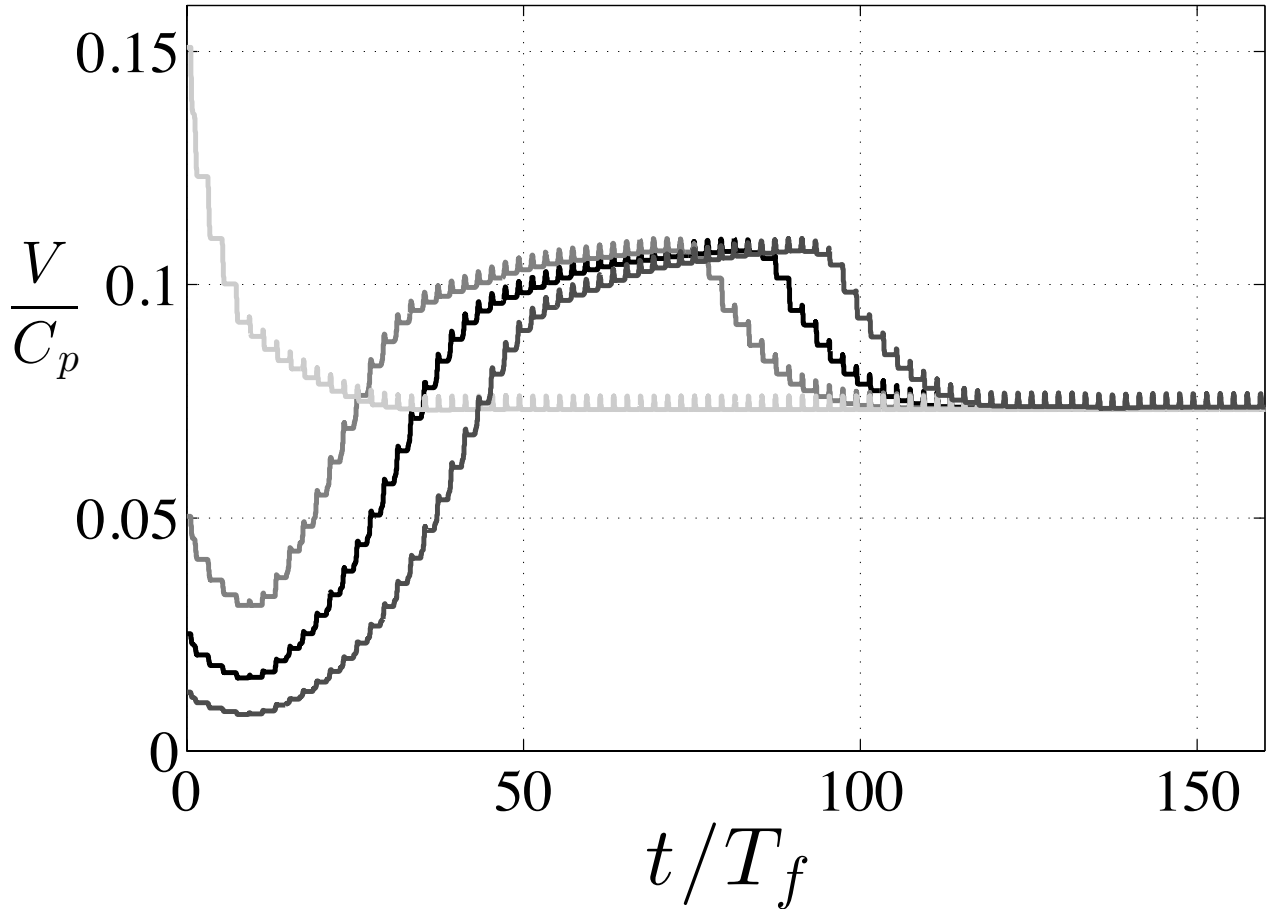


Figure 3.6: Evolution of the velocity of a walker ($\Omega = 0.8$, $\Gamma = 3.7$) with different initial velocities.

Though the system is robust in relation to initial velocities, we found cases in which Γ was changed after the drop had reached a steady state to a value that corresponded to a different mode, but the drop would remain in its initial mode. This multiplicity of states that can be obtained by changing Γ needs further study to be completely characterized.

3.3.2 Accuracy of Predicted Vertical Motion

Our model provides predictions for the vertical motion and contact times of both, bouncers and walkers. We were able to compare these with the most accurate experimental results currently available [14].

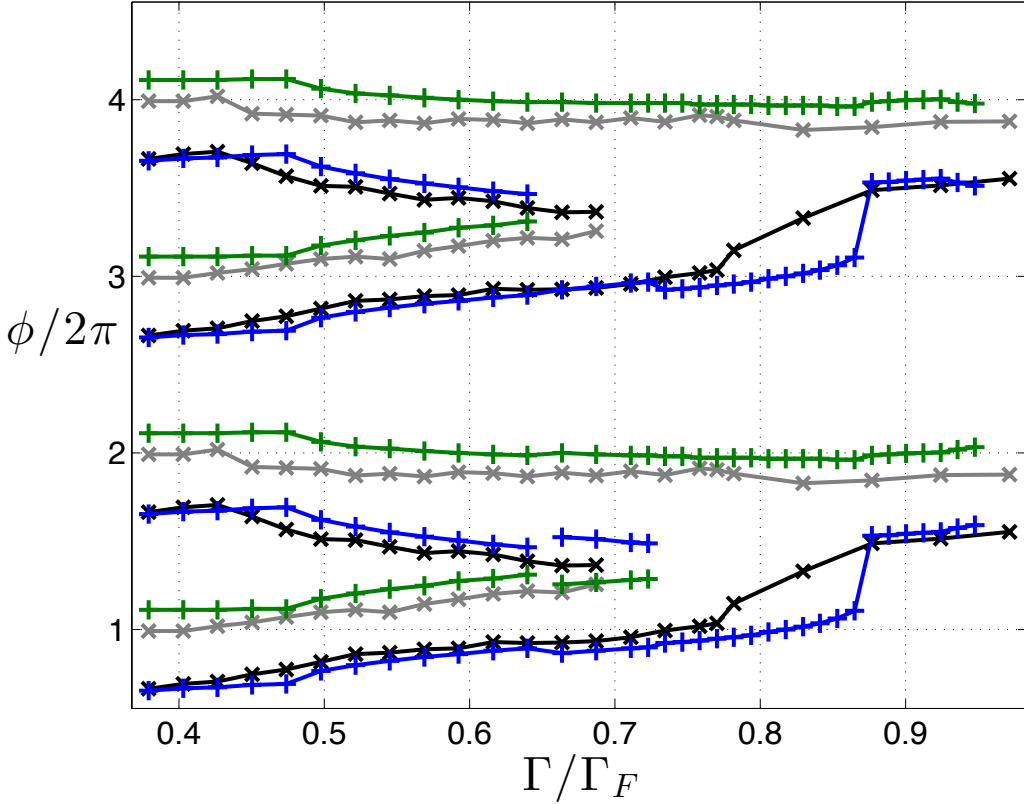


Figure 3.7: Impact phases for $\Omega = 0.8$. Every vertical traverse describes a bouncing or a walking state, with time (i.e. shaking phase) increasing upwards. For the experiment, contact starts when a black curve is reached and continues until the phase reaches a gray curve. At that point, the drop detaches from the bath and flies until the next black curve is encountered. Similarly, in the simulations, the blue curves correspond to impacts and contact lasts until the next green curve is met. Bullets show the actual data points, the line is simply the linear interpolant between two consecutive values.

Figure 3.7 shows a comparison between phases of impact as predicted by this model and as observed in the laboratory for different values of Γ [14]. Models presented here are the first to show evidence of correctly capturing the impact phases. The agreement in Figure 3.7 indicates that the predictions of our model coincide well with experimental measurements. Notice that our estimate of the duration of contact is somewhat larger than the reported values; this shortcoming may be due to the definition of contact that we use, which considers that the contact is over only when the hypothetical surface is below the drop once again, when in fact the forces between the drop and the fluid may have ceased earlier.

Careful examination of the phase transitions that take place as Γ increases in Figure 3.7 reveal the phase signature of the period doubling events attained as Γ changes. In particular,

between $\Gamma/\Gamma_F = 0.65$ and $\Gamma/\Gamma_F = 0.75$, it can be seen that our simulation report a (4, 3) mode, which is not reported experimentally for this drop size.

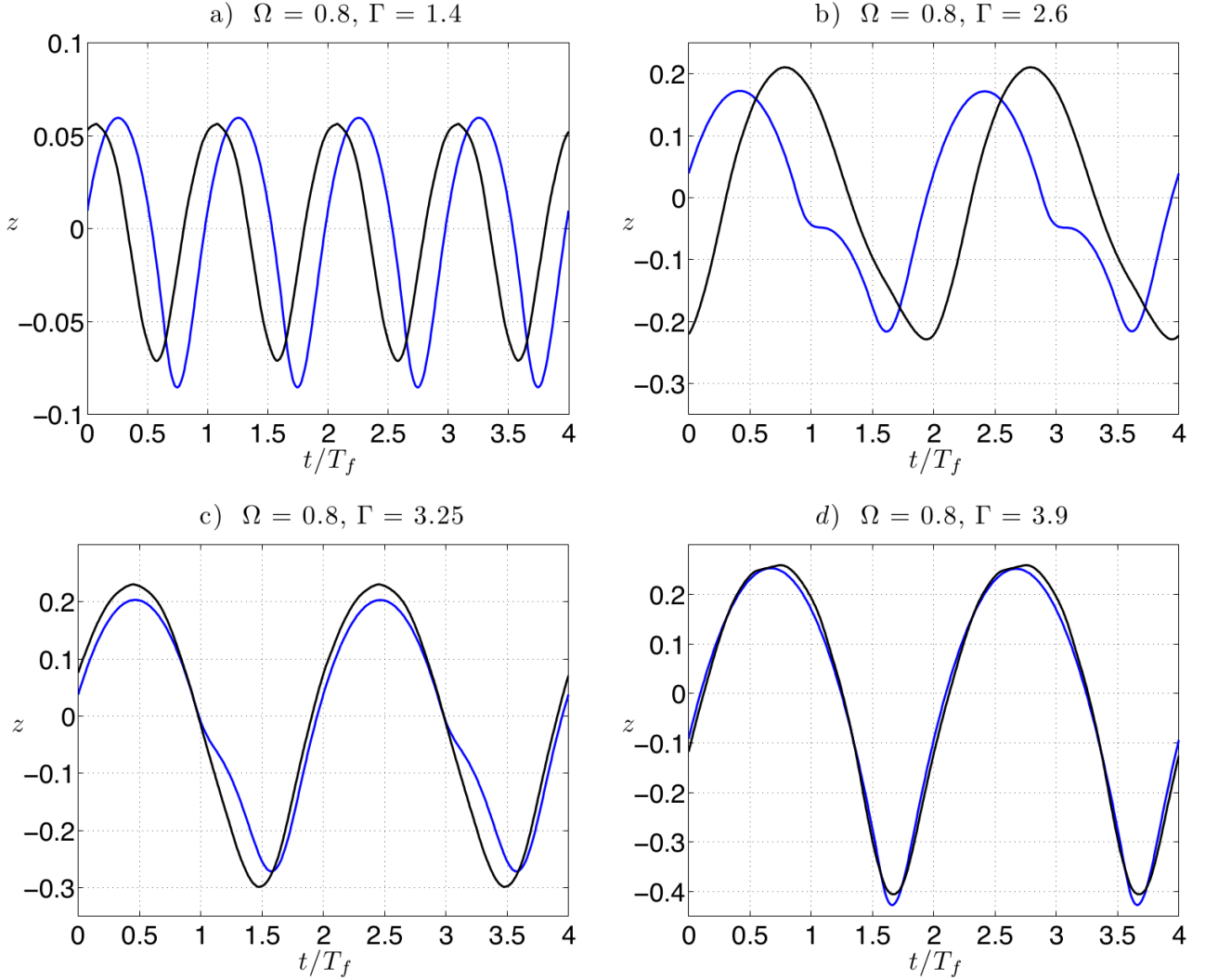


Figure 3.8: Vertical trajectories for $\Omega = 0.8$. Experimental measurements (black), compared to the predictions of our model (blue). Vertical axes are in mm .

Figure 3.8 shows the comparison between the predicted vertical trajectories of the droplets (blue), and the laboratory measurements. The data displayed suggest that agreement improves as we approach the Faraday threshold. This might be due to the fact that we have tuned the viscosity (ν^*) so as to match the dissipation at $\Gamma = \Gamma_F$, and thus the model might capture dissipation in the system less accurately for lower values of Γ .

3.3.3 Wave Fields

The model captures the characteristic wave field features of free space bouncers and walkers. Figure 3.9 shows the typical progression of the wave field of a bouncing droplet as Γ approaches Γ_F . In particular, at $\Gamma/\Gamma_F = 0.73$ the droplet is bouncing at a fixed position, and as Γ increases one can see how the symmetry in the direction of motion disappears progressively. This figure compares qualitatively to the photos of experiments presented in Figure 2 of [23].

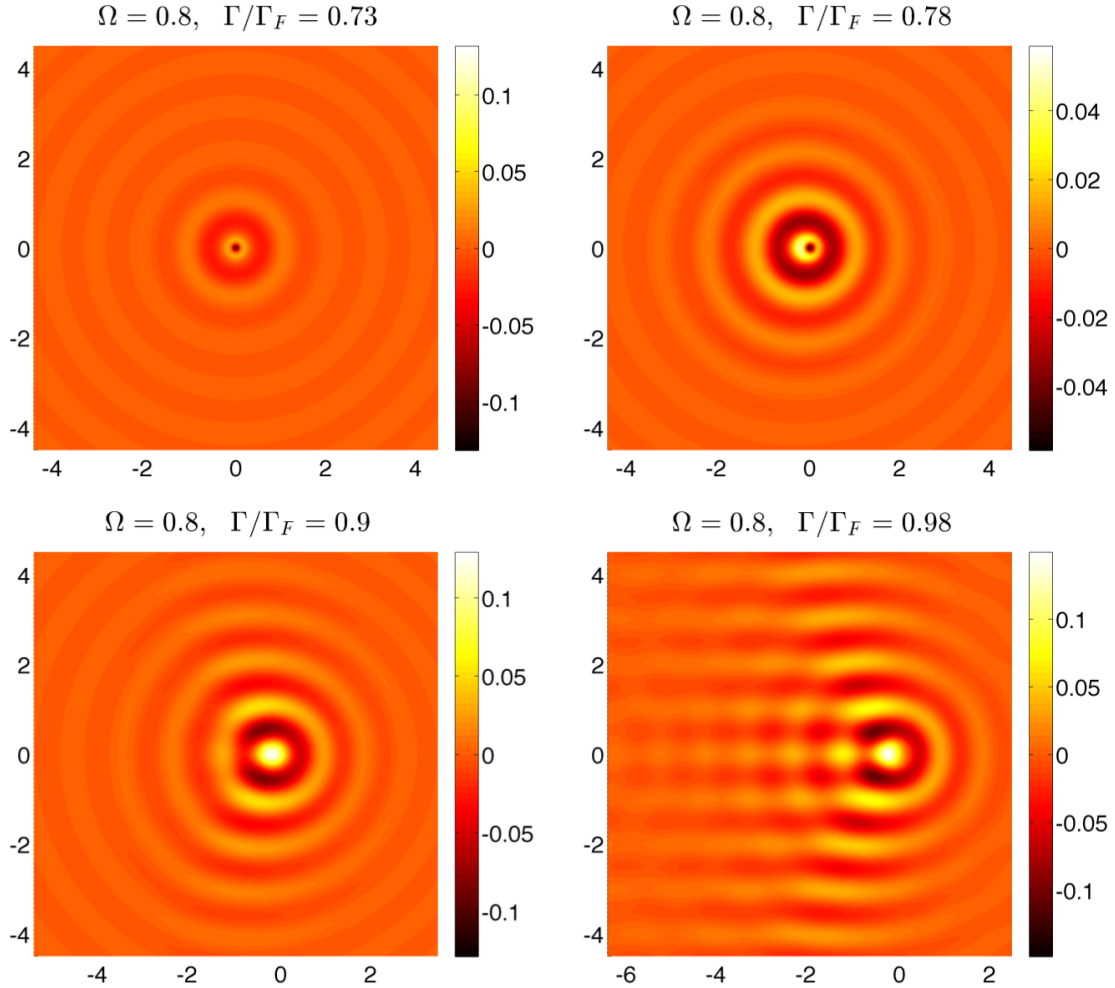


Figure 3.9: Wave fields for $\Omega = 0.8$. Axes are in units of λ_F , color scale is in units of z/R_0 .

We were also able to compare wave field predictions of our model to experimental measurements [14] obtained by the surface *Schlieren* method [39]. The results of the comparisons of that data to our model are presented in Figure 3.10. It is important to note that the Faraday threshold changes slightly from experiment to experiment, and so does the walking threshold. We chose to compare the bouncer with $\Omega = 0.8$ that is closest to walking. This corresponds to the case $\Gamma = 3.25$ in the experiments; and $\Gamma = 3.15$ in our simulations, which were calibrated to match the walking threshold reported on [53]. Notice that Figure 3.10 is missing data in the vicinity of the origin, the drop's shadow region. We thus only compare the waves beyond 3 mm from the center.

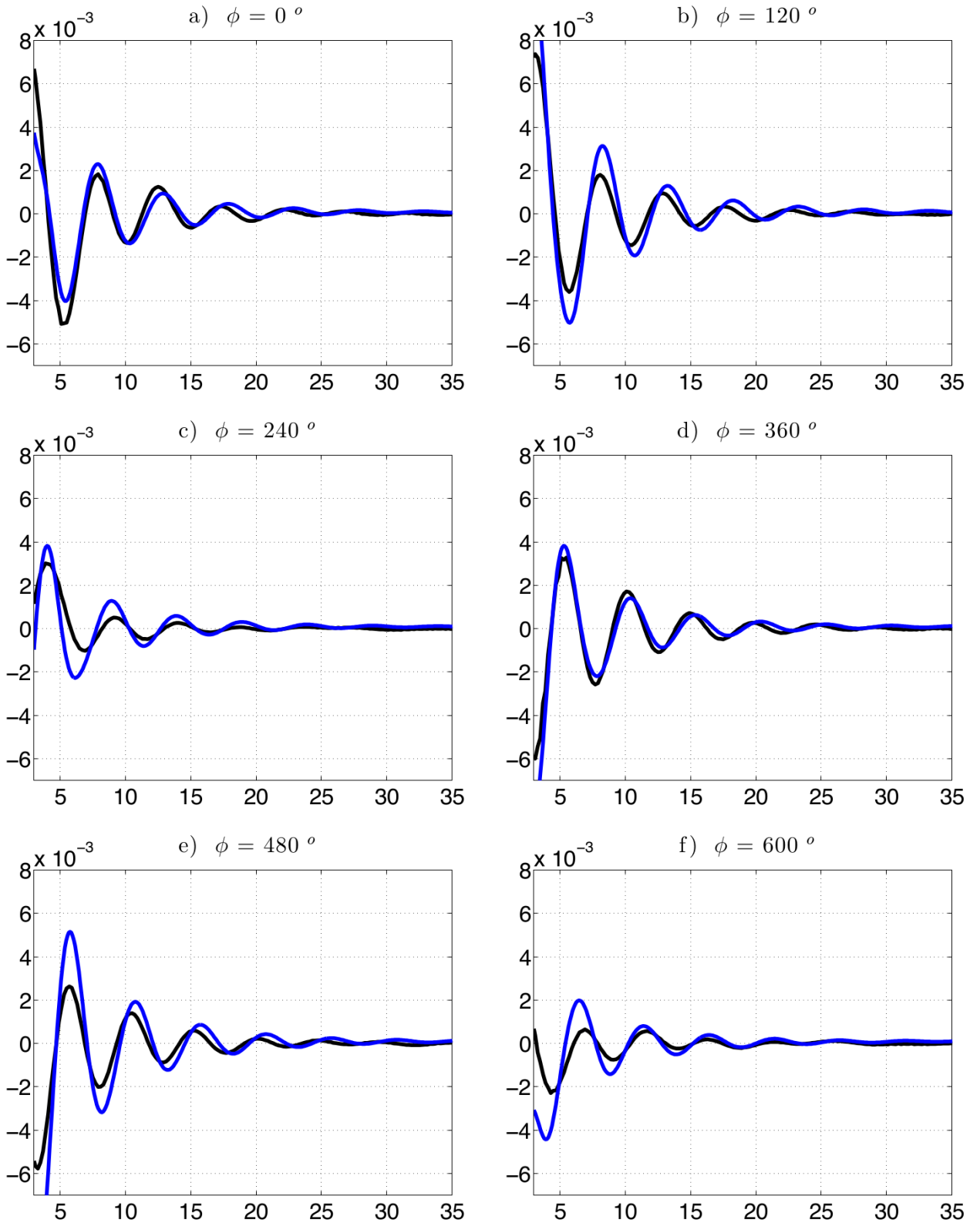


Figure 3.10: Axisymmetric wave field of a bouncer at different phases of the shaking, as measured with the *schlieren* method [14] (black) and as predicted by our simulations (blue). The vicinity of the origin is not shown, since in this region, the presence of the drop interferes with the experimental measurements.

Doppler Effect

Another interesting feature of walkers, reported in [23] is the Doppler effect that can be measured along the direction of motion. The drop acts as a moving source of waves, and a corresponding Doppler effect is observed, i.e. the wavelength as estimated by the mean distance between peaks ahead of the walker is shorter than that measured behind the walker.

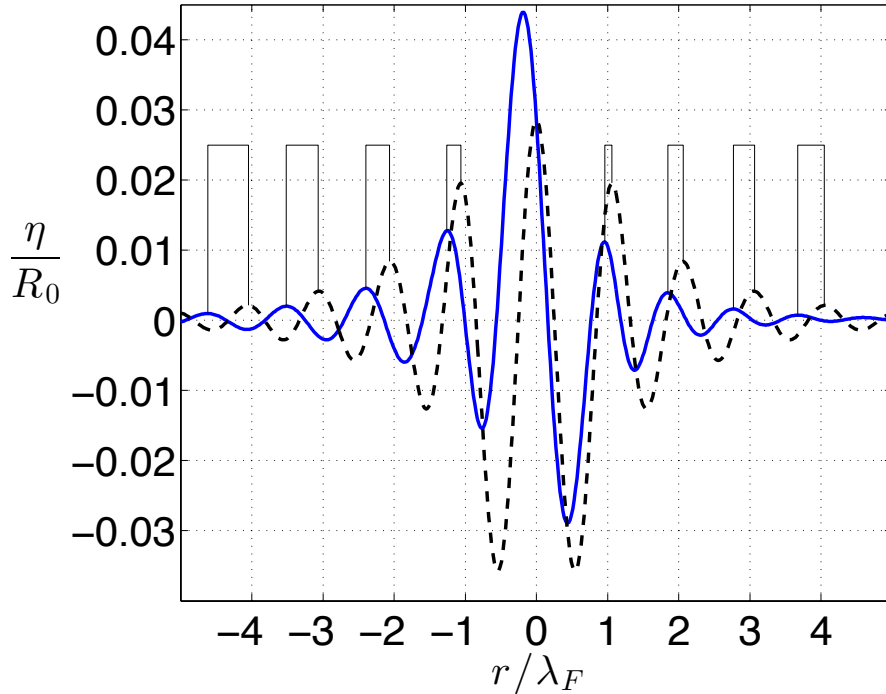


Figure 3.11: Cross sections of the wave field of a walker of $\Omega = 0.8$ and $\Gamma = 3.6$ right before an impact. A section along the direction of motion is shown in the solid blue line, a cut that is perpendicular to the direction of motion in the dashed black curve. The droplet's center is right above the origin, and both planes of section contain the vertical axis. The thin black lines indicate the difference between the peaks of the symmetric transverse section. The longitudinal section is affected by the Doppler effect.

Figure 3.11 presents a typical example of the Doppler effect seen in a walker. In this figure we take two vertical planes, one of which contains the direction of motion, and generates the blue curve when it intersects the wave field. The second plane contains the horizontal direction perpendicular to the direction of motion; this plane generates the dashed black line when it intersects the interface. The latter intersection is symmetric with respect to the origin, while the former is affected by the Doppler effect. Both planes contain the vertical that passes through the origin; on which the drop's center is found. Peaks to the right of the origin (direction of motion) fall increasingly closer to the origin, when compared to the transverse peaks. Peaks to the left of the origin fall ever farther from the origin, when compared with the same reference.

Thus, the two curves shown in Figure 3.11 are actually in two perpendicular planes. We expect no Doppler effect signature un the section that is transversal to the motion, i.e., the section should be symmetric. The thin black lines are used to indicate that the distance between

corresponding peaks increases in roughly the same amount successively. This corresponds to the accumulation of the differences between wavelengths.

Figure 3.12 summarizes the prediction for the Doppler effect obtained for walkers with walker of $\Omega = 0.8$. Figure 3.12 should be compared to figure number 14 in [23], which presents measurements of this effect as seen in the laboratory.

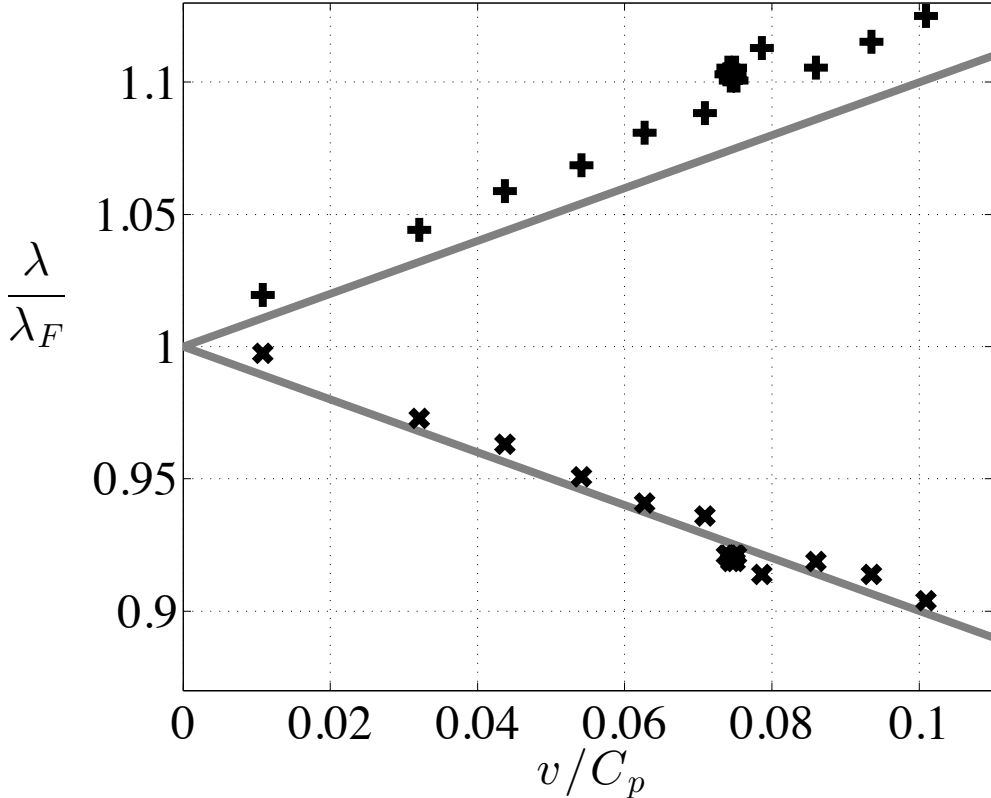


Figure 3.12: Wavelengths as measured from distances between peaks ahead of the walker (\times), and behind the walker (+); compared to the expected Doppler effect (gray) from a source of Faraday waves moving at the mean speed of the walker.

3.4 Multiple Droplets

Some of the most interesting phenomena observed with bouncing droplets appear when two of them interact by means of their accompanying wave fields. To facilitate the capture of the interactions between two bouncing droplets, we resorted to the use of one hypothetical surface for each drop. The hypothetical surface that corresponds to any given one of the drops, is calculated by removing the pressure due to an ongoing contact of the drop in question, but maintaining the pressure due to the ongoing contact of the other drop, whenever they are contacting the bath simultaneously. Using this strategy, we were able to observe the spontaneous appearance of behaviors that have been reported from laboratory experiments [12, 47].

Notice that when the walkers bounce in synchrony with the subharmonic waves; even when they have the same mode of bouncing, as can be expected from two identical drops in the same

parameter regime, the phase of impact may differ by a full forcing period. We were able to control whether the pair was bouncing in phase or out of phase simply by letting one drop initiate its motion one forcing period after the other or at the same time as the other one.

We had to increase the friction coefficient c_4 to 0.3, and to 0.32 in some cases, in order to capture some behaviors that are observed for similar experimental set ups and initial conditions. The agreement so far is mainly qualitative but still it shows that the ingredients that are necessary for this phenomena are present in a model of this kind.

3.4.1 Scattering and Orbiting

We simulate the launching of two identical walkers with initial antiparallel velocities, varying the distance between the incident trajectory lines, i.e. impact parameter (I_p) [48], for different values of Γ . We tested launching the walkers with impact parameters corresponding to integer multiples of $\lambda_F/2$.

We observe one of two alternatives, either the drops depart in different but still antiparallel directions (scattering collision) or they start to orbit each other (attracting collision). The second situation can in turn be realized in a perfectly circular orbit, or some wobbling motion may appear.

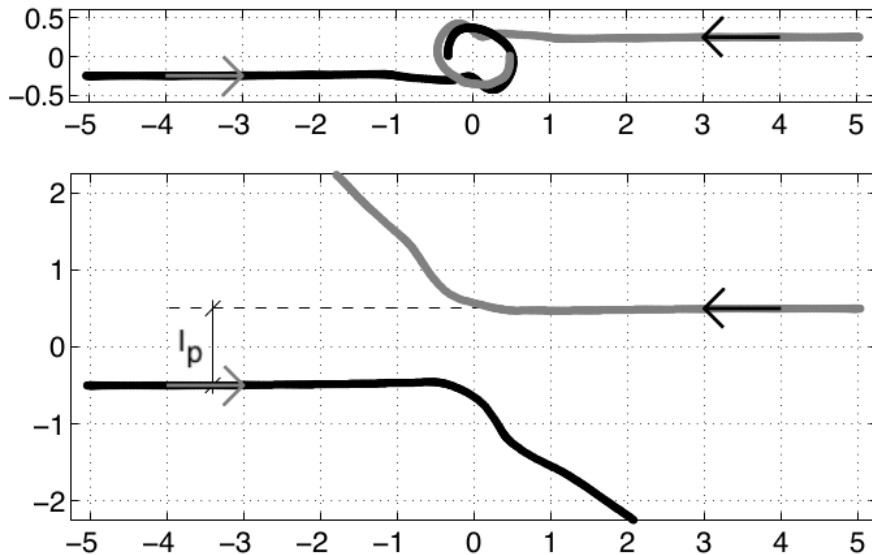


Figure 3.13: Walker collisions. Two identical droplets shot towards each other, with impact parameter equal to $0.5 \lambda_F$ (top), and λ_F (bottom), respectively. The former results in an attracting collision, the latter in a scattering event. Axes are in units of λ_F .

A more careful exploration of the parameter regimes where orbiting solutions exists, and how the system can be initialized to access them remains to be done. It is reasonable to suppose, for example, that a finer comb of the impact parameter may be needed; since, even if the orbital radii that can be accessed might not change, there is no a priori reason to assume that the launching distance has to be the same as the final orbital radius.

Figure 3.13 shows the paths of pairs of walkers in both kinds of collisions. It is important to highlight that the two experiments portrayed in it differ only in the impact parameter, and yet completely different responses are obtained. Orbiting pairs have been reported to exist only for certain discrete radii [47], and for this reason we looked for them only with the initial separation corresponding approximately to those values of orbiting diameter.

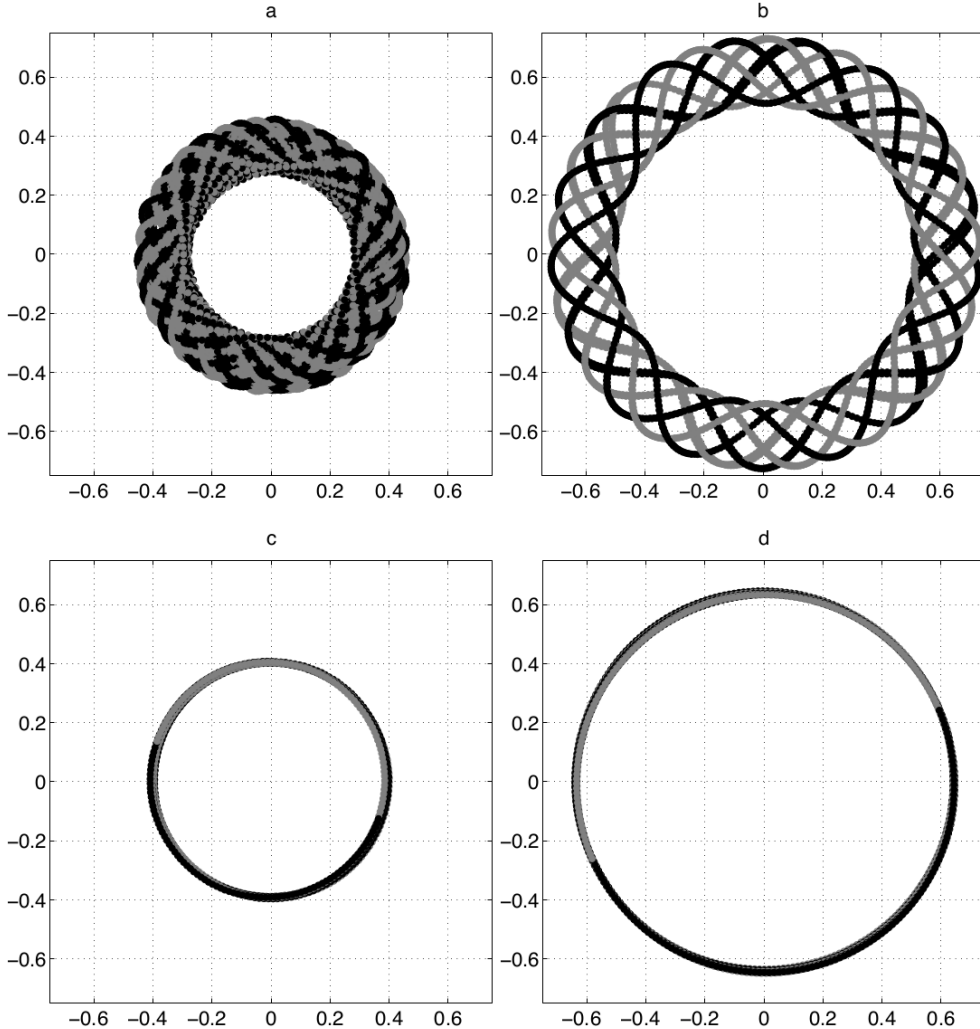


Figure 3.14: Trajectories of orbiting pairs. a) $\Omega = 0.8$, $\Gamma = 3.7$, $c_4 = 0.32$, walkers in phase; b) $\Omega = 0.8$, $\Gamma = 3.6$, $c_4 = 0.32$, walkers out of phase; c) $\Omega = 0.7$, $\Gamma = 4$, $c_4 = 0.3$, walkers in phase; d) $\Omega = 0.7$, $\Gamma = 4$, $c_4 = 0.3$, walkers out of phase.

The simulations performed so far show evidence that the predicted wobbling motion can be commensurate with the original orbit or not, thus giving rise to periodic or quasi-periodic wobbling orbital solutions. Figure 3.14 shows the different orbiting modes obtained with walkers bouncing in phase and out of phase. Only the steady state is presented, but all orbiting pairs were generated by collisions like those shown in Figure 3.13.

Figure 3.15 shows the wave field of a pair of non-wobbling orbiters, in phase and out of phase. Both cases correspond to a counter clockwise rotation.

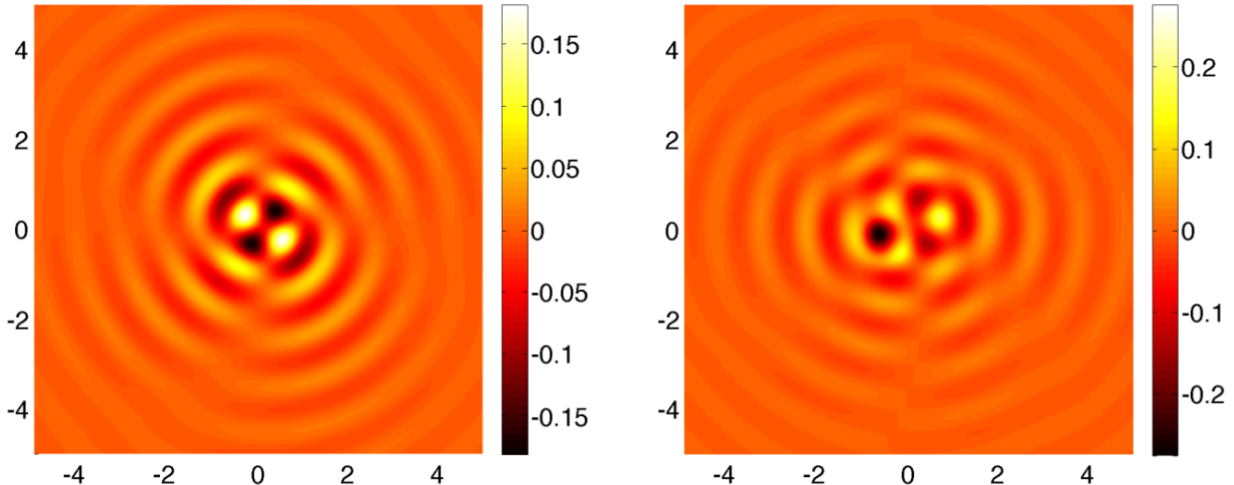


Figure 3.15: Wave fields of non-wobbling orbiting pairs, bouncing in phase (left) and out of phase (right).

3.4.2 The Promenade Mode

Another phenomenon that is observed experimentally when working with two identical droplets occurs when they move side by side along the same direction with added transversal oscillation. This has been named the promenade mode [4]. As it turns out this model captures this behavior in a completely spontaneous way. We simply launch the two walkers with initially parallel velocities and they instantly initiate a transversal wobbling motion that after a few oscillations reaches a periodic regime. We are also able to obtain promenading pairs with bouncers out of phase, and once again we see evidence of the existence of preferred distances at which the motion can take place.

Figure 3.16 shows some of the promenading orbits obtained with bouncers in phase and out of phase. In it, horizontal trajectories are shown color coded by the mean value of the horizontal speed of the droplet through one period of its vertical motion.

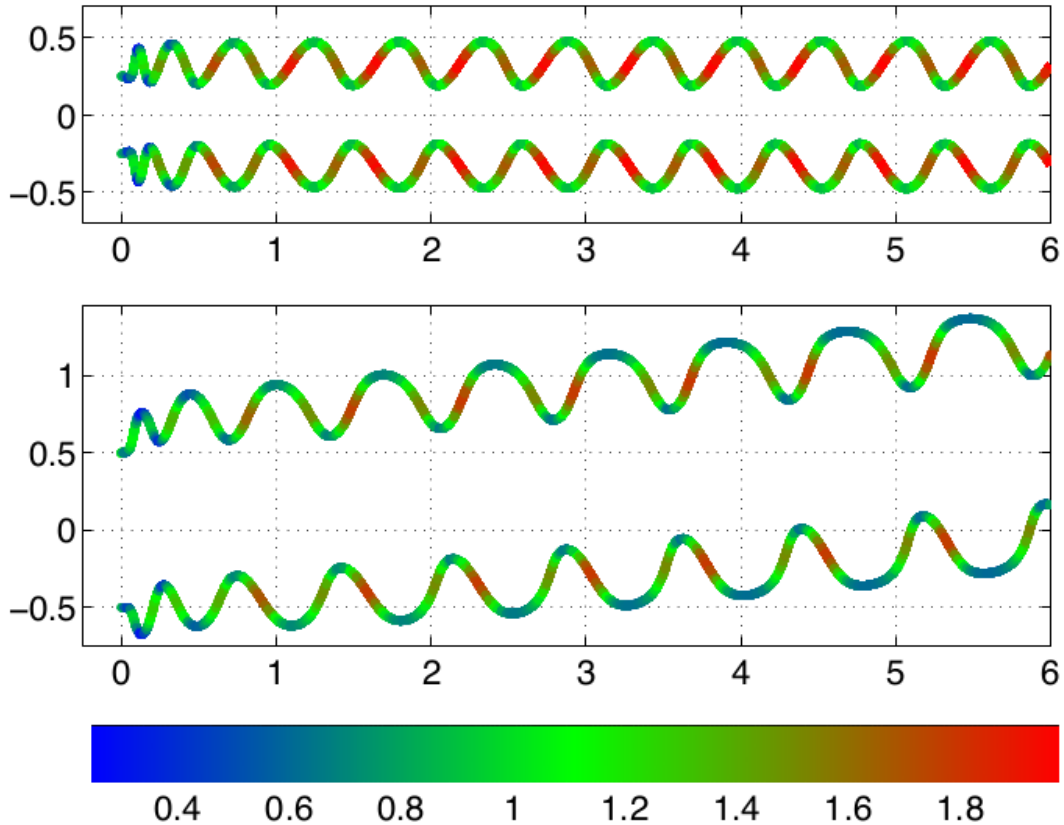


Figure 3.16: Trajectories of promenading pairs, bouncing in phase (above) and out of phase (below). Trajectories are color coded by mean velocity during a period of vertical motion. Axes are in units of λ_F and the color scale indicates mean horizontal speed of walkers through a period of its vertical motion, in units of phase velocity opt the waves (v/C_p). Note the dramatic changes in speed.

3.5 Possible Improvements

The next two chapters present, respectively; an alternative modeling of the surface-droplet interaction, which does not require the use of any coefficients deduced from experiments, and a more careful modeling of dissipation. Both developments show evidence of their potential to improve the predictive nature of our model.

This page was intentionally left blank.

CHAPTER 4

A Kinematic Matching Condition

We present a model for a bouncing droplet, based on the fluid model presented in Chapter 2, and the imposition of geometric constraints of motion.

4.1 The Modeling Assumptions

We wish to obtain a model that produces consistent displacements of the bath surface and the drop. More specifically, we wish to enforce impenetrability of both masses of fluid. This is a very natural constraint for the problem; since we know that if the two ever come into contact, the drop will initiate a coalescence cascade [11, 35, 40]. We are also aware that the pressure interaction between droplet and bath is made possible by the sustenance of a very thin air layer between the two [11]. Thus, where we have pressure acting between droplet and bath, we expect the two surfaces to be extremely close to each other. A modeling choice is thus made. We must have that the surface elevation $\eta(x, y)$ is no greater than the lowest point of the drop for each value of (x, y) .

At the same time, considering that the air layer is very thin, when compared to the drop's radius, we will assume that the surface of the bath and that of the drop actually coincide along the area throughout which pressure is applied. Naturally, since we are dealing with a lubrication layer, we will assume that pressures do not change across the width of the air layer; and thus we impose the same pressure field on both fluid masses as follows from Newton's third law.

The dynamics of small bouncing droplets is less likely to rely on droplet deformation [50]. We will henceforth assume that the drop is a perfectly rigid sphere, and explore the range of validity of this approximation. We naturally expect to obtain better results for smaller drops.

Finally, when the drop is in contact throughout a given subset of the sphere S_C , we will assume that the surface of the liquid is tangent to that of the drop at the boundary of S_C (∂S_C).

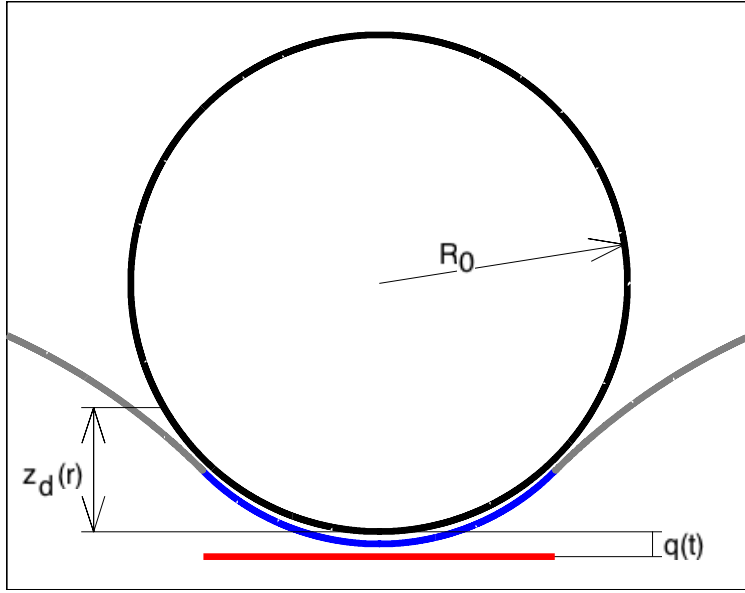


Figure 4.1: Outline of the geometric assumptions. The cross section of the surfaces of the drop (black) and the bath shows how the contacted spherical section S_C (blue) of the free surface and its derivative match onto the rest of the interface (light gray) at their meeting point. Below (red), we see the cross section of A_C , the horizontal projection of S_C on to the $z = 0$ plane.

This assumption is nothing but the requirement that there be no curvature singularity at the matching point of these two surfaces. A curvature singularity would imply a pressure singularity due to surface tension, and hence it is unphysical. Figure 4.1 outlines this configuration.

The considerations above, put together with the slowly decaying waves model presented in Chapter 2 yield the following system

$$\eta_t = 2\nu^* \Delta_H \eta + N\phi, \quad (4.1a)$$

$$\phi_t = -g(t)\eta + \frac{\sigma}{\rho} \Delta_H \eta - 2\nu^* \Delta_H \phi - \frac{p_d}{\rho} + \frac{\sigma}{\rho} (\kappa - \Delta_H) \eta, \quad (4.1b)$$

$$q_{tt} = -\frac{c_{St}}{m} q_t - g(t) + \frac{1}{m} \int_{A_C} p_d \, dx dy, \quad (4.1c)$$

subject to

$$\eta(\vec{r}, t) \leq q(t) + z_d(r); \quad (4.2)$$

where

$$z_d = \begin{cases} R_0 - \sqrt{R_0^2 - r^2} & \text{for } r \leq R_0, \\ +\infty & \text{for } r > R_0, \end{cases} \quad (4.3)$$

with ν^* as defined in equation (2.42), m is the mass of the drop, and $c_{St} = 6\pi R_0 \mu_{air}$ is the coefficient for Stoke's drag. $q(t)$ is the height of the lowest point of the drop (under the center), $z_d(r)$ is given by the lower half of the spherical drop (see Figure 4.1). A_C is the horizontal projection of the contacted fraction of the sphere S_C , i.e. the maximal possible support of

function p_d , R_0 is the drop's radius, $\vec{r} = (x, y)$ and $r = |\vec{r}| = \sqrt{x^2 + y^2}$. The origin of the coordinate system shares a vertical with the center of the drop and is placed at the level of the unperturbed surface.

In system (4.1), we have recovered the form in physical space of the multiplication operators in Fourier space to which we arrived in Chapter 2. Also, we have kept the full non-linear expression of curvature, but separated it into its linear and non-linear parts. The motivation to keep the full curvature is that beneath the drop, the surface shape will approach that of a sphere, thus having an important curvature, that the linear approximation might estimate poorly. We have the exact value for the non-linear curvature along the support area A_C , it is specifically the difference between the curvature of the sphere and the horizontal Laplacian of the same sphere. Away from the drop, outside A_C , the pressure jump should be small, so we can safely use the linear approximation.

To summarize, we model the drop as a perfectly hydrophobic solid sphere, and its effect on the fluid by the pressure field that is needed for compatible motion of the interfaces. This, as will be shown, produces a parameter free model of the surface-droplet interaction of a bouncer.

4.2 An Implicit Iterative Method in Physical Space

According to our model, the contacted part of the fluid surface will be a section of a sphere. In particular, notice that once a contact area is chosen, the displacement of that section of the fluid surface is fully determined up to a vertical translation. Hence this problem inherently induces a decomposition of the free surface into two parts. The position of the spherical section is determined up to a translation, and the rest of the surface is dictated by system (4.1).

It is very natural to use the spatial Fourier transform to solve the differential operators involved, since they have a diagonal representation in Fourier space. It may be possible to solve this problems in Fourier space, but some technical difficulties have to be overcome first. For now, we start by using methods based on the form of these operators in physical space.

Consider now the problem of a drop in flight whose position, after a given interval of time, we wish to determine. Notice that the drop may impact the surface during this time. This means that, at the initial time, we do not yet know whether or not there will be pressure forces affecting the drop's trajectory. These pressures will, of course, also affect the motion of the fluid. Thus, if we wish to produce a model with no inconsistencies in the position of the two masses of fluid, the calculations must be coupled, making the need for an implicit method intrinsic to the problem.

Also, whenever a contact arises, we need to specify at least two variables, the contact area A_C and the height of the spherical part. Determining the contacted part of the sphere and its position will determine the region where the pressure has to be such that it forces the fluid to follow a sphere. Moreover, the normal derivative at the curve that bounds S_C has to be that of S_C . With these conditions, we could expect that the surface elevation of the rest of the

fluid should be determined by the differential relations presented in system (4.1). This suggests that we can define a contact A_C , and the values of pressure and surface elevation will be fully determined by the relations we enforce. Nevertheless, we may still need to test different possible contact areas, and choose the solution that produces the most physical result. We will show the realization of this approach in the following sections.

4.3 A Problem of Singular Integrals

As mentioned above, the N transform has a diagonal representation in Fourier space, which we unfortunately can not use at the time. We must then investigate the form of this transform in physical space. We consider the problem in the half-space $D = \{(x, y, z) ; z < 0\}$. We assume that we are only looking for solutions as smooth and decaying as necessary to guarantee all the convergences that we need. We will also assume that the differential relations hold even on the boundary. As it turns out, under these conditions, we have

$$N\phi(\vec{r}) = \frac{1}{2\pi} \lim_{\epsilon \rightarrow 0^+} \int_{\mathbb{R}^2 \setminus B(\vec{r}; \epsilon)} \frac{\phi(\vec{r}) - \phi(\vec{s})}{|\vec{r} - \vec{s}|^3} dS(\vec{s}), \quad (4.4)$$

where $\vec{s} = (x', y')$, and

$$B(\vec{r}; \epsilon) = \{\vec{s} = (x', y') ; |\vec{r} - \vec{s}| < \epsilon\}. \quad (4.5)$$

The form of the N transform evidently involves the computation of a singular integral. As is well known, singular integrals rely strongly on cancellations due to symmetries of the integral kernels. It will thus be very important to use an appropriate mesh to compute them. Specifically, we must make sure that the mesh has point symmetry around the singularity of the kernel. A proof of equality (4.4) and of the existence of this limit, for sufficiently smooth and decaying functions ϕ , is given in Appendix D.

4.4 Simulating a Bouncer

We explore the case of a bouncer configuration, which has the advantage of being axisymmetric. Our problem was already reduced to the surface, hence when axisymmetric it becomes effectively 1D.

We assume that the contact area is simply connected. In the axisymmetric case this simply means that the contacted part of the drop is a spherical cap. A_C is a circle, and we need only specify its radius to determine the contact area.

We use an implicit finite differences scheme in time, given by

$$\frac{\eta^{j+1} - \eta^j}{dt} = 2\nu^* \Delta_H \eta^{j+1} + N \phi^{j+1}, \quad (4.6a)$$

$$\frac{\phi^{j+1} - \phi^j}{dt} = g^{j+1} \eta^{j+1} + \frac{\sigma}{\rho} \Delta_H \eta^{j+1} + 2\nu^* \Delta_H \phi^{j+1} - \frac{p_d^{j+1}}{\rho} + \frac{\sigma}{\rho} (\kappa - \Delta_H) \eta^{j+1}, \quad (4.6b)$$

$$\frac{\dot{q}^{j+1} - \dot{q}^j}{dt} = -\frac{c_{St}}{m} \dot{q}^{j+1} + g^{j+1} + \frac{1}{m} \int_{A_C} p_d^{j+1} dx dy, \quad (4.6c)$$

$$\frac{q^{j+1} - q^j}{dt} = \dot{q}^{j+1}; \quad (4.6d)$$

subject to

$$\eta^{j+1} \leq q^{j+1} + z_d. \quad (4.7)$$

System (4.6) yields the following matrix relation

$$Q^{j+1} W^{j+1} = F^j; \quad (4.8)$$

where

$$Q^{j+1} = \begin{bmatrix} (I - 2dt \nu^* \Delta_H) & -dt N & 0 & 0 & 0 \\ -dt \left(g^{j+1} I + \frac{\sigma}{\rho} \Delta_H \right) & (I - 2dt \nu^* \Delta_H) & -dt \frac{I}{\rho} & 0 & 0 \\ 0 & 0 & -dt \frac{A}{m} & \left(1 + dt \frac{c_{St}}{m} \right) & 0 \\ 0 & 0 & 0 & dt & 1 \end{bmatrix}, \quad (4.9)$$

$$W^{j+1} = \begin{bmatrix} \eta^{j+1} & \phi^{j+1} & p_d^{j+1} & \dot{q}^{j+1} & q^{j+1} \end{bmatrix}^T, \quad (4.10)$$

$$F^j = \begin{bmatrix} \eta^j & \phi^j + dt \frac{\sigma}{\rho} (\kappa - \Delta_H) \eta^{j+1} & \dot{q}^j + dt g^{j+1} & q^j \end{bmatrix}^T. \quad (4.11)$$

Above, I is the identity operator, and A is the integral functional. When the spatial differential operators in (4.8) are discretized, we can see (4.8) as a relation between the vector variables defined on the mesh. Since we will be dealing with radial functions, we will use regular polar meshes. This means that our meshes will consist of evenly distributed radial lines and concentric circles. Recall that axial symmetry requires that we only solve one radial line of that mesh.

We must then find a finite difference approximation to the polar expression of Δ_H . Similarly, we need to find a numerical approximation to the integral on a polar mesh. To do this, we assume the wave has decayed sufficiently in the far field that we can neglect the contributions to the singular integral that come from points of the surface beyond $R = 5\lambda_F$.

We recall the polar expression for Δ_H

$$\Delta_H \phi(r, \theta) = \frac{\partial^2}{\partial r^2} \phi + \frac{1}{r} \frac{\partial}{\partial r} \phi + \frac{1}{r^2} \frac{\partial^2}{\partial \theta^2} \phi, \quad (4.12)$$

which for a radial ϕ yields

$$\Delta_H \phi(r) = \frac{\partial^2}{\partial r^2} \phi + \frac{1}{r} \frac{\partial}{\partial r} \phi. \quad (4.13)$$

Notice that equation (4.13) has a definition problem at the origin; specifically, it is not suited to base a finite difference scheme on it at that precise point. For this point we can use the equivalent of the 5-point stencil approximation to Δ_H in a radial set up, i.e.

$$\Delta_H \phi(0) \approx 4 \frac{\phi(dr) - \phi(0)}{dr^2}. \quad (4.14)$$

For every other point we use

$$\Delta_H \phi(l dr) \approx \frac{\phi((l+1) dr) - 2\phi(l dr) + \phi((l-1) dr)}{dr^2} + \frac{\phi((l+1) dr) - \phi((l-1) dr)}{2 l dr^2}. \quad (4.15)$$

The integral functional A is estimated by the linear interpolation in the radial direction, yielding a weighted sum of the coefficients in the mesh.

Estimating the N operator is a more complicated matter. First, it is not a local operator, and hence the value of ϕ_z at each point will depend on the value of ϕ at every point of the mesh. This essentially means that the matrix representation of its approximation will be full. Secondly, cancelations of the kernel weights are essential in a singular integral such as the one in (4.4); thus, to estimate $\phi_z(r, 0)$ we need to use a new, auxiliary, polar mesh (r', θ') centered at each point $(r, 0)$ of our original mesh. We make sure that this new mesh has an even number of radial lines and compute the singular integral one concentric circle at a time. Moreover, to compute the value of ϕ_z at each point of this mesh, we need to find the distance from each point of the new mesh to the origin. This distance will in general not be an integer multiple of dr , and thus we use a linear interpolation of the values at the two mesh points that are most similar in distance to the origin.

Another feature of the new mesh centered at each point $(r, 0)$ is that its size has to be

$$R_r = R_d + r, \quad (4.16)$$

where R_d is the radius of the region outside which we assume the wave has decayed to a negligible amplitude. This condition on the auxiliary meshes is imposed so that it can cover all the points of the disc centered at the origin and with radius R_d . We compute the contribution of different points of the new mesh, adding the coefficient for the contribution of each point being interpolated into a matrix, where every line corresponds to a point where ϕ_z is being found, and every column corresponds to the weight of the value of ϕ .

At this point, we have a discrete approximation to the operator Q^{j+1} , so we only need

an adequate estimate of the κ operator to complete our formulation of the discrete version of problem (4.8). Of course, we can always neglect the contribution of the non-linear part of curvature; but for the bouncer problem, specially for small drops, curvature might not be accurately estimated by the linear approximation. So, instead of linearizing curvature everywhere, we linearize it for the mesh points that are at the contact perimeter or beyond. At points interior to A_C , the surface curvature is very close to that of the drop; i.e $\kappa \approx 2/R_0$, and Δ_H is approximately the Laplacian of the lower half of a sphere of radius R_0 .

Recall also that the contacted points have their position determined up to a vertical translation by the shape of the solid sphere model. Thus, we can parameterize their position as $z + z_d(r)$. Thus, when we have contact at n_c mesh points; we can remove the n_c columns that correspond to the value of η at the contacted points from the first block column matrices of the matrix representation of operator Q^{j+1} . We will, in turn, have to add a column of coefficients of z in the fifth block column and a column of constants to the first and second vector elements of the matrix representation of F^j . These constants are due to the contribution of z_d in Δ_H .

Notice now that, when there is no contact, the third element of W^{j+1} , given in (4.10) vanishes, thus rendering useless the third column of Q^{j+1} as given in (4.9). This effectively decouples system (4.8) into two square systems. When there is contact at n_c points, the first n_c columns of the matrix representation of Q^{j+1} become irrelevant, and simultaneously the third block column of the matrix representation of Q^{j+1} has exactly n_c relevant columns. This now yields a square system for each possible value of n_c .

Finally, we can then proceed in the following way at each time step. We solve the system as if there will be no contact during the next time step. If this assumption leads to the droplet penetrating the fluid, we discard this solution, and proceed to try all possible number of contact points, from 1 to the integer part of R_0/dr ($\text{int}(R_0/dr)$). Each one of the possible contact areas will produce an error in the tangency of the drop to the free surface at the boundary of the contact area. We choose the contact length that minimizes the absolute value of this error. Put more succinctly we apply the following algorithm

1. *Do for $t < t_{final}$*
2. *Solve system (4.8) assuming there are no contact points. If the solution does not produce overlap of the fluid masses, update t and go to step 1. Otherwise go to step 2.*
3. *Solve system (4.8) for $n_c = 1, 2, \dots, \text{int}(R_0/dr)$. Select the solution corresponding to the minimum absolute tangency error at the matching point. Update t , go to step 0.*

A final remark is in order. The curvature on the perimeter of the contact area is not well defined, since it may have a discontinuity on this matching point. We approximate the value of curvature at this point assuming $\kappa \approx \Delta_H$.

4.4.1 Results

We use this model to simulate experiment with $\nu = 0.2 \text{ St}$, $\rho = 0.949 \text{ g/cm}^3$, $\sigma = 20.6 \text{ dyne/cm}$ and $\omega_0 = 2\pi \cdot 80 \text{ rad/s}$. We take $\nu^* = 0.8025 * \nu$, as defined in section 2.4.1. We initialize the problem with the bath at the maximum height of its simple harmonic motion; the drop falling towards the bath with $\dot{z} = -8.422 \text{ cm/s}$, chosen to be comparable to a free fall from a height similar to the vertical amplitude of a typical droplet motion. We also initialize the drop at a height of $.01154 \text{ mm}$, chosen to initiate contact in few time steps. All of these conditions were chosen aiming at reduce the time that it would take to reach the steady regime.

We use a polar spatial mesh that guarantees that $dr < R_0/10$. The angular spacing here is irrelevant to the problem, since our domain is reduced to a line. For the mesh required to approximate $N\phi$ we use the same radial spacing and an angular spacing of $d\theta = 2\pi/n_\theta$, where n_θ is the closest integer to $1/dr$. This is chosen so as to minimize numerical error when integrating.

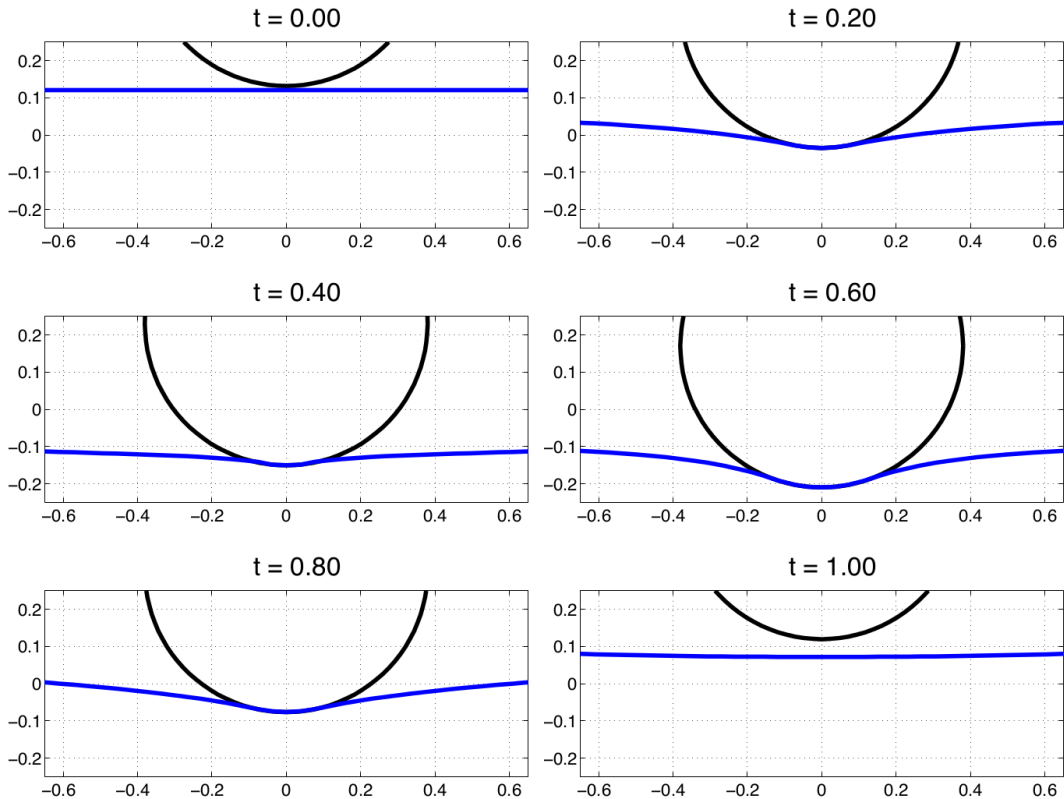


Figure 4.2: Cross section of the bouncer's first impact ($\Gamma = 3.1$, $\Omega = 0.8$). Time is measured in units of forcing periods, space in mm .

We run the simulations for 3 seconds and record the first 10 and the last 17 forcing periods of surface motion. We also record the entire vertical trajectory of the drop. The drop selects very quickly its bouncing mode but achieving precise periodicity takes several bounces. Time step size is chosen so as to match 1 sexagesimal degree of the forcing phase. By varying the drop size, and the amplitude of the shaking Γ , we obtain an important variety of modes which reproduce many regimes reported in [53]. Figure 4.2 shows the result of a bouncer simulation

where the result of imposing the geometrical constraints that we just described is evident.

We follow [40, 41, 53] in defining the drop's vibration number as

$$\Omega = \omega_0 \sqrt{\rho R_0^3 / \sigma}, \quad (4.17)$$

the quotient between the driving frequency and the natural frequency of the drop. Notice that $\Omega(R_0)$ is a monotonically increasing map on R_0 , and thus Ω essentially acts as a proxy for drop size. We prefer Ω over R_0 to classify drops, since it has been reported that different set ups will produce a different $\Gamma/\Gamma_F - R_0$ graph, but these data collapse when we instead use the dimensionless $\Gamma/\Gamma_F - \Omega$ plane [41].

We follow the same mode notation as in [53], where they identify the bouncing mode in terms of the drop's vertical motion. This is done by assigning an ordered pair (m, n) to each bouncer. m indicates the length of the period of vertical motion of the drop, measured in forcing periods; n indicates how many times along that period the drop contacts the surface. For example, mode $(1, 1)$ is a mode that is synchronous with the forcing and sustains one contact interval per bouncing period. Figure 4.3 shows different bouncing modes obtained with $\Omega = 0.8$.

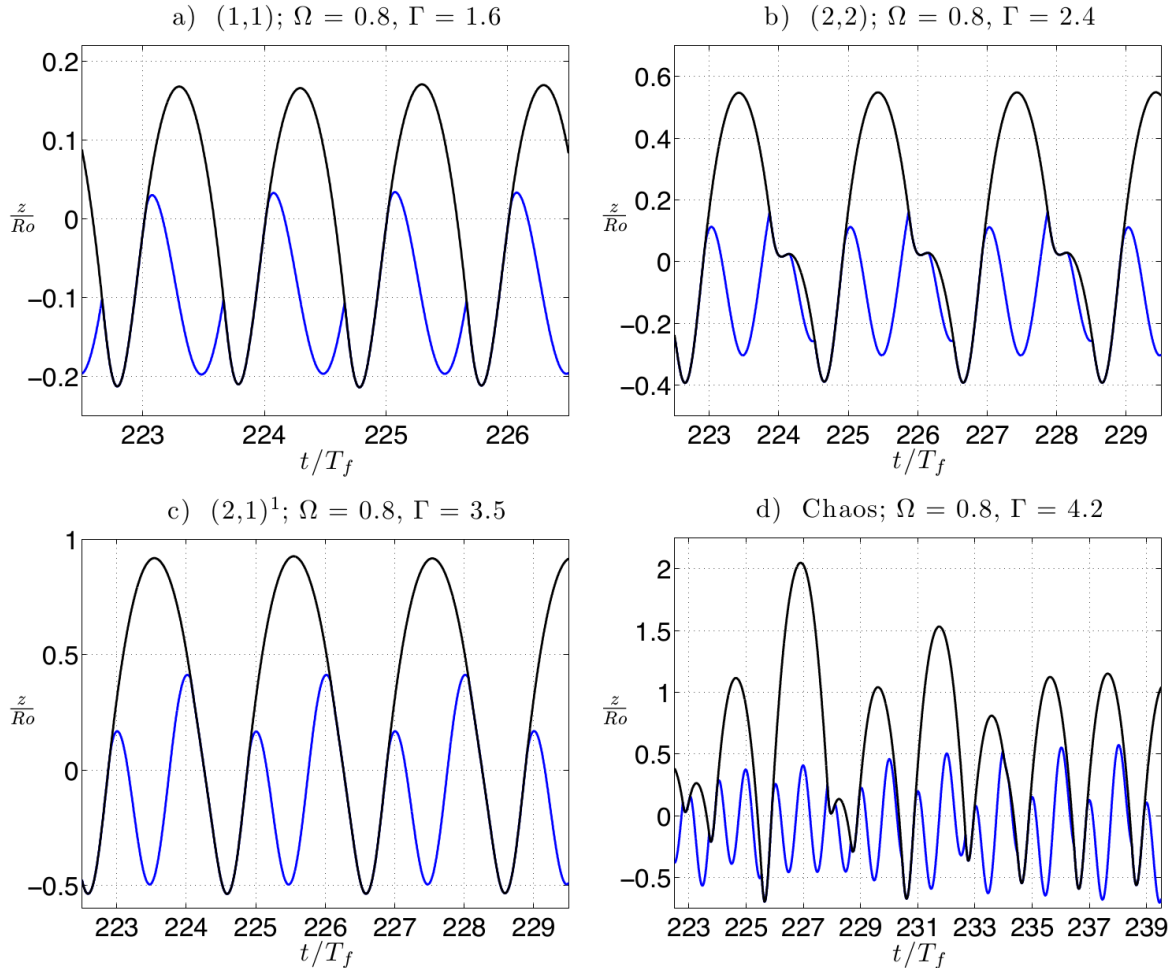


Figure 4.3: Modes of bouncing for $\Omega = 0.8$ as determined by the periodicity of $q(t)$ (black) and $\eta(0, t)$ (blue).

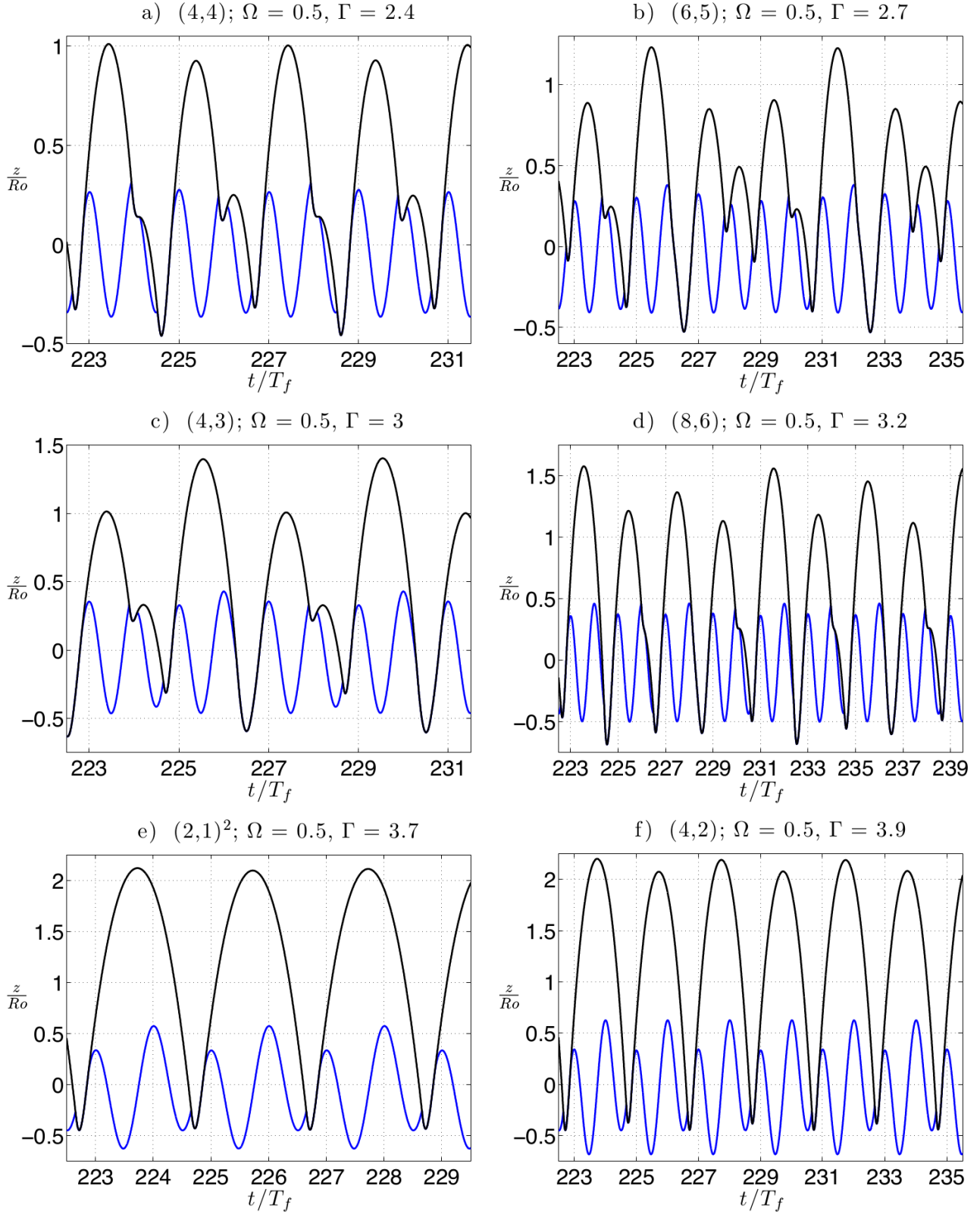


Figure 4.4: Some modes of bouncing that appear for $\Omega = 0.5$ as determined by the periodicity of $q(t)$ (black) and $\eta(0,t)$ (blue).

We differentiate between two kinds of $(2, 1)$ modes, following [41]. We have the $(2, 1)^1$ mode, and the $(2, 1)^2$. The latter being the one that produces longer flights, shorter contacts and

higher jumps. We find a clear separation between the two, given by the sign of the velocity of the fluid surface beneath the drop center at the time of impact. In the $(2, 1)^2$ mode, the droplet impacts on a part of the free surface that has a positive (upward) velocity; while in the $(2, 1)^1$ mode, such velocity is negative.

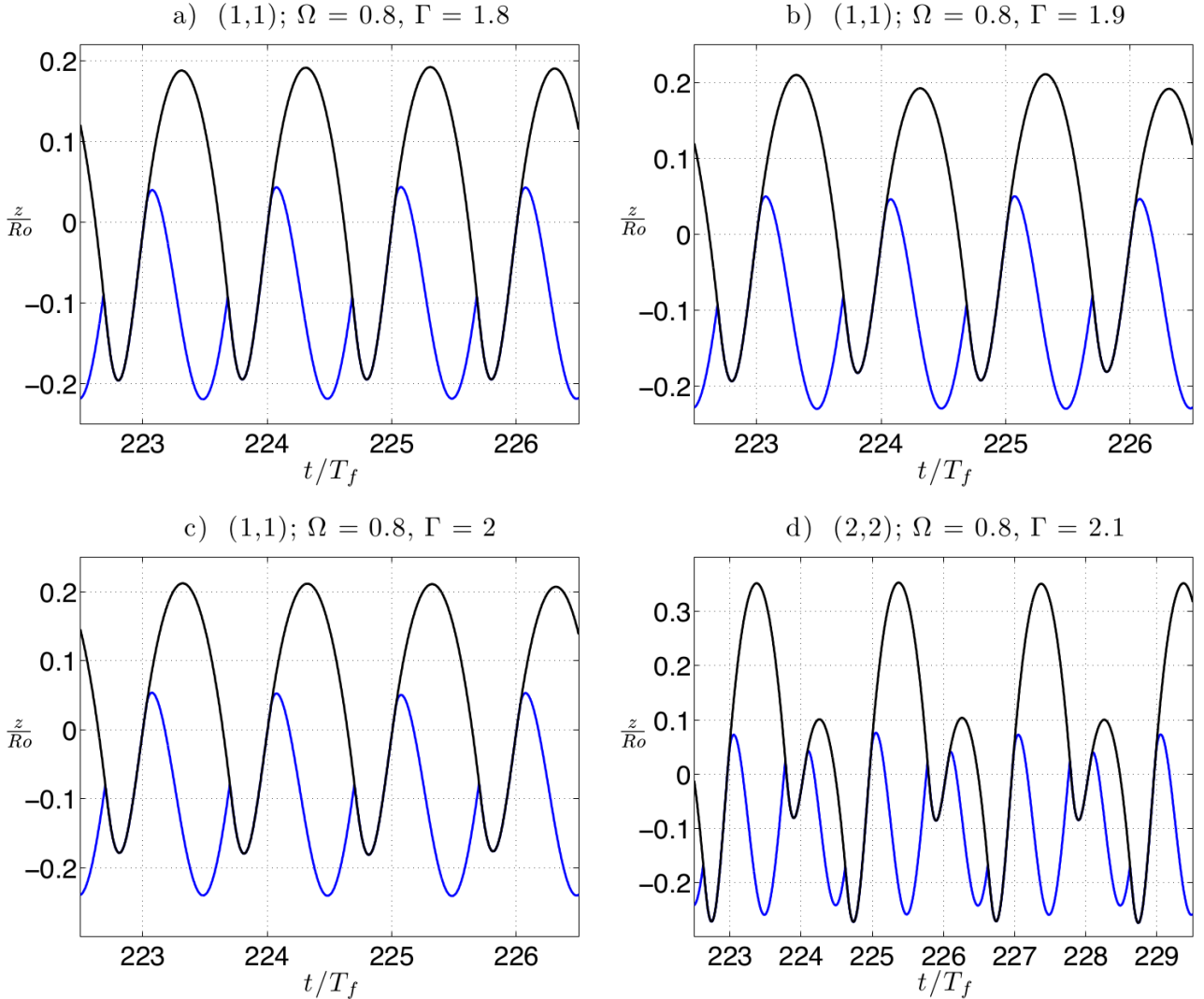


Figure 4.5: Typical transition from the $(1, 1)$ to the $(2, 2)$ bouncing mode, as predicted by our model. The black curve corresponds to $q(t)$, the blue one to $\eta(0, t)$.

Figure 4.5 shows the transition between the $(1, 1)$ and $(2, 2)$ modes, as arises when Γ is increased. Notice that for $\Gamma = 1.8$ (Figure 4.5-a) we have the $(1, 1)$ mode; for $\Gamma = 1.9$ (Figure 4.5-b) there is evidence of the onset of a period-doubling transition, which then disappears for $\Gamma = 2$ (Figure 4.5-c). We still consider the case of $\Gamma = 1.9$ a $(1, 1)$ mode; since the difference in the height of two consecutive bounces is a tiny fraction of the radius of the drop. For $\Gamma = 2.1$ (Figure 4.5-d) vertical motion has suddenly changed in a radical way. It may be thought fair to consider the case of $\Gamma = 1.9$ a $(2, 2)$ mode bouncer; however, when looking at a long sequence of bounces, the drop will occasionally skip a bounce of this alternating sequence. Thus we take this as a manifestation of the proximity to the sharp transition arising at a slightly higher Γ .

Figure 4.4 shows some of the modes obtained with $\Omega = 0.5$. Notice that for $\Gamma = 3.9$ (Figure 4.4) one could argue that the consecutive bounces are different by a very small fraction of the radius, and thus it could be tempting to simply consider this as a $(2, 1)^2$ mode bouncer; however, the difference though small is robust in time, and thus we considered it to be a distinct mode. Figures 4.3 and 4.4 are analogs of Figure 3.2; when comparing them, one can immediately see that with this model there is, by construction, no longer overlap nor gap between the drop and bath interfaces during contact.

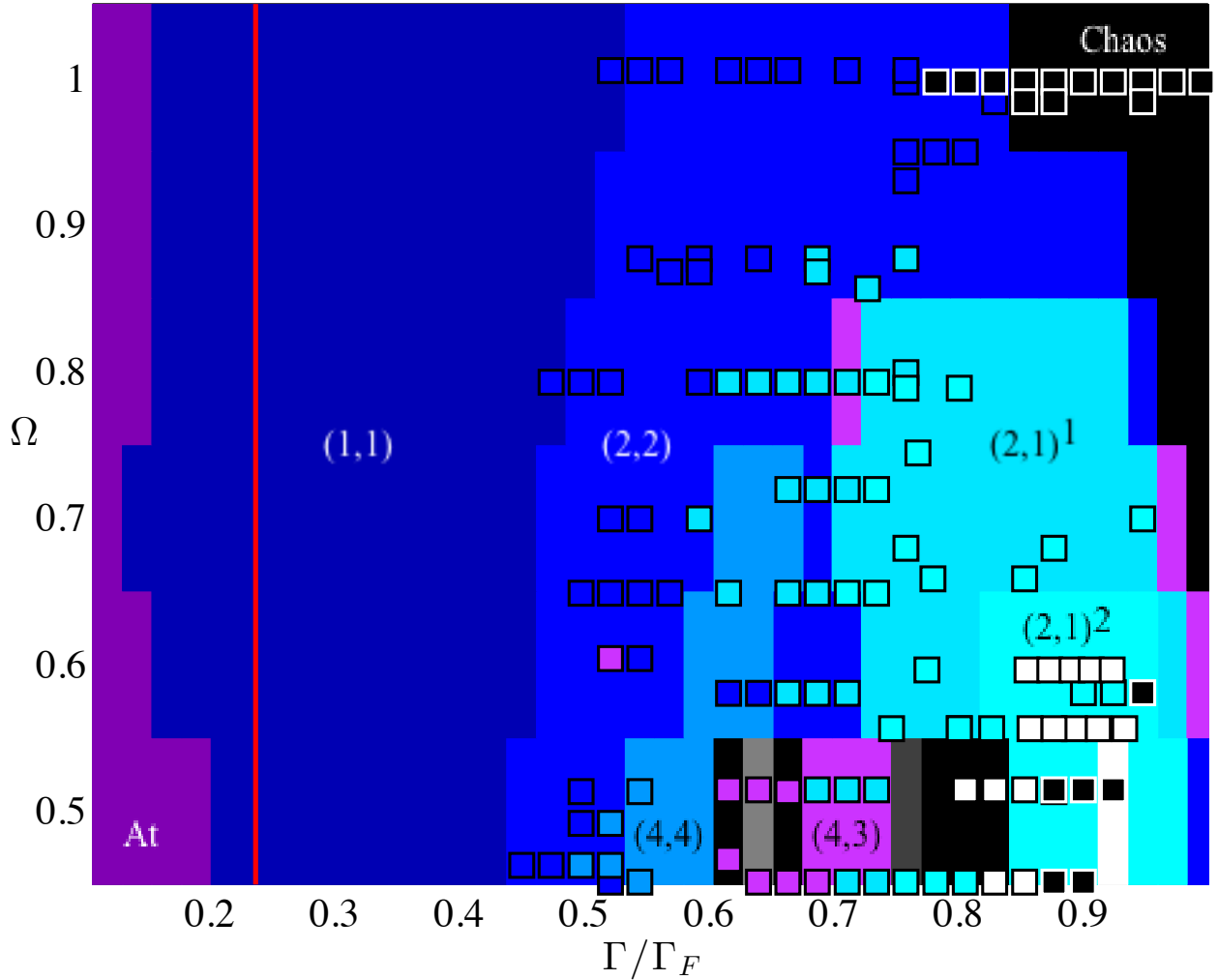


Figure 4.6: Regime diagram of bouncers. The background is color coded according to the mode of bouncing observed in our simulations. *At* stands for *attached*, and corresponds to regimes for which the drop is always in contact with the bath; light gray is a $(6, 5)$ mode; dark gray, a $(8, 6)$ mode; white, a $(4, 2)$ mode. The squares show experimentally observed bouncers, reported in [53]; the color coding of the squares is the same as that of the background. The red vertical line corresponds to $\Gamma = 1$.

Figure 4.6 is a regime diagram which presents the region of the $\Gamma/\Gamma_F - \Omega$ plane explored in our simulations. Each tile in Figure 4.6 is colored according to the result of the experiment with parameter values that correspond to the center of the tile. The mapping of the $\Gamma - \Omega$ plane was done with an interval of 0.1 in each direction. Since in this model coalescence is not

a possibility in this model, the left most region (labeled *At*) of Figure 4.6 show the regimes where the drop never detaches from the surface. In comparing Figure 4.6 to Figure 3.3, the improvement obtained by the present model for low and intermediate values of Γ/Γ_F is evident.

Notice that, in all these reported experiments, axial symmetry is imposed *a priori*; hence we can not have a walker. It is very likely that some of the bouncing solutions here presented are actually not stable; in the future we expect to develop a model for walkers based on the kinematic match of the surfaces which will provide the possibility to explore, with this model, the stability, multiplicity of bouncing states, and hysteresis observed in the laboratory [53].

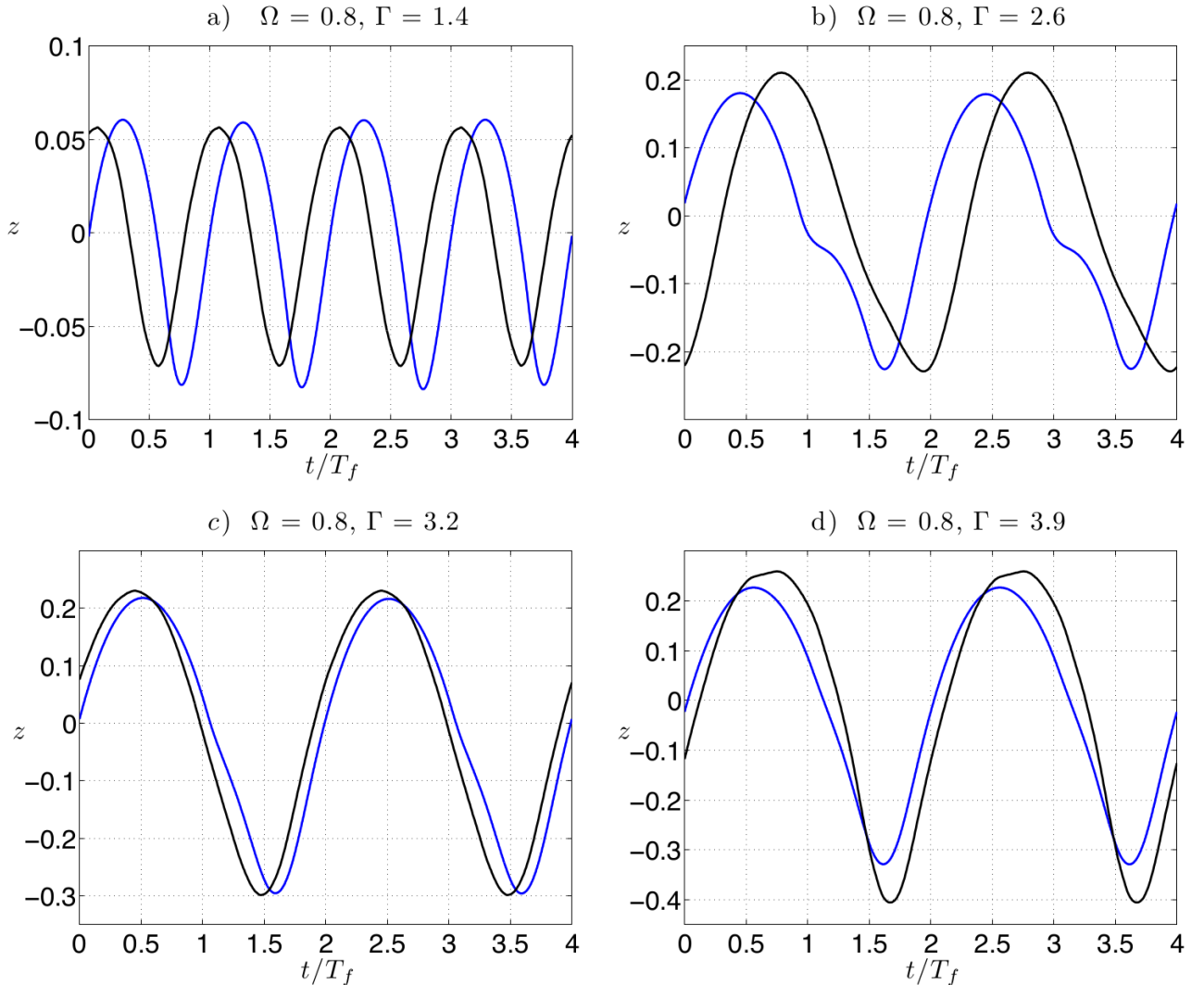


Figure 4.7: Comparison of the experimental measurements of the vertical motion of a drop (black), to the predictions of the kinematic matching model (blue). Vertical axes are in mm.

Figure 4.7 shows a comparison between the vertical motion of the drop, as measured in the laboratory and predicted by our model. Notice that in Figure 4.7-d the experimental data corresponds to a walker and the simulation to a bouncer; thus, one might expect to see less agreement. Nevertheless, we include the comparison, since this is the most reasonable data set available to which we can compare this predictions. Here again, we use the convention that the

phase of the shaker ϕ is zero at the moment of maximum elevation of the bath.

Figure 4.8 shows a comparison between the phases of impact and take off of the same drop at different values of Γ/Γ_F . Notice that there is one bouncer for which simulations indicate one more contact per period relative to the experimental results. This corresponds to the only (4, 3) bouncer that can be found for $\Omega = 0.8$ in our sweep as reported in Figure 4.6.

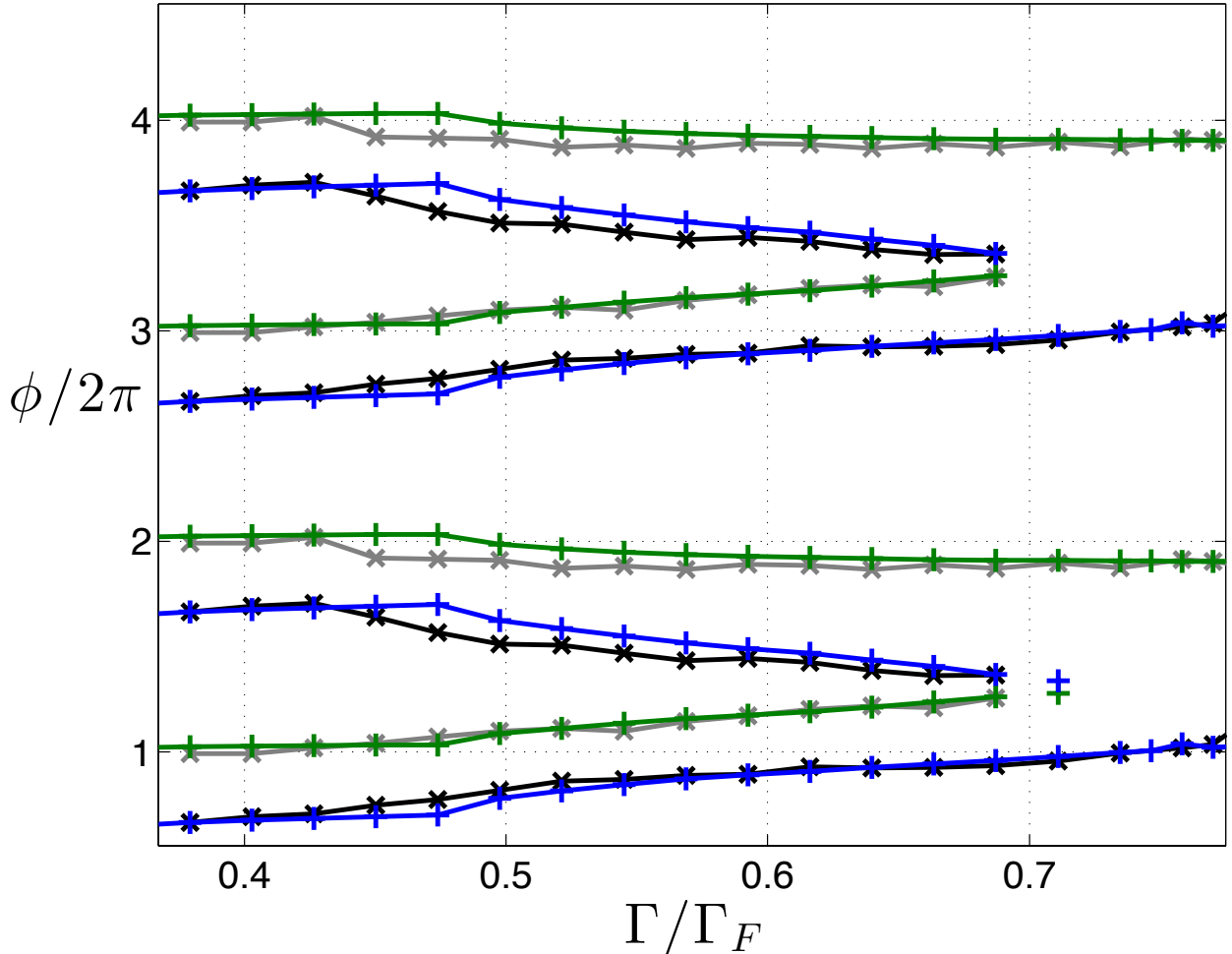


Figure 4.8: Experimental phases of impact (black) and take off (gray), compared to predictions by the kinematic matching model (impact, blue; take off, green). The vertical axis corresponds to the phase of the shaker, with the convention that maximum height of the bath is attained at $\phi = 0$.

Figure 4.8 should be compared to the left most part of Figure 3.7. This comparison indicates an improved agreement in the phase of contact for bouncers with the present model. Another improvement that becomes evident, is that the region where simulations predict a (4, 3) mode, not observed in the experiments, has shrunk to a single point, namely that arising at $\Gamma/\Gamma_F = 0.71$.

Figure 4.9 shows a comparison between the surface *Schlieren* measurements [14], shown in black; with the prediction of the surface elevation made by this model, shown in blue.

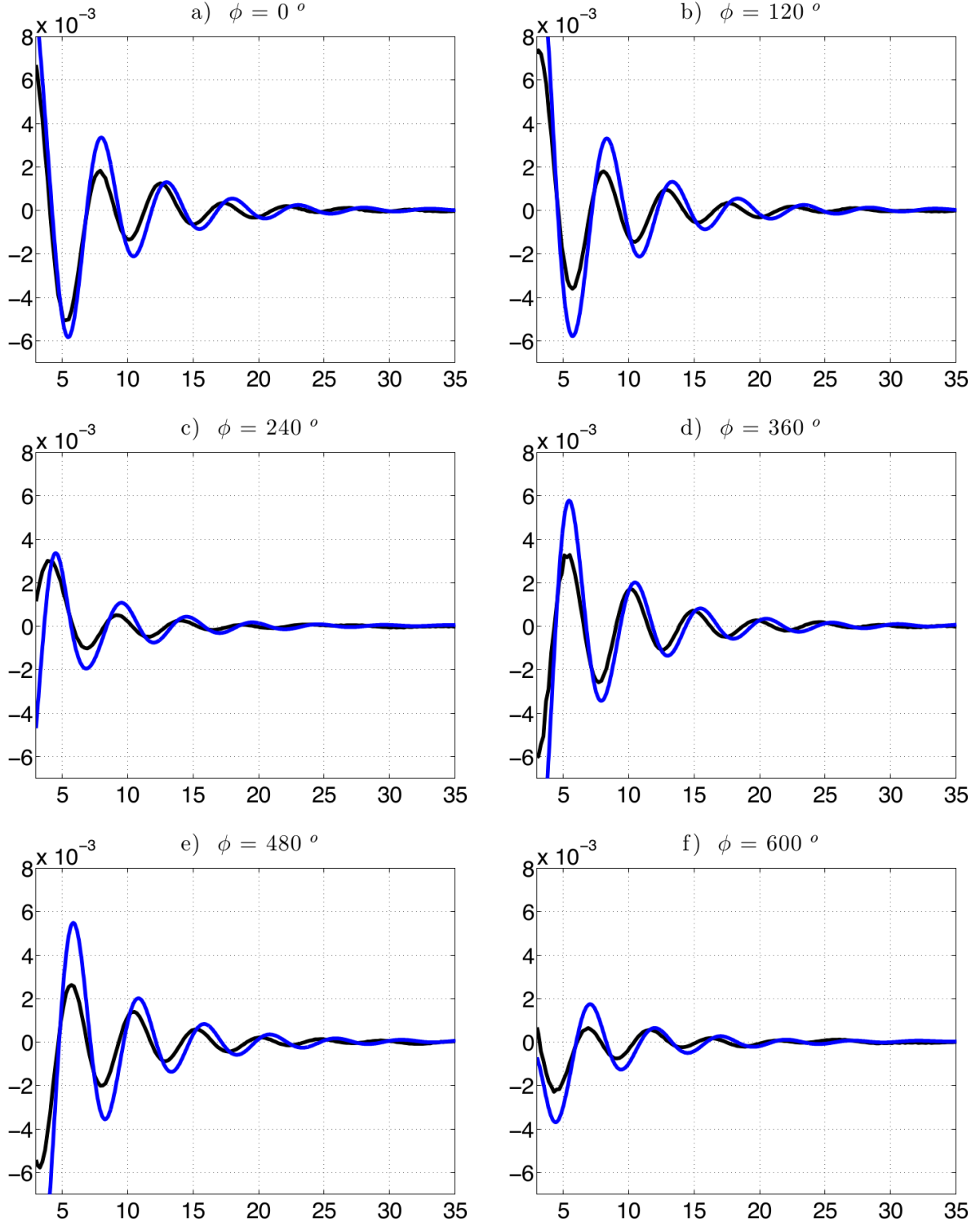


Figure 4.9: Comparison of the radial profiles of the experimental measurements of wave topography (black) for a bouncer with $\Omega = 0.8$ just below the walking threshold to the predictions of the kinematic matching model (blue) for $\Gamma = 3.15$, value that is just below the numerical walking threshold in [38]. The vicinity of the origin is not shown, since in this region, the presence of the drop interferes with the measurements. Axes are in mm .

It is important to highlight that the main virtue of this model is its ability to predict accurately a bouncer with absolutely no fitting parameters for the surface-droplet interaction.

4.4.2 Possible Improvements

With the current mesh, simulations of a few seconds of the experiment takes a couple of days. Currently, we use a grid that is unnecessarily fine for the far field and still only reasonably fine near the drop. The possibility of using an inhomogeneous mesh is an advantage of the finite difference method, that we wish to exploit in the future. We hope to improve computing times considerably using an irregular mesh, one that is very fine in the vicinity of the drop and much coarser in the far field.

This model, though mostly predictive maintains one *a posteriori* correction, that applied to the fluid viscosity to correctly match the Faraday threshold. We retain that correction since we are essentially using the results of Chapter 2 to model the surface waves. Chapter 5 presents an alternative modeling of the fluid motion which attempts to deal more carefully with the dissipation, so as to obtain improved predictions that require no such calibrations.

CHAPTER 5

An Improved Viscous Water Wave Model

We present the solution of system (1.67).

5.1 Solving the System

Let us write system (1.67) in matrix form as

$$-(-i\omega)V = M(-i\omega)V + P_\kappa, \quad (5.1)$$

where

$$V = \begin{bmatrix} \eta^{\vec{k}} \\ \phi^{\vec{k}} \end{bmatrix}, \quad (5.2)$$

$$M(-i\omega) = \begin{bmatrix} -\alpha & k \\ -\left(-g + \frac{\sigma}{\rho}k^2\right) & -\alpha - \frac{2\nu k \xi \alpha}{i\omega - \alpha} \end{bmatrix}, \quad (5.3)$$

$$P_\kappa = \begin{bmatrix} 0 \\ \frac{\sigma}{\rho}(k^2 + \kappa)\eta^{\vec{k}} - \frac{p_d^{\vec{k}}}{\rho} \end{bmatrix}; \quad (5.4)$$

and

$$\alpha = 2\nu k^2, \quad (5.5)$$

$$\xi = \sqrt{k^2 + \frac{-i\omega}{\nu}}, \quad (5.6)$$

with $\Re e(\xi) \geq 0$, and $\kappa\eta$ is the curvature of the free surface.

We consider the unperturbed problem, i.e. $p_d = 0$ and $g(t) = g_0$. We recall that we have assumed that the wave amplitude is very small when compared to the wavelength, as happens in the case in the bouncing droplets problem, for which wave amplitude is typically less than $25\mu\text{m}$ [13]. For such small amplitudes, we will assume

$$\kappa\eta^{\vec{k}} \approx \Delta_H\eta^{\vec{k}} = k^2\eta^{\vec{k}}, \quad (5.7)$$

that is, $P_\kappa = 0$. Under these circumstances, equation (5.1) becomes

$$\left[M(-i\omega) - (-i\omega)I \right] V = 0; \quad (5.8)$$

which only admits a non trivial solution if

$$\det \left(\left[M(-i\omega) - (-i\omega)I \right] \right) = 0 \quad (5.9)$$

i.e.

$$\det \begin{pmatrix} i\omega - \alpha & k \\ -\left(-g_0 + \frac{\sigma}{\rho}k^2\right) & i\omega - \alpha - \frac{2\nu k \xi \alpha}{i\omega - \alpha} \end{pmatrix} = 0. \quad (5.10)$$

We thus have

$$(i\omega - \alpha)^2 + \beta^2 = 2\nu k \xi \alpha, \quad (5.11)$$

where

$$\beta = \sqrt{k \left(-g_0 + \frac{\sigma}{\rho}k^2 \right)}. \quad (5.12)$$

Recall that, by (2.15), $\vec{g} = g(t)\hat{z}$, thus normal gravity implies $\vec{g} = g_0\hat{z}$, with $g_0 < 0$, rendering

$$k \left(-g_0 + \frac{\sigma}{\rho}k^2 \right) > 0; \quad (5.13)$$

and thus we can assume $\beta > 0$. Let us now go back to equations (5.6) and (5.5) which imply

$$\xi = k \sqrt{1 + \frac{2(-i\omega)}{\alpha}}, \quad (5.14)$$

with $\Re e(\xi) \geq 0$. If we now substitute ξ as given by (5.14) into equation (5.11), we obtain

$$(\alpha + (-i\omega))^2 + \beta^2 = \alpha^2 \sqrt{1 + \frac{2(-i\omega)}{\alpha}}; \quad (5.15)$$

which is the dispersion relation for this problem, and where

$$\Re e \left(\sqrt{1 + \frac{2(-i\omega)}{\alpha}} \right) \geq 0. \quad (5.16)$$

Notice now that taking the conjugate of both sides of equation (5.15) yields

$$\left(\alpha + \overline{(-i\omega)} \right)^2 + \beta^2 = \alpha^2 \sqrt{1 + \frac{2\overline{(-i\omega)}}{\alpha}}; \quad (5.17)$$

from which we can see that the conjugate of any value of $-i\omega$ that satisfies (5.15) also satisfies it. Notice also that if a root $-i\omega^*$ of (5.15) satisfies $\Im m(-i\omega^*) \neq 0$, i.e. when we have two distinct complex conjugate roots, condition (1.52) is automatically satisfied. The two conjugate $-i\omega$ values will in turn produce two conjugate values of ξ . The importance of the existence of two complex conjugate values of ξ is explained in Appendix C.

It is simple to show that equation (5.15) has at most four roots, since its square is

$$(\alpha + (-i\omega))^4 + 2\beta^2 (\alpha + (-i\omega))^2 + \beta^4 = \alpha^4 \left(1 + \frac{2(-i\omega)}{\alpha} \right), \quad (5.18)$$

which is a fourth degree polynomial in $-i\omega$; namely

$$(-i\omega)^4 + 4\alpha(-i\omega)^3 + 2(3\alpha^2 + \beta^2)(-i\omega)^2 + 2\alpha(\alpha^2 + 2\beta^2)(-i\omega) + \beta^2(2\alpha^2 + \beta^2) = 0. \quad (5.19)$$

If we now substitute $-i\omega^*$ into equation (5.8) and obtain a non-trivial solution V^* , this V^* determines a solution to the linearized curvature unforced system (1.67) of the form (1.40). Moreover, given the form of M presented in (5.3), it is impossible to subtract any multiple of the identity and obtain the null matrix (it suffices to notice that $g_0 \neq 0$). Thus, no eigenvalue of $M(-i\omega^*)$ can have two linearly independent eigenvectors. Hence, if we wish to construct a solution for arbitrary values of $A(\vec{k})$ and $B^+(\vec{k})$ (from equations (1.40a) and (1.61), respectively) we need to use two different roots of (5.15). This follows from the bidimensionality of the space of solutions of the form (1.40). Besides, notice that there is no *a priori* reason for the corresponding eigenvectors obtained to be linearly independent; since they are eigenvectors of different matrices.

We now claim that two eigenvectors obtained from complex conjugate values of $-i\omega$ must be linearly independent. Indeed, if we suppose that they are linearly dependent, this means that any given one is a multiple of the other (since none can be null). Notice also that even though this is a generalization of the typical eigenvalue problem, it is still true that

$$M(\lambda)V = \lambda V \implies M(\lambda)cV = \lambda cV, \quad (5.20)$$

for any $c \in \mathbb{C}$. Thus, we can assume that the two eigenvalues share an eigenvector. Thus we

have

$$\begin{bmatrix} -\alpha & k \\ -\left(-g + \frac{\sigma}{\rho}k^2\right) & -\alpha + \frac{2\nu k \xi \alpha}{\alpha + (-i\omega^*)} \end{bmatrix} \begin{bmatrix} \eta^{\vec{k},*} \\ \phi^{\vec{k},*} \end{bmatrix} = (-i\omega^*) \begin{bmatrix} \eta^{\vec{k},*} \\ \phi^{\vec{k},*} \end{bmatrix}, \quad (5.21)$$

and

$$\begin{bmatrix} -\alpha & k \\ -\left(-g + \frac{\sigma}{\rho}k^2\right) & -\alpha + \frac{2\nu k \bar{\xi} \alpha}{\alpha + (-i\omega^*)} \end{bmatrix} \begin{bmatrix} \eta^{\vec{k},*} \\ \phi^{\vec{k},*} \end{bmatrix} = \overline{(-i\omega^*)} \begin{bmatrix} \eta^{\vec{k},*} \\ \phi^{\vec{k},*} \end{bmatrix}. \quad (5.22)$$

From the first lines of equations (5.21) and (5.22), we have

$$(-i\omega^*) \eta^{\vec{k},*} = -\alpha \eta^{\vec{k},*} + k \phi^{\vec{k},*} = \overline{(-i\omega^*)} \eta^{\vec{k},*}, \quad (5.23)$$

and hence either $\eta^{\vec{k},*} = 0$ or $-i\omega^*$ is real. Since the latter is not the case, we have

$$\eta^{\vec{k},*} = 0. \quad (5.24)$$

Taking (5.24) into the second line of equation (5.21) we have

$$\left(-\alpha + \frac{2\nu k \xi \alpha}{\alpha + (-i\omega^*)} \right) \phi^{\vec{k},*} = (-i\omega^*) \phi^{\vec{k},*}. \quad (5.25)$$

Now, since the eigenvector can not be null by definition, we have $\phi^{\vec{k},*} \neq 0$. Thus

$$\frac{2\nu k \xi \alpha}{\alpha + (-i\omega^*)} = \alpha + (-i\omega^*), \quad (5.26)$$

which implies

$$(\alpha + (-i\omega))^2 - 2\nu k \xi \alpha = 0. \quad (5.27)$$

Finally, notice that equation (5.11) implies

$$(i\omega - \alpha)^2 + 2\nu k \xi \alpha = -\beta^2 < 0, \quad (5.28)$$

and hence contradicts (5.27).

We conclude that if equation (5.15) has at least one root $-i\omega^*$ such that $\text{Im}(-i\omega^*) \neq 0$, we can find a wave-like solution to system (1.67) for any given values of $A(\vec{k})$ and $B^+(\vec{k})$. More importantly, this implies that, for any initial condition of the form

$$\eta(x, y, t=0) = \sum_{\vec{k}} A(\vec{k}) e^{i\vec{k} \cdot \vec{r}}, \quad (5.29)$$

$$\phi(x, y, z = 0, t = 0) = \sum_{\vec{k}} B(\vec{k}) e^{i\vec{k} \cdot \vec{r}}, \quad (5.30)$$

such that for every k involved we can find non-real solutions to equation (5.15); we can calculate the solution to system (1.67). Notice that we can in fact calculate this exactly, since we have a formula for the roots of fourth degree polynomials which can then be tested in (5.15), yielding the exact eigenvalues and eigenvectors. Once that is done, the solution to system (1.67) is given by

$$V^1 = e^{-i\omega t} V_0^1, \quad (5.31a)$$

$$V^2 = e^{\overline{-i\omega t}} V_0^2; \quad (5.31b)$$

since

$$V_t^1 = M^1 V^1 = -i\omega^* V^1, \quad (5.32a)$$

$$V_t^2 = M^2 V^2 = \overline{-i\omega^*} V^2; \quad (5.32b)$$

where

$$M^1 = M(-i\omega^*), \quad (5.33)$$

and

$$M^2 = M(\overline{-i\omega^*}), \quad (5.34)$$

Finally, notice that, if we substitute ξ from equation (5.11) into (5.10), we can calculate the eigenvectors exactly, as functions of ω^* , namely

$$V^1 = \begin{bmatrix} k \\ \alpha + (-i\omega^*) \end{bmatrix}, \quad (5.35a)$$

$$V^2 = \begin{bmatrix} k \\ \alpha + \overline{(-i\omega^*)} \end{bmatrix}. \quad (5.35b)$$

Consequently, whenever there exists a root of (5.15), we can find a matrix form of $M(-i\omega)$ which will be diagonal in the base $\{V^1, V^2\}$. Thus, the system is best expressed as

$$V_t = \mathbb{M}V, \quad (5.36)$$

where

$$\mathbb{M} = \begin{bmatrix} k & k \\ \alpha + (-i\omega^*) & \alpha + \overline{(-i\omega^*)} \end{bmatrix} \begin{bmatrix} -i\omega^* & 0 \\ 0 & \overline{(-i\omega^*)} \end{bmatrix} \begin{bmatrix} k & k \\ \alpha + (-i\omega^*) & \alpha + \overline{(-i\omega^*)} \end{bmatrix}^{-1}; \quad (5.37)$$

yielding

$$\mathbb{M} = \begin{bmatrix} -\alpha & k \\ -\frac{(\alpha + (-i\omega^*))(\alpha + \overline{(-i\omega^*)})}{k} & \alpha + (-i\omega^*) + \overline{(-i\omega^*)} \end{bmatrix}. \quad (5.38)$$

Notice that (5.38) can be written as

$$\mathbb{M} = \begin{bmatrix} -\alpha & k \\ -\frac{\alpha^2 + 2\Re e(-i\omega^*) + |-i\omega^*|}{k} & \alpha + 2\Re e(-i\omega^*) \end{bmatrix}, \quad (5.39)$$

from which it is clear that the operator is given by a real matrix.

A final comment is due before we conclude this section. We have shown that the dispersion relation (5.15) squared is a fourth degree polynomial with real coefficients (5.19); and hence (5.19) has exactly 4 complex roots, which can either be all real or include one or two complex conjugate pairs. We also know that any root of the dispersion relation (5.15) must be a root of its square (5.19), and these facts led us to conclude that our dispersion relation has at most four roots. Notice that condition (5.16) implies that there is in principle no reason for any root of (5.19) to be a root of (5.15). Thus, it is possible that the method here presented yields no solution or a non-unique solution to the problem, the latter case occurring if we find four roots for (5.15). In the case of the parameters that were explored, neither of these two were ever the case, that is to say we always found the unique pair of complex conjugate roots for the dispersion relation given in (5.15).

5.2 Faraday Forcing

We now try to find an approximate wave-like subharmonic solution to system (1.35) with $p_d = 0$ and when

$$g(t) = g_0(1 - \Gamma \cos(\omega_0 t)). \quad (5.40)$$

This is inspired in the simulations results we have observed for this physical system, where we see that the subharmonic component dominates the solution.

We consider the following ansatz

$$\eta^{\vec{k}} = E^+ e^{(v+i\frac{\omega_0}{2})t} e^{\vec{k} \cdot \vec{r}} + E^- e^{(v-i\frac{\omega_0}{2})t} e^{\vec{k} \cdot \vec{r}}, \quad (5.41a)$$

$$\phi^{\vec{k}} = F^+ e^{(v+i\frac{\omega_0}{2})t} e^{\vec{k} \cdot \vec{r}} e^{kz} + F^- e^{(v-i\frac{\omega_0}{2})t} e^{\vec{k} \cdot \vec{r}} e^{kz}, \quad (5.41b)$$

$$w^{3,\vec{k}} = G^+ e^{(v+i\frac{\omega_0}{2})t} e^{\vec{k} \cdot \vec{r}} e^{\xi z} + G^- e^{(v-i\frac{\omega_0}{2})t} e^{\vec{k} \cdot \vec{r}} e^{\bar{\xi} z}. \quad (5.41c)$$

Notice that, by construction, $\phi^{\vec{k}}$ and $w^{3,\vec{k}}$ satisfy the Laplace and heat equation, respectively (see section 1.2).

Ansatz (5.41) must satisfy approximately

$$\eta_t = N\phi + w^3, \quad \text{on } z = 0; \quad (5.42a)$$

$$\phi_t = g\eta + \frac{\sigma}{\rho} \kappa\eta + 2\nu\Delta_H\phi - 2\nu w_z^3, \quad \text{on } z = 0; \quad (5.42b)$$

$$w_t^3 = 2\nu\Delta_H(N\phi + w^3), \quad \text{on } z = 0; \quad (5.42c)$$

We now substitute ansatz (5.41) into equation (5.42) and after canceling $e^{vt+i\vec{k}\vec{r}}$ from every term and separating waves that travel in opposite direction, we obtain

$$QR = 0; \quad (5.43)$$

where

$$R = \begin{bmatrix} E^+ & F^+ & G^+ & E^- & F^- & G^- \end{bmatrix}^T \quad (5.44)$$

$$Q = \begin{bmatrix} -\lambda & k & 1 & 0 & 0 & 0 \\ -\frac{\beta^2}{k} & -\lambda - \alpha & -2\nu\xi & -\frac{g_0\Gamma}{2} & 0 & 0 \\ 0 & -\alpha k & -\lambda - \alpha & 0 & 0 & 0 \\ 0 & 0 & 0 & -\bar{\lambda} & k & 1 \\ -\frac{g_0\Gamma}{2} & 0 & 0 & -\frac{\beta^2}{k} & -\bar{\lambda} - \alpha & -2\nu\bar{\xi} \\ 0 & 0 & 0 & 0 & -\alpha k & -\bar{\lambda} - \alpha \end{bmatrix}; \quad (5.45)$$

and

$$\lambda = \left(v + i\frac{\omega_0}{2} \right); \quad (5.46)$$

where v and ω_0 are real numbers and we have disregarded terms of the form $-\frac{g_0\Gamma}{2}E^+e^{i3\frac{\omega_0}{2}t}$ and $-\frac{g_0\Gamma}{2}E^-e^{-i3\frac{\omega_0}{2}t}$.

We wish to find non trivial solutions to (5.43). Thus, we need to solve $\det(Q) = 0$, which yields

$$g_0^2 k^2 |\lambda|^2 \Gamma^2 = 4 \left| \alpha\beta^2 k - k\beta^2 (\lambda + \alpha) - \lambda (\lambda + \alpha)^2 + 2\nu\xi\alpha k \lambda \right|^2 \quad (5.47)$$

which can be used to estimate the damping that will be predicted by this model for a given Γ , or alternatively to find the value of Γ such that a given damping is expected. In particular, for null damping at some given k we can substitute $v = 0$ into equation (5.46) and take the result into equation (5.47). This yields a value of Γ for each k , beyond which we expect to observe

Faraday instability in our system.

Thus the value of Γ_F^p predicted by this model is given by the minimum of

$$\Gamma = \frac{4 \left| \alpha\beta^2 k - k\beta^2 \left(i\frac{\omega_0}{2} + \alpha \right) - i\frac{\omega_0}{2} \left(i\frac{\omega_0}{2} + \alpha \right)^2 + i2\nu\xi\alpha k\frac{\omega_0}{2} \right|}{g_0 k |\omega_0|}, \quad (5.48)$$

and the minimizing argument k_F^p corresponds to the predicted Faraday wave length.

A final remark is in order. It is possible to verify the stability of system (1.35) more rigorously, using Floquet theory to find a numerical estimate of the Poincaré map since this a linear system with periodical coefficients. In the present work, we limit our approach to this analytical estimate. We wish to do a more rigorous validation in the future.

5.2.1 Some Examples

We compare the predictions of equation (5.48) to the experimental results reported in [53] where three parameter combinations are tested. In all three cases the predicted Faraday wavelength matches that of subharmonic waves in the capillary-gravity dispersion relation with less than 1% error.

For the 50 *cSt* viscosity silicon oil with density of 0.965 *gr/cm*³ and surface tension of 20.8 *dyne/cm* which was shaked at a frequency of 50 *Hz* the experimental Faraday threshold was found to be at $\Gamma = 4.23$. For this configuration, equation (5.48) predicts $\Gamma = 4.05$, yielding a 4.3% error.

The 20 *cSt* viscosity silicon oil with density of 0.949 *gr/cm*³ and surface tension of 20.6 *dyne/cm* when shaked at a frequency of 70 *Hz* was reported to reach Faraday instability at $\Gamma = 3.33$ and when shaked at 80 *Hz* of $\Gamma = 4.22$. The corresponding predictions of equation (5.48) are $\Gamma = 3.30$ and $\Gamma = 4.15$, yielding errors of 0.9% and 1.6%, respectively.

Figure 5.1 presents the values of Γ for neutral stability as predicted by equation (5.48) for the 20 *cSt* and 80 *Hz* set up, reported in [53]. Values of Γ above the black curve are expected to show exponential growth in time for the corresponding wave numbers k . Figure 5.1, when compared to Figure 2.1, shows the improvement in the prediction of the Faraday threshold; specifically, the error is reduced by roughly a factor of 14. As a consequence of this improvement, this fluid model can be used without a correction of viscosity of the kind imposed before.

Remark 1. The model developed in this chapter can be used for a variety of wave problems in which viscous effects are not negligible. The Faraday wave problems considered here are just one example.

Remark 2. We notice that using the solution of system (1.67) as calculated in Chapter 5, we can check the adequacy of the high Reynolds number approximation made in section 2.1. In particular, for the physical parameters used in the experiments modeled in Chapter 3, we can

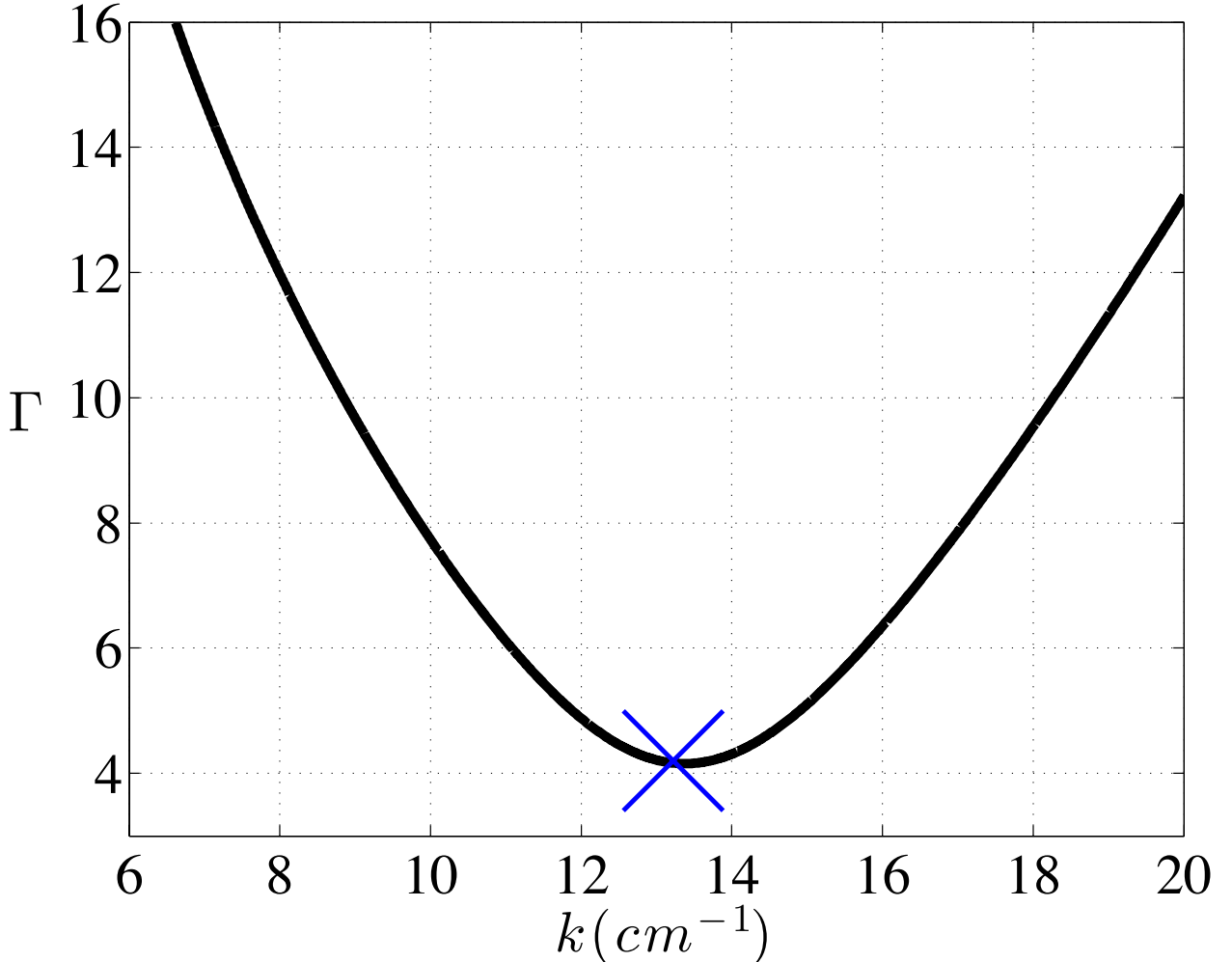


Figure 5.1: Prediction of the Faraday threshold for silicone oil with 20 cS viscosity, 0.949 gr/cm^3 density, 20.6 dyne/cm surface tension, shakes at 80 Hz . The black curve shows the value of Γ for neutral stability of each wave number k , as predicted by equation (5.48). The blue marker corresponds to the experimental results for the same configuration [53]

find the value of ϵ_0 as given in equation (2.4). Essentially

$$\epsilon_0 = \frac{\sqrt{1 + 2 \frac{-i\omega^*(k_F)}{\alpha(k_F)}}}{1 + \frac{-i\omega^*}{\alpha(k_F)}} = 0.76,$$

which is smaller than one, but hardly negligible. It would thus seem appropriate using the model presented in Chapter 5.

This page was intentionally left blank.

General Overview and Future Directions

The model presented in Chapter 3 was able reproduce every one of the behaviors we tested on it, at least in a qualitative way. Moreover, it is the first to show evidence of reproducing accurately the vertical motion and phases of contact of the drops, as well as the features of the surface waves; reported by the most precise experimental measurements yet available. Much more exploration could be done with such model; e.g. studying pairs of droplets of different size, searching for more experimentally reported orbital states, exploring behaviors of set of three or more droplets, characterizing the predicted multiplicity of states and hysteresis, exploring the interaction of walkers with submerged topographies, exploring the behavior of droplets under the effect of electric or magnetic fields.

The model developed in Chapter 4, produces bouncers that are qualitatively similar to those produced with the model of Chapter 3, moreover, quantitative predictions for bouncers improve with this model. In a sense, Chapter 4 presents the converse view of what was done in [50], where all effects due to surface waves are removed, and they only keep those that are due to drop deformation. The accuracy of the predictions obtained is evidence that in the regime we studied, droplet deformation effects are not necessary to generate the observed dynamics.

The model of Chapter 4 could be adapted for the case of walkers. There is in principle no reason why this can't be done; it will, nevertheless, require some modeling choices to determine the contact area. There is the possibility of iterating on the pressure field instead of decomposing the domain into two parts as we currently do. Doing so could allow for the use of a spectral method to solve the fluid equations, and thus take greater advantage of the form in Fourier space of the operators involved. It would also be interesting to include droplet deformation and air layer dynamics into this model, to understand better the role of these two variables in this problem.

In Chapter 5 we showed that through a more careful treatment of the dissipative effects, we can better estimate the Faraday threshold. It is then reasonable to expect that such a model will be more successful at describing phenomena that take place near the Faraday threshold. This fluid model can be combined with the surface droplet interaction model presented in Chapter 3

to see the extent to which predictions are improved.

In the future, we wish to combine the improved fluid model from Chapter 5 with a model of surface-droplet interaction based on the kinematic match we presented in Chapter 4. We believe we can adapt the methods of Chapter 4 to Fourier space, using an iteration on the pressure distribution to match the geometrical constraints. Such a method would preserve the advantages of working on a space in which some of the operators involved have a diagonal form; in a similar way as was done in Chapters 3 and 5. It would, in principle, have the ability to predict a bouncer with no coefficients of any kind to be tuned; thus maintaining also the main desirable features of the model presented un Chapter 4.

Appendices

This page was intentionally left blank.

APPENDIX A

Linearization

In modeling Bouncing droplets we are looking at a system that, with every impact of a drop on the surface, essentially triggers standing waves of the form

$$\eta \approx A \cos\left(\frac{2\pi}{\lambda_F}x\right) \cos(\omega_0 t), \quad (\text{A.1})$$

where η is the surface elevation, and we have omitted a temporal decay that depends on proximity to the Faraday threshold. The surface elevation will approximately be a combination of this type of waveforms up to some translations and rotations around the z axis. Thus, we know

$$\eta_t \approx \omega_0 A \cos\left(\frac{2\pi}{\lambda_F}x\right) \cos(\omega_0 t). \quad (\text{A.2})$$

Notice that, for the typical experiment that we will be modeling, $\lambda_F \approx 5\text{mm}$, and $A < 25\mu\text{m}$.

Recall now the kinematic boundary condition given by

$$\eta_t = u^3 - \vec{u}_H \cdot \nabla_H \eta, \quad (\text{A.3})$$

where $\vec{u}_H = (u^1, u^2)$ and $\nabla_H \eta = (\eta_x, \eta_y)$. From equation (A.1) we know that a typical value for η is A , and from equation (A.2) that for η_t a typical value is $\omega_0 A$. Also from equation (A.1) we know that a typical value for ∇_H is $2\pi/\lambda$.

Now, let U be a typical value for fluid velocity at the surface; from (A.3) we have

$$\omega_0 A \left[\frac{\eta_t}{\omega_0 A} \right] = U \left[\frac{u^3}{U} \right] - U \left(\frac{2\pi A}{\lambda_F} \right) \left[\vec{u}_H \cdot \nabla_H \eta \right], \quad (\text{A.4})$$

where all magnitudes in brackets are $O(1)$, and $\frac{2\pi A}{\lambda_F} \approx 0.031$; thus we can take $U = \omega_0 A$.

Notice also, that from equation (A.1) a typical value for ∂_t is ω_0 , and consider now the Navier-Stokes equation

$$\vec{u}_t + \vec{u} \cdot \nabla \vec{u} = \vec{g} - \frac{\nabla p}{\rho} + \nu \Delta \vec{u}; \quad (\text{A.5})$$

i.e.

$$\omega_0^2 A \left[\frac{\vec{u}_t}{\omega_0^2 A} \right] + \omega_0^2 A \left(\frac{2\pi A}{\lambda_F} \right) \left[\vec{u} \cdot \nabla \vec{u} \right] = \vec{g} - \frac{\nabla p}{\rho} + \frac{4\pi^2 \nu \omega_0 A}{\lambda_F^2} \left[\Delta \vec{u} \right], \quad (\text{A.6})$$

where once again all quantities in brackets are $O(1)$, and the one in parenthesis is small. Thus, we have

$$\vec{u}_t \approx \vec{g} - \frac{\nabla p}{\rho} + \nu \Delta \vec{u}, \quad (\text{A.7})$$

which produces equation (1.10). Notice that equation (A.4) above also gives us

$$\eta_t \approx u^3; \quad (\text{A.8})$$

which yields equation (1.13).

The free surface is also subject to dynamic boundary conditions, as dictated by the stress tensor, which prescribes

$$\vec{\sigma} = \begin{bmatrix} \sigma^1 \\ \sigma^2 \\ \sigma^3 \end{bmatrix} = \tau \hat{n}; \quad (\text{A.9})$$

where

$$\tau = -pI + \rho \nu \begin{bmatrix} 2u_x^1 & (u_y^1 + u_x^2) & (u_z^1 + u_x^3) \\ (u_x^2 + u_y^1) & 2u_y^2 & (u_z^2 + u_y^3) \\ (u_x^3 + u_z^1) & (u_y^3 + u_z^2) & 2u_z^3 \end{bmatrix}, \quad (\text{A.10})$$

and

$$\hat{n} = \frac{1}{\sqrt{1 + (\eta_x)^2 + (\eta_y)^2}} \begin{bmatrix} -\eta_x \\ -\eta_y \\ 1 \end{bmatrix}. \quad (\text{A.11})$$

Thus we have

$$\vec{\sigma} = \frac{1}{\sqrt{1 + (\eta_x)^2 + (\eta_y)^2}} \begin{bmatrix} 2\rho\nu u_x^1 - p & \rho\nu (u_y^1 + u_x^2) & \rho\nu (u_z^1 + u_x^3) \\ \rho\nu (u_x^2 + u_y^1) & 2\rho\nu u_y^2 - p & \rho\nu (u_z^2 + u_y^3) \\ \rho\nu (u_x^3 + u_z^1) & \rho\nu (u_y^3 + u_z^2) & 2\rho\nu u_z^3 - p \end{bmatrix} \begin{bmatrix} -\eta_x \\ -\eta_y \\ 1 \end{bmatrix}; \quad (\text{A.12})$$

from where

$$\vec{\sigma} \approx \begin{bmatrix} 2\rho\nu u_x^1 - p & \rho\nu (u_y^1 + u_x^2) & \rho\nu (u_z^1 + u_x^3) \\ \rho\nu (u_x^2 + u_y^1) & 2\rho\nu u_y^2 - p & \rho\nu (u_z^2 + u_y^3) \\ \rho\nu (u_x^3 + u_z^1) & \rho\nu (u_y^3 + u_z^2) & 2\rho\nu u_z^3 - p \end{bmatrix} \begin{bmatrix} -\eta_x \\ -\eta_y \\ 1 \end{bmatrix}, \quad (\text{A.13})$$

since

$$\frac{1}{\sqrt{1 + (\eta_x)^2 + (\eta_y)^2}} \approx 1, \quad (\text{A.14})$$

because $|\eta_x| \approx |\eta_y| \approx 0.025$.

Going back to (A.13) we have

$$\vec{\sigma} \approx -\eta_x V^1 - \eta_y V^2 + V^3, \quad (\text{A.15})$$

where V^i is the i -th column of τ , and thus

$$\vec{\sigma} \approx V^3, \quad (\text{A.16})$$

yielding

$$\begin{bmatrix} 0 \\ 0 \\ \sigma \kappa \eta - p_d \end{bmatrix} \approx \begin{bmatrix} \rho \nu (u_z^1 + u_x^3) \\ \rho \nu (u_z^2 + u_y^3) \\ -p + 2\rho \nu u_z^3 \end{bmatrix}, \quad (\text{A.17})$$

i.e. equation 1.14; where σ is the surface tension coefficient, $\kappa \eta$ is twice the mean curvature operator, and p_d is the pressure at the surface. The LHS of equation (A.16) is constructed using the a no strecht condition in the tangential direction a pressure jump by surface tension condition in the normal direction. There we used once more the approximation $\hat{n} \approx \hat{z}$.

We use the standard linearization of the free surface wave problem, i.e. we solve the vector field of velocities on the negative half-space, and use the velocity on the plane $z = 0$ to calculate the evolution of the free surface elevation η .

This page was intentionally left blank.

APPENDIX B

The Dirichlet to Neumann Operator

B.1 The Laplace Problem

Consider the Laplace problem

$$\Delta u = 0, \quad (\text{B.1})$$

in the negative half-space $D = \{(x, y, z) ; z < 0\}$ subject to the Dirichlet boundary conditions

$$u = f, \quad (\text{B.2})$$

on $\partial D = \{(x, y, z) ; z = 0\}$. We know that for a sufficiently smooth and decaying f we can obtain a solution to the Laplace problem (B.1) that is continuous in the closure of D . We also know that such a solution will admit a normal derivative on its surface.

We can now consider the function that maps the Dirichlet data on the plane to the normal derivative of the solution to the Laplace equation for that Dirichlet data, which is also defined on the plane.

It takes some care to properly define this map, and more details can be read in Appendix D. Still, for the problems we are here tackling, it will suffice to notice that whenever a Dirichlet boundary condition univocally identifies a solution to the Laplace Problem on the half-space, which has a normal derivative along its boundary, we can define a Dirichlet to Neumann transform adequately enough. In particular; for the case of traveling plane waves solutions obtained by separating variables, we see in section 1.2 that such a transform is very simply defined.

This page was intentionally left blank.

APPENDIX C

Comments on the Solution to the Heat Equation

Notice that for a given wave vector \vec{k} it is possible to combine more than one solution of the form (1.40). In particular, it is possible that we have more than one value of ω associated to a given k , so long as ω satisfies the generalization of the eigenvalue problem given by (1.56). Chapter 5 shows that, indeed that is the case; for the time being we merely wish to point out that more than one value of ω is necessary if we are to obtain a real solution for w^3 of the form (1.40c).

Notice that to satisfy condition (1.41c) we must have

$$\overline{C^{\vec{k},+} e^{\xi z} + C^{\vec{k},-} e^{-\xi z}} = C^{-\vec{k},+} e^{\xi z} + C^{-\vec{k},-} e^{-\xi z} \quad (\text{C.1})$$

which follows from (1.48). Hence we arrive at

$$\overline{C^{\vec{k},+}} e^{\Re e(\xi)z} e^{-i\Im m(\xi)z} + \overline{C^{\vec{k},-}} e^{-\Re e(\xi)z} e^{i\Im m(\xi)z} = \overline{C^{-\vec{k},+}} e^{\Re e(\xi)z} e^{i\Im m(\xi)z} + \overline{C^{-\vec{k},-}} e^{-\Re e(\xi)z} e^{-i\Im m(\xi)z}, \quad (\text{C.2})$$

which must hold for all $z < 0$. Notice that; if $\Im m(\xi) \neq 0$, it is impossible to satisfy (C.2) for all values of z , since the only possibility was to cancel the first term of the left hand side (LHS) with the first term of the RHS, given that each one is the only one term in each side that decays in z , but the imaginary parts have angles that change with z in opposite ways.

Notice that, in particular, if we can add a similar solution with $\bar{\xi}$ instead of ξ ; equation (C.2) would come to have four terms on each side that would precisely cancel.

Finally, recall equation (1.47), and notice that it is enough for $-i\omega$ to take two complex conjugate values to produce the balance we need. This is in fact the case, and thus we can obtain a real solution, as is shown in Chapter 5.

This page was intentionally left blank.

APPENDIX D

The N Transform for the Laplace Problem in the Half-space

D.1 How to compute the N map

D.1.1 The Neumann to Dirichlet map

The following is a deduction of the Neumann to Dirichlet map for the case of the half space. This was obtained by a slight modification of a more elaborate case presented in [26].

Let $\phi(x, y, z)$ be a solution of the Laplace problem for the half space that decays sufficiently at infinity (take "sufficiently" to mean that it satisfies the necessary decay for boundary integral terms to converge to zero as the domain approaches infinity). For any $\vec{r} = (x, y, 0)$

$$\psi_{\vec{r}}(\vec{q}) = \frac{1}{|\vec{r} - \vec{q}|},$$

where $\vec{q} = (x', y', z')$. We can also define the compact domain of integration Λ , shown in figure (D.1), bounded by the negative half spheres D_1 and D_2 with center at \vec{r} and radii r_1 and r_2 respectively, and the plane annulus D_3 bounded by the circles C_1 and C_2 (of radii r_1 and r_2).

We use Green's second identity in Λ as follows

$$\int_{\Lambda} \frac{1}{|\vec{r} - \vec{q}|} \Delta \phi(\vec{q}) - \phi(\vec{q}) \Delta \frac{1}{|\vec{r} - \vec{q}|} dV(\vec{q}) = \int_{D_1 \cup D_2 \cup D_3} \frac{1}{|\vec{r} - \vec{q}|} \partial_{\hat{n}} \phi(\vec{q}) - \phi(\vec{q}) \partial_{\hat{n}} \frac{1}{|\vec{r} - \vec{q}|} dA(\vec{q}), \quad (\text{D.1})$$

where \hat{n} denotes the outward pointing unit normal to the boundary. Notice that both terms on the left hand side of the equation above vanish since ϕ as well as $\psi_{\vec{r}}$ are Laplacian free on Ω .

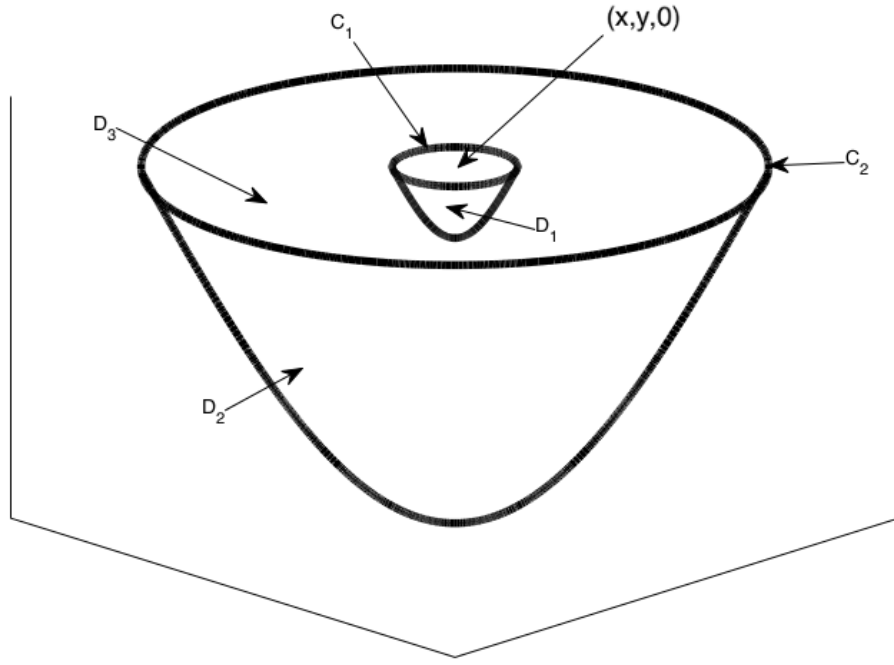


Figure D.1: Domain of integration Λ , where we apply Green's second Identity.

This renders equation (D.1) into

$$\int_{D_1 \cup D_2 \cup D_3} \phi(\vec{q}) \partial_{\hat{n}} \frac{1}{|\vec{r} - \vec{q}|} dS(\vec{q}) = \int_{D_1 \cup D_2 \cup D_3} \frac{1}{|\vec{r} - \vec{q}|} \partial_{\hat{n}} \phi(\vec{q}) dS(\vec{q}) \quad (\text{D.2})$$

Notice that because the normal vector to D_3 is tangent to the level sets of $\frac{1}{|\vec{r} - \vec{q}|}$, the left hand side integral in equation (D.2) is identically zero for any domain like D_3 . Also both integrals on D_2 will vanish as $r_2 \rightarrow \infty$ according to our initial decay hypothesis, which is also assumed of $\nabla \phi$. Moreover; notice that the integral on the right hand side, when evaluated on D_3 , converges as $r_2 \rightarrow \infty$, since the $1/r$ factor is ever smaller and ϕ decays enough at infinity. Whence from equation (D.2), once the limit of $r_2 \rightarrow \infty$ is taken, we obtain

$$\int_{D_1} \phi(\vec{q}) \partial_{\hat{n}} \frac{1}{|\vec{r} - \vec{q}|} dS(\vec{q}) = \int_{D_1} \frac{1}{|\vec{r} - \vec{q}|} \partial_{\hat{n}} \phi(\vec{q}) dS(\vec{q}) + \int_{|\vec{r} - \vec{q}| > r_1} \frac{1}{|\vec{r} - \vec{q}|} \partial_{\hat{n}} \phi(\vec{q}) dA(\vec{q}), \quad (\text{D.3})$$

where $dA(\vec{q}) = dx' dy'$.

Consider now the first integral on the right hand side above in spherical coordinates

$$\int_{D_1} \frac{1}{|\vec{r} - \vec{q}|} \partial_{\hat{n}} \phi(\vec{q}) dA(\vec{q}) = \int_{z' \leq 0} \frac{1}{r'_1} \partial_{\hat{n}} \phi(r_1, \theta) r'_1 dS^2(\vec{q}) \xrightarrow{r_1 \rightarrow 0} 0,$$

where S^2 is the form of area of the unit sphere in three dimensions. Moreover, notice that

$$\partial_{\hat{n}} \frac{1}{|\vec{r} - \vec{q}|} = \frac{1}{r_1^2} \quad \text{on } D_1,$$

which follows from the function and the normal being radial. Therefore we have

$$\int_{D_1} \phi(\vec{q}) \partial_{\hat{n}} \frac{1}{|\vec{r} - \vec{q}|} dS(\vec{q}) = 2\pi \underbrace{\frac{1}{2\pi r_1^2} \int_{S^2} \phi(\vec{q}) r_1^2 dS^2(\vec{q})}_{\bar{\phi}(\vec{r}, r_1)} = 2\pi \bar{\phi}(\vec{r}, r_1) \xrightarrow{r_1 \rightarrow 0} 2\pi \phi(\vec{r}), \quad (\text{D.4})$$

where $\bar{\phi}$ is the average of ϕ in the negative half sphere of center \vec{r} and r_1 radius, which by continuity converges to $\phi(\vec{r})$. We take now the limit of $r_1 \rightarrow 0$ on equation (D.3) and obtain:

$$\phi(\vec{r}) = \frac{1}{2\pi} P.V. \int \frac{1}{|\vec{r} - \vec{q}|} \partial_{\hat{n}} \phi(\vec{q}) dA(\vec{q}). \quad (\text{D.5})$$

D.1.2 Inverting the Neumann to Dirichlet map

Notice that since $\phi_{z'}$ is also a solution to the Laplace problem in the half space that is also assumed to decay sufficiently, we can follow exactly the same steps from above, up until equation (D.2) to obtain

$$\int_{D_1 \cup D_2 \cup D_3} \phi_{z'}(\vec{q}) \partial_{\hat{n}} \frac{1}{|\vec{r} - \vec{q}|} dS(\vec{q}) = \int_{D_1 \cup D_2 \cup D_3} \frac{1}{|\vec{r} - \vec{q}|} \partial_{\hat{n}} \phi_{z'}(\vec{q}) dS(\vec{q}). \quad (\text{D.6})$$

Now, let

$$I_i = \int_{D_i} \phi_{z'}(\vec{q}) \partial_{\hat{n}} \frac{1}{|\vec{r} - \vec{q}|} dS(\vec{q}), \quad (\text{D.7})$$

and

$$J_i = \int_{D_i} \frac{1}{|\vec{r} - \vec{q}|} \partial_{\hat{n}} \phi_{z'}(\vec{q}) dS(\vec{q}), \quad (\text{D.8})$$

for $i = 1, 2, 3$. Hence equation (D.6) is given by

$$I_1 + I_2 + I_3 = J_1 + J_2 + J_3. \quad (\text{D.9})$$

Now, notice that by virtue of the decay of $\phi_{z'}$ (and of $\partial_{\hat{n}} \phi_{z'}$) we have: $I_2 \xrightarrow{r_2 \rightarrow \infty} 0$, as well as $J_2 \xrightarrow{r_2 \rightarrow \infty} 0$. Also, notice that on D_1

$$\partial_{\hat{n}} \frac{1}{|\vec{r} - \vec{q}|} = \sum_{i=1}^3 \frac{\vec{r}_i - \vec{q}_i}{|\vec{r} - \vec{q}|} \cdot (-1) |\vec{r} - \vec{q}|^{-2} \cdot \frac{\vec{q}_i - \vec{r}_i}{|\vec{r} - \vec{q}|} = |\vec{r} - \vec{q}|^{-2} = \frac{1}{r_1^2}, \quad (\text{D.10})$$

hence:

$$I_1 = \int_{D_1} \frac{1}{r_1^2} \phi_{z'}(\vec{q}) \gamma_1^2 dS_2(\vec{q}) \xrightarrow{r_1 \rightarrow 0} 2\pi \phi_{z'}(\vec{r}), \quad (\text{D.11})$$

which follows from the same arguments used for equation (D.4). Simultaneously,

$$J_1 = \int_{D_1} \frac{1}{\gamma'} \partial_{\hat{n}} \phi_{z'}(\vec{q}) r_1^2 dS_2(\vec{q}) = r_1 \int_{D_1} \partial_{\hat{n}} \phi_{z'}(\vec{q}) dS_2(\vec{q}) \xrightarrow{r_1 \rightarrow 0} 0,$$

since r_1 is converges to zero and the integral is bounded.

We are left to investigate I_3 and J_3 . I_3 is identically zero, since

$$\partial_{\hat{n}} = \partial_{z'} \quad \text{in } D_1, \quad (\text{D.12})$$

and since the gradient of $\frac{1}{|\vec{r} - \vec{q}|}$ points radially, whenever this gradient is restricted to D_3 it is contained in D_3 (since D_3 is part of a plain that contains the origin); and thus it is orthogonal to its normal vector. Alternatively one can notice that the normal vector on D_3 is tangent to the level sets of $\frac{1}{|\vec{r} - \vec{q}|}$ and hence perpendicular to the gradient, thus its normal derivative on D_3 is zero, which implies that D_3 is identically zero.

To manipulate J_3 recall D.12 which yields

$$J_3 = \int_{D_3} \frac{1}{|\vec{r} - \vec{q}|} \partial_{z'z'} \phi(\vec{q}) dA(\vec{q}) = - \int_{D_3} \frac{1}{|\vec{r} - \vec{q}|} \Delta' \phi(\vec{q}) dA(\vec{q}), \quad (\text{D.13})$$

where $\Delta' = \partial_{x'x'} + \partial_{y'y'}$. We can now apply Green's identity once again, but now on D_1 . This yields

$$J_3 = - \int_{D_3} \phi(\vec{q}) \Delta' \frac{1}{|\vec{r} - \vec{q}|} dA(\vec{q}) - \int_{C_1 \cup C_2} \frac{1}{|\vec{r} - \vec{q}|} \partial_{\hat{n}} \phi(\vec{q}) dl(\vec{q}) + \int_{C_1 \cup C_2} \phi(\vec{q}) \partial_{\hat{n}} \frac{1}{|\vec{r} - \vec{q}|} d\vec{q}. \quad (\text{D.14})$$

Notice that

$$\Delta' \frac{1}{|\vec{r} - \vec{q}|} = \sum_{i=1}^2 \partial_i ((\vec{r}_i - \vec{q}_i) |\vec{r} - \vec{q}|^{-3}), \quad (\text{D.15})$$

as follows from equation (D.10), hence

$$\Delta' \frac{1}{|\vec{r} - \vec{q}|} = \sum_{i=1}^2 \left(-|\vec{r} - \vec{q}|^{-3} + (\vec{r}_i - \vec{q}_i)(-3)|\vec{r} - \vec{q}|^{-4} \frac{\vec{q}_i - \vec{r}_i}{|\vec{r} - \vec{q}|} \right), \quad (\text{D.16})$$

i.e.

$$\Delta' \frac{1}{|\vec{r} - \vec{q}|} = -2|\vec{r} - \vec{q}|^{-3} + 3|\vec{r} - \vec{q}|^{-3} = \frac{1}{|\vec{r} - \vec{q}|^3}. \quad (\text{D.17})$$

Therefore

$$J_4 := - \int_{D_3} \phi(\vec{q}) \Delta' \frac{1}{|\vec{r} - \vec{q}|} dA(\vec{q}) = - \int_{D_3} \frac{\phi(\vec{q})}{|\vec{r} - \vec{q}|^3} dA(\vec{q}). \quad (\text{D.18})$$

Define also

$$J5 := - \int_{C_1} \frac{1}{|\vec{r} - \vec{q}|} \partial_{\hat{n}} \phi(\vec{q}) dl(\vec{q}),$$

$$J6 := - \int_{C_2} \frac{1}{|\vec{r} - \vec{q}|} \partial_{\hat{n}} \phi(\vec{q}) dl(\vec{q}),$$

$$J7 := \int_{C_1} \phi(\vec{q}) \partial_{\hat{n}} \frac{1}{|\vec{r} - \vec{q}|} dl(\vec{q}),$$

$$J8 := \int_{C_8} \phi(\vec{q}) \partial_{\hat{n}} \frac{1}{|\vec{r} - \vec{q}|} dl(\vec{q});$$

which yields

$$J_3 = J_4 + J_5 + J_6 + J_7 + J_8.$$

Notice now that J_6 and J_8 will converge to zero as $r_2 \rightarrow \infty$ on virtue of the decay of ϕ and its derivatives. Also we can easily see that:

$$J_5 = - \int_0^{2\pi} \frac{\partial_{\hat{n}} \phi(\vec{q})}{\gamma_1} \gamma_1 d\theta \xrightarrow{r_1 \rightarrow 0} 0;$$

since the integrand becomes symmetric as r_1 approaches zero. To analyze J_7 we need to consider

$$\partial_{\hat{n}} \frac{1}{|\vec{r} - \vec{q}|} = \left| \nabla \left(\frac{1}{|\vec{r} - \vec{q}|} \right) \right| = \frac{1}{|\vec{r} - \vec{q}|^2}.$$

Hence we have

$$J7 = \underbrace{\int_{C_1} \frac{\phi(\vec{q}) - \phi(\vec{r})}{|\vec{r} - \vec{q}|^2} dl(\vec{q})}_{J_9} + \underbrace{\phi(\vec{r}) \int_{C_1} \frac{1}{|\vec{r} - \vec{q}|^2} dl(\vec{q})}_{J_{10}}.$$

Notice now

$$J_9 = - \int_{C_1} \frac{\nabla \phi(\vec{r})(\vec{q} - \vec{r})}{|\vec{r} - \vec{q}|^2} dl(\vec{q}) - \int_{C_1} \frac{\zeta(\vec{q} - \vec{r}) |\vec{q} - \vec{r}|}{|\vec{r} - \vec{q}|^2} dl(\vec{q});$$

where $\zeta(\vec{q} - \vec{r}) \rightarrow 0$ as $r_1 \rightarrow 0$ and thus

$$- \int_{C_1} \frac{\zeta(\vec{q} - \vec{r}) |\vec{q} - \vec{r}|}{|\vec{r} - \vec{q}|^2} dl(\vec{q}) = - \int_0^{2\pi} \frac{\zeta(\vec{q} - \vec{r}) \gamma_1^2}{\gamma_1^2} d\theta \xrightarrow{r_1 \rightarrow 0} 0,$$

while

$$- \int_{C_1} \frac{\nabla \phi(\vec{r})(\vec{q} - \vec{r})}{|\vec{r} - \vec{q}|^2} dl(\vec{q}) = - \int_0^{2\pi} \frac{\nabla \phi(\vec{r})(\vec{q} - \vec{r})}{r_1^2} \gamma_1 d\theta \xrightarrow{r_1 \rightarrow 0} 0;$$

due to the symmetry of the linear transformation given by $\nabla\phi(\vec{r})$.

Now notice that

$$J_{10} = \phi(\vec{r}) \int_0^{2\pi} \frac{1}{r_1^2} r_1 d\theta = \phi(\vec{r}) \frac{2\pi}{r_1} = \phi(\vec{r}) \int_0^{2\pi} \int_{r_1}^{\infty} \frac{1}{r^3} r dr d\theta,$$

therefore

$$J_{10} = \int_{r>r_1} \frac{\phi(\vec{r})}{|\vec{r} - \vec{q}|^3} dA(\vec{q}).$$

Sumarizing we have:

$$I_1 + (I_2) + J_3 = J_1 + (J_2) + \underbrace{J_3}_{J_4+\dots+J_8} = J_1 + (J_2 + J_6 + J_8) + J_4 + J_5 + J_7,$$

where we have canceled identically null terms and grouped in parenthesis the quantities that got to zero as $r_2 \rightarrow \infty$. Notice that all the other terms remain finite when we take the limit of $r_2 \rightarrow \infty$. We now take the limit and obtain

$$I_1 = J_1 - \int_{r>r_1} \frac{\phi(\vec{q})}{|\vec{r} - \vec{q}|^3} dA(\vec{q}) + J_5 + \underbrace{J_7}_{J_9+J_{10}}.$$

Notice that J_4 was the only term whose expression changed (among the integral that were not grouped in parenthesis) when taking the limit of $r_2 \rightarrow \infty$, this is because it was the only one that depended on r_2 . We now proceed to substitute J_7 by its equal and group in brackets those quantities that converge to zero as $r_1 \rightarrow 0$

$$I_1 = - \int_{r>r_1} \frac{\phi(\vec{q})}{|\vec{r} - \vec{q}|^3} dA(\vec{q}) + J_{10} + [J_1 + J_5 + J_9],$$

We also substitute J_{10} by its expression since it can be naturally combined with the other integral in the equation above. We thus obtain

$$I_2 = - \int_{r>r_1} \frac{\phi(\vec{q})}{|\vec{r} - \vec{q}|^3} dA(\vec{q}) + \int_{r>r_1} \frac{\phi(\vec{r})}{|\vec{r} - \vec{q}|^3} dA(\vec{q}) + [J_5 + J_2 + J_9],$$

i.e.

$$I_2 = \int_{r>r_1} \frac{\phi(\vec{r}) - \phi(\vec{q})}{|\vec{r} - \vec{q}|^3} dA(\vec{q}) + [J_5 + J_2 + J_9],$$

we now take the limit of $r_1 \rightarrow 0$, and finally obtain (by virtue of equation (D.11))

$$\phi_z(\vec{r}) = \frac{1}{2\pi} P.V. \int \frac{\phi(\vec{r}) - \phi(\vec{q})}{|\vec{r} - \vec{q}|^3} dA(\vec{q}). \quad (\text{D.19})$$

Notice that, in order for this inversion to work, we needed to add the hypothesis is that $\phi(z' = 0) \in C^2(\mathbb{R}^2)$. This was necessary for us to take the Laplacian on the plane. We also assumed that the boundary satisfies the Laplace equation when the normal derivative is taken for the $\partial_{z'z'}$.

D.1.3 Convergence of the singular integral of the N map in the principal value sense

Consider

$$P.V. \int \frac{\phi(\vec{r}) - \phi(\vec{q})}{|\vec{r} - \vec{q}|^3} dA(\vec{q}) = \lim_{\epsilon \rightarrow 0} \int_{|\vec{r} - \vec{q}| > \epsilon} \frac{\phi(\vec{r}) - \phi(\vec{q})}{|\vec{r} - \vec{q}|^3} dA(\vec{q})$$

Notice that given any radius $r_0 > 0$ arbitrarily small, for any bounded ϕ of class C^2 we have:

$$P.V. \int \frac{\phi(\vec{r}) - \phi(\vec{q})}{|\vec{r} - \vec{q}|^3} dA(\vec{q}) = \underbrace{\lim_{\epsilon \rightarrow 0} \int_{r_0 > |\vec{r} - \vec{q}| > \epsilon} \frac{\phi(\vec{r}) - \phi(\vec{q})}{|\vec{r} - \vec{q}|^3} dA(\vec{q})}_{K_1} + \underbrace{\int_{|\vec{r} - \vec{q}| > r_0} \frac{\phi(\vec{r}) - \phi(\vec{q})}{|\vec{r} - \vec{q}|^3} dA(\vec{q})}_{K_2}$$

Notice that K_2 is bounded, and that $K_1 = K_3 + K_4 + K_5$, where

$$K_3 = - \lim_{\epsilon \rightarrow 0} \int_0^{2\pi} \int_{|\vec{r} - \vec{q}| = \epsilon}^{r_0} \frac{\nabla \phi(\vec{r})(\vec{q} - \vec{r})}{|\vec{r} - \vec{q}|^3} |\vec{q} - \vec{r}| d|\vec{q} - \vec{r}| d\theta,$$

$$K_4 = - \frac{1}{2} \lim_{\epsilon \rightarrow 0} \int_0^{2\pi} \int_{|\vec{r} - \vec{q}| = \epsilon}^{r_0} \frac{(\vec{q} - \vec{r})^T}{|\vec{q} - \vec{r}|} H(\vec{r}) \frac{(\vec{q} - \vec{r})^T}{|\vec{q} - \vec{r}|} d|\vec{q} - \vec{r}| d\theta,$$

and

$$K_5 = - \lim_{\epsilon \rightarrow 0} \int_0^{2\pi} \int_{|\vec{r} - \vec{q}| = \epsilon}^{r_0} \frac{\xi(\vec{q}) |\vec{q} - \vec{r}|^2}{|\vec{q} - \vec{r}|^3} |\vec{q} - \vec{r}| d|\vec{q} - \vec{r}| d\theta$$

where $\xi(\vec{q}) \rightarrow 0$ as $\vec{q} \rightarrow \vec{r}$. Notice that K_3 is identically zero due to symmetries, and K_4 and K_5 are bounded. We thus have

$$P.V. \int \frac{\phi(\vec{r}) - \phi(\vec{q})}{|\vec{r} - \vec{q}|^3} dA(\vec{q}) = K_4 + K_5 + K_2$$

where the bounds for the right hand side show that the singular integral converges.

It is clear now that all the separation of limits above made are legitimate, since all the limits exist once separated, as was shown.

This page was intentionally left blank.

Bibliography

- [1] T. B. Benjamin and F. Ursell. The stability of the plane free surface of a liquid in vertical periodic motion. *Proc. R. Soc. Lond. A*, 225:505–515, 1954.
- [2] H. Bhatia, G. Norgard, V. Pascucci, and P.-T. Bremer. The helmholtz-hodge decomposition—a survey. *IEEE Transactions on Visualization and Computer Graphics*, 19(X), 2013.
- [3] O. Blumenthal. über die zerlegung unendlicher vektorfelder. *Mathematische Annalen*, 61(2):235–250, 1905.
- [4] C. Borghesi, J. Moukhtar, M. Labousee, A. Eddi, E. Fort, and Y. Couder. The interaction of two walkers: wave-mediated energy and force. *Phys. Rev. E*, 90(063017), 2014.
- [5] J. W. M. Bush. personal communication.
- [6] J. W. M. Bush. Quantum mechanics writ large. *Proc. Natl. Acad. Sci. U.S.A.*, 107(41):17455–17456, 2010.
- [7] J. W. M. Bush. The new wave of pilot-wave theory. *Physics Today*, 68(8):47–53, 2015.
- [8] J. W. M. Bush, A. U. Oza, and J. Moláćek. The wave-induced added mass of walking droplets. *J. Fluid Mech.*, 755(R7), 2014.
- [9] John W. M. Bush. Pilot-wave hydrodynamics. *Annu. Rev. Fluid Mech.*, 47:269–292, 2015.
- [10] Y. Couder and E. Fort. Single-particle diffraction and interference at a macroscopic scale. *Phys. Rev. Lett.*, 97(154101), 2006.
- [11] Y. Couder, E. Fort, C.H. Gautier, and A. Boudaoud. From bouncing to floating: Noncoalescence of drops on a fluid bath. *Phys. Rev. Lett.*, 94(177801), 2005.
- [12] Y. Couder, S. Protière, E. Fort, and A. Boudaoud. Walking and orbiting droplets. *Nature*, 437(208), 2005.

- [13] A. Damiano, P.T. Brun, and J. W. M. Bush. personal communication.
- [14] A. P. Damiano. Surface topography measurements of the bouncing droplet experiment. Master's thesis, École Polytechnique Fédérale de Lausanne, 2015.
- [15] L. De Broglie. *Ondes et mouvements*. Gauthier-Villars, 1926.
- [16] L. De Broglie. *An Introduction to the Study of Wave Mechanics*. Methuen, 1930.
- [17] L. De Broglie. *Une interprétation causale et non linéaire de la Mécanique ondulatoire: la théorie de la double solutions*. Gauthier-Villars, 1956.
- [18] L. De Broglie. Interpretation of quantum mechanics by the double solution theory. *Ann. Fond. Louis de Broglie*, 12:1–23, 1987.
- [19] F. Dias, A. I. Dyachenko, and V. E. Zakharov. Theory of weakly damped free-surface flows: A new formulation based on potential flow solutions. *Phys. Lett. A*, 372:1297–1302, 2008.
- [20] A. Eddi, A. Decelle, E. Fort, and Y. Couder. Archimedean lattices in the bound states of wave interacting particles. *Europhys. Lett.*, 87(56002), 2009.
- [21] A. Eddi, E. Fort, F. Moisy, and Y. Couder. Unpredictable tunneling of a classical wave-particle association. *Phys. Rev. Lett.*, 102(240401), 2009.
- [22] A. Eddi, J. Moukhtar, S. Perrard, E. Fort, and Y. Couder. Level splitting at macroscopic scale. *Phys. Rev. Lett.*, 108(264503), 2012.
- [23] A. Eddi, R. Sultan, J. Moukhtar, E. Fort, M. Rossi, and Y. Couder. Information stored in faraday waves: the origin of a path memory. *J. Fluid Mech.*, 674:433–463, 2011.
- [24] A. Eddi, D. Terwagne, E. Fort, and Y. Couder. Wave propelled ratchets and drifting rafts. *Europhys. Lett.*, 82(44001), 2008.
- [25] R. Farwig, H. Kozono, and H. Sohr. An l^q -approach to stokes and navier-stokes equations in general domains. *Acta Math.*, 195:21–53, 2005.
- [26] L. K. Forbes. An algorithm for 3-dimensional free-surface problems in hydrodynamics. *J. Comput. Phys.*, 82:330–347, 1989.
- [27] E. Fort, A. Eddi, A. Boudaoud, J. Moukhtar, and Y. Couder. Path-memmory induced quantization of classical orbits. *Proc. Natl. Acad. Sci. U.S.A.*, 107(41):17515–17520, 2010.
- [28] T. Gilet. Dynamics and statistics of wave-particle interactions in a confined geometry. *Phys. Rev. E*, 90(052917), 2014.
- [29] D. Harris. *The Pilot-Wave Dynamics of Walking Droplets in Confinement*. PhD thesis, Massachusetts Institute of Technology, 2015.

- [30] D. M. Harris and J. W. M. Bush. The pilot-wave dynamics of walking droplets. *Physics of Fluids*, 25(091112), 2013.
- [31] D. M. Harris and J. W. M. Bush. Droplets walking in a rotating frame: from quantized orbits to multimodal statistics. *J. Fluid Mech.*, 739:444–464, 2014.
- [32] D. M. Harris and J. W. M. Bush. Generating uniaxial vibration with an electrodynamic shaker and external air bearing. *Journal of Sound and Vibration*, 334:255–269, 2015.
- [33] D. M. Harris, T. Liu, and J. W. M. Bush. A low-cost, precise piezoelectric droplet-on-demand generator. *Exp. Fluids*, 56(83), 2015.
- [34] D. M. Harris, J. Moukhtar, E. Fort, Y. Couder, and J. W. M. Bush. Wavelike statistics from pilot-wave dynamics in a circular corral. *Phys. Rev. E*, 88(011001), 2013.
- [35] H. P. Kavehpour. Coalescence of drops. *Annu. Rev. Fluid Mech.*, 47:245–268, 2015.
- [36] K. Kumar. Linear theory of faraday instability in viscous liquids. *Proc. R. Soc. A*, 452(1948):1113–1126, 1996.
- [37] H. Lamb. *Hydrodynamics*. Cambridge Univ. Press, 1895.
- [38] P. Milewski, C. A. Galeano-Rios, A. Nachbin, and J. W. M. Bush. Faraday pilot-wave dynamics: modeling and computation. *J. Fluid Mech.*, 778:361–388, 2015.
- [39] F. Moisy, M. Rabaud, and K. Salsac. A synthetic schlieren method for the measurement of the topography of a liquid interface. *Exp. Fluids*, 46(1021), 2009.
- [40] J. Moláček and J. W. M. Bush. Drops bouncing on a vibrating bath. *J. Fluid Mech.*, 727:582–611, 2013.
- [41] J. Moláček and J. W. M. Bush. Drops walking on a vibrating bath: towards a hydrodynamic pilot-wave theory. *J. Fluid Mech.*, 727:612–647, 2013.
- [42] A. U. Oza, D. M. Harris, R. R. Rosales, and J. W. M. Bush. Pilot-wave hydrodynamics in a rotating frame: on the emergence of orbital quantization. *J. Fluid Mech.*, 744:404–429, 2014.
- [43] A. U. Oza, R. R. Rosale, and J. W. M. Bush. A trajectory equation for walking droplets: hydrodynamic pilot-wave theory. *J. Fluid Mech.*, 737:552–570, 2013.
- [44] A. U. Oza, O. Wind-Willassen, D. M. Harris, R. R. Rosales, and J. W. M. Bush. Pilot-wave hydrodynamics in a rotating frame: Exotic orbits. *Physics of Fluids*, 26(082101), 2014.
- [45] S. Perrard, M. Labousse, E. Fort, and Y. Couder. Chaos driven by interfering memory. *Phys. Rev. Lett.*, 113(104101), 2014.

- [46] S. Perrard, M. Labousse, M. Miskin, E. Fort, and Y. Couder. Self-organization into quantized eigenstates of a classical wave-driven particle. *Nat. Commun.*, 5(3219), 2014.
- [47] S. Protière, S. Bohn, and Y. Couder. Exotic orbits of two interacting wave sources. *Phys. Rev. E*, 78(036204), 2008.
- [48] S. Protière, A. Boudaoud, and Y. Couder. Particle-wave association on a fluid interface. *J. Fluid Mech.*, 554:85–108, 2006.
- [49] D. Terwagne, T. Gilet, N. Vandewalle, and S. Dombolo. From bouncing to boxing. *Chaos*, 18(041104), 2008.
- [50] D. Terwagne, F. Ludewig, N. Vandewalle, and S. Dombolo. The role of droplet deformations in the bouncing droplet dynamics. *Physics of Fluids*, 25(122101), 2013.
- [51] D. Terwagne, N. Vandewalle, and S. Dombolo. Lifetime of a bouncing droplet. *Phys. Rev. E*, 76(056311), 2007.
- [52] N. Vandewalle, D. Terwagne, K. Mulleners, T. Gilet, and S. Dombolo. Dancing droplets onto liquid surfaces. *Physics of Fluids*, 18(091106), 2006.
- [53] O. Wind-Willansen, J. Moláček, D. Harris, and J. W. M. Bush. Exotic states of bouncing and walking droplets. *Phys. Fluids*, 25(0820023), 2013.